THE UNIVERSITY *of* EDINBURGH

Underground Study of the ^{17}O(p,γ)^{18}F Reaction at Gamow Energies for Classical Novae

D. A. Scott

A thesis submitted in fulfilment of the requirements
for the degree of Doctor of Philosophy
to the
University of Edinburgh
July 2014

Abstract

Classical novae are explained as thermonuclear explosions on the surface of white dwarf stars accreting hydrogen-rich material from less evolved companions in binary star systems. These events occur frequently within our galaxy and have been proposed as significant contributors to the galactic abundance of ^{13}C, ^{15}N, $^{17/18}$O and $^{18/19}$F. The short-lived isotope ^{18}F ($t_{1/2}$ = 110 min) is of particular importance since it may provide a signature of novae events through the detection of 511 keV γ-ray emission following the β^+ decay of a ^{18}F nucleus. During classical novae the ^{17}O(p,γ)^{18}F reaction governs the production of ^{18}F and affects the synthesis of the rare isotopes mentioned above. Prior to the present study, the ^{17}O(p,γ)^{18}F reaction rate was poorly determined owing to a lack of low-energy experimental data. The present work reports on the first accurate measurements of the resonant and non-resonant contributions to the ^{17}O(p,γ)^{18}F reaction cross section in the energy region relevant for classical novae.

Measurements were performed at the Laboratory for Underground Nuclear Astrophysics (LUNA) accelerator facility of the Laboratori Nazionali del Gran Sasso (LNGS) in Italy. Here the γ-ray background is suppressed by up to 3 orders of magnitude, thus providing a unique environment for low-energy measurements of reaction cross sections.

Prompt γ rays associated with the formation and decay of states in ^{18}F were analysed to determine the resonant and non-resonant contributions to the reaction cross section. The total non-resonant S-factor was determined at energies between $E_{\rm cm} \approx$ 200 - 370 keV and the strength of a key resonance at $E_{\rm cm}$ = 183 keV was obtained with the best precision to date. The uncertainty in the reaction rate is now sufficiently low to place firmer constraints on nucleosynthesis predictions from accurate models of novae.

Lay Summary

The vast majority of elements heavier than hydrogen are produced as a result of nuclear fusion reactions inside the hot interiors of stars. The energy released by the successive fusion of progressively heavier elements counteracts the gravitational force, maintaining stability throughout much of a star's life. In contrast to this quiescent phase of stellar evolution, many astrophysical sites are associated with explosive nuclear processes which occur under extreme conditions of temperature and pressure, and involve a large number of different nuclear reactions. Classical novae, which take place on the surface of a dense, compact star referred to as a white dwarf, represent one such example. It is generally the case that many aspects of explosive stellar events are governed by the nuclear reactions which occur within them. The work presented in this thesis concerns the experimental investigation of a specific nuclear fusion reaction between hydrogen nuclei (protons) and an isotope of oxygen (^{17}O), which affects the abundances of several rare isotopes that are produced during classical novae events. This reaction is directly responsible for producing ^{18}F, a radioactive isotope associated with the emission of high energy electromagnetic radiation known as gamma rays. Detection of this radiation by satellite observatories could provide an unambiguous signature of a nova event having taken place. This is important as it may potentially allow for comparisons to be made between observational features of novae and theoretical models based on nuclear physics information.

The present work has involved studying the ^{17}O(p,γ)^{18}F reaction in a laboratory setting in order to measure the likelihood of its occurrence (reaction cross section) at energies typical of classical novae. The formation of ^{18}F via the ^{17}O(p,γ)^{18}F reaction is accompanied by the production of gamma radiation, which can be detected and analysed in order to determine the reaction cross section. However, due to the extremely low cross sections typical of nuclear reaction at

stellar energies experiments of this nature are often hampered by background radiation, mainly of a cosmic origin. For this reason the present investigation has been performed in a laboratory located deep underground, where the level of background radiation is greatly reduced.

Declaration

The experiment described in this thesis was performed by myself and fellow members of the LUNA collaboration. The data analysis and interpretation of results are entirely my own work, and this thesis has been written entirely by myself. No portion of the work referred to in this thesis has been submitted in support of an application for another degree qualification at this university or any other academic institution. Parts of this work have been published in references [1] and [2].

D. A. Scott
July 2014

Acknowledgements

First and foremost I thank my supervisor, Marialuisa Aliotta, whom I am greatly indebted to for all the support and guidance she has provided throughout my studies at Edinburgh.

I thank the members of the LUNA collaboration, many of whom I have worked with closely during the course of my PhD. In particular, I thank Alba Formicola (my second supervisor) and Matthias Junker for providing me with so many opportunities and making me feel extremely welcome in Italy. I would also like to thank Gianluca Imbriani, Antonino Di Leva and Frank Strieder for several invaluable discussions on many aspects of my data analysis. Thank you Carlo for many 'memorable' shifts working underground.

Thanks goes to the staff and students of the Edinburgh University Nuclear Physics Group for making my time spent here so enjoyable. You know who you all are and I am extremely grateful for your friendship and support.

Thank you Rachel for all the good times we have shared together over the last few years. I wish you every success in the future.

Finally, I thank my family, Andrew, Margaret and Alison, to whom I owe so much.

Contents

List of Figures

List of Tables

Introduction

Driven by the fervent curiosity that is characteristic of the human condition, cultures around the world have long sought to understand their place in the Cosmos. In its attempt to explain the complex array of astronomical phenomena visible in our universe as well as the processes that govern their evolution, the field of nuclear astrophysics is a continuation of this long-standing drive. Early applications of nuclear physics to the area of astronomy were aimed at identifying the processes responsible for generating the energy necessary to support our Sun. In 1938, Bethe and Critchfield [3] demonstrated that sufficient energy could be provided from the fusion of hydrogen into helium, inviting scientists to question what other nuclear reactions might take place inside the hot interiors of stars. At that time, the origin of the 90 or so naturally occurring chemical elements remained a mystery, although there existed widespread support for the theory that the majority were produced in the *Big Bang* [4]. However, by the late 1950s this view had been overthrown with the publication of the landmark paper of Burbidge, Burbidge, Fowler and Hoyle [5], which proposed stars as the true site for the synthesis of the elements. Burbidge *et al.* recognised that while elements up to the iron region could be produced by successive stages of quiescent burning, the formation of heavier species requires more extreme conditions of temperature and density such as those found in supernovae and other explosive events. The arguments presented in [5] are particularly convincing as they go a long way to explaining the large variation in the measured relative abundances of the different elements [6].

Despite the wealth of observational information that now exists for a diverse range of stellar systems, gaining a detailed understanding of the mechanisms underlying their properties and behaviour often requires nuclear physics input in the form of reaction rates. Ideally this information is acquired by directly studying

reactions in a laboratory setting; however, this is often extremely challenging due to the low probability for a given reaction to take place at the energies typical of stellar environments (Chapter 2).

This thesis is dedicated to the experimental investigation of a particular nuclear reaction, namely that of $^{17}O(p,\gamma)^{18}F$, which has important consequences for a class of explosive stellar events referred to as classical novae. The investigation presented in this thesis was performed at the Laboratory for Underground Nuclear Astrophysics (LUNA) accelerator facility of the Laboratori Nazionali del Gran Sasso (LNGS), Italy. The resonant and non-resonant contributions to the $^{17}O(p,\gamma)^{18}F$ reaction cross section were determined by measuring the prompt γ-ray yield associated with transitions to and from states in ^{18}F. This information has been used to calculate the total reaction rate.

Chapter 1 provides a brief introduction to stellar evolution, a description of classical novae events, and a discussion of the importance of the $^{17}O(p,\gamma)^{18}F$ reaction in this context. An overview of the theoretical formalism developed to model stellar reaction rates together with many of the concepts underpinning the present work is presented in Chapter 2. Chapter 3 contains a critical evaluation of the findings of all previous investigations of the $^{17}O(p,\gamma)^{18}F$ reaction while in Chapter 4 I describe the methodology employed in the present study. The underground LUNA accelerator facility where these measurements have been undertaken is described in Chapter 5, where I also present details of the experimental setup. In Chapter 6, I discuss the analysis and results of this investigation, the astrophysical implications of which are finally presented in Chapter 7.

Chapter 1

Stellar Evolution and Classical Novae

1.1 General aspects of stellar evolution

Stellar evolution is governed by nuclear fusion reactions, which generate the internal pressure necessary to support stars from gravitational collapse. The specific reactions that occur are determined by the temperature and composition of the stellar interior. As the lightest element, hydrogen nuclei have the lowest Coulomb barrier (Chapter 2) and are therefore the first to undergo nuclear fusion (referred to as *hydrogen burning*) in the core of a star. Once hydrogen fusion reactions cease, the star will contract under gravity. This raises the temperature, eventually resulting in the initiation of fusion reactions between the next heaviest nuclear species (in this case helium). Figure 1.1 shows the total energy emitted by a one-solar-mass star as a function of core temperature during the hydrogen and helium burning stages of stellar evolution.

The scenario described above illustrates the general principle governing the evolution of stars, *i.e.* alternating periods of gravitational contraction and nuclear burning leading to the synthesis of progressively heavier elements in order to maintain hydrostatic equilibrium. Carbon burning, followed by oxygen, neon and finally silicon burning processes may produce elements up to the iron mass region. Since elements heavier than iron have a relatively lower binding energy, further fusion reactions do not liberate energy. This ultimately leads to the catastrophic collapse of the star resulting in a *type II supernova*. These explosive events are

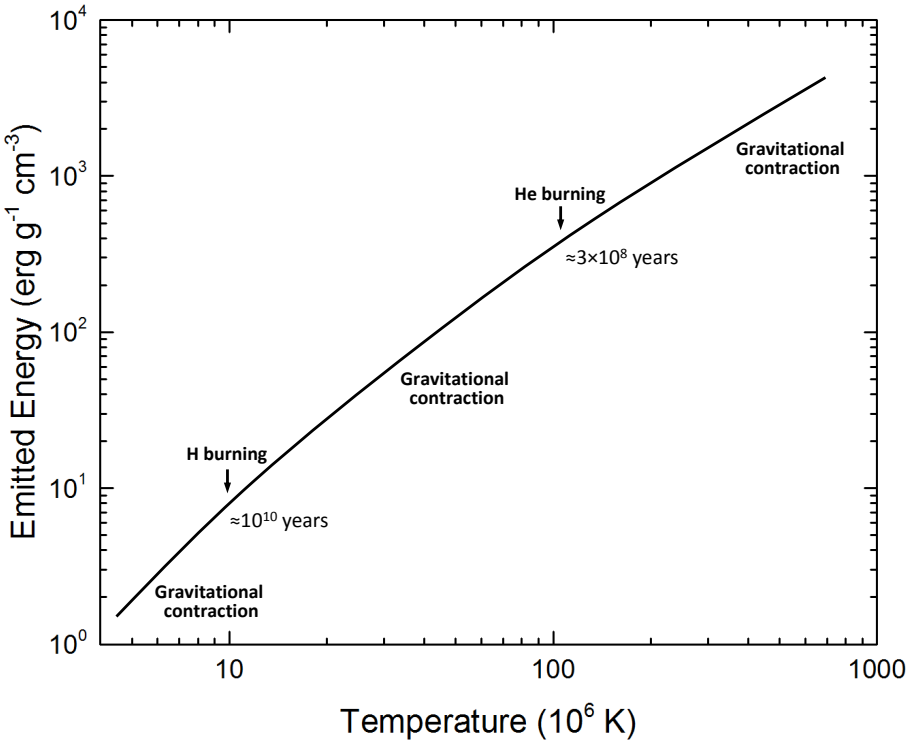

Figure 1.1: The (approximate) total energy emitted by a one-solar-mass star as a function of core temperature during the hydrogen and helium burning stages of stellar evolution [7]. (1 erg = 624.15 GeV). The approximate duration of each nuclear burning episode is also shown.

responsible for enriching the interstellar medium with heavy elements.

Whether or not all of the nuclear burning stages leading up to a type II supernova are completed depends on the mass of the star, since this largely determines the internal temperature. Stars of mass[1] lower than approximately $M = 11M_{\odot}$ generally do not attain core temperatures sufficiently high to synthesise elements heavier than neon and ultimately become *white dwarfs* (Section 1.4).

1.2 Stellar formation and the main sequence

Stars originate from the gravitational collapse of cold (10-50 K [8]) interstellar clouds of gas, predominantly consisting of molecular hydrogen (approximately 70% by mass) and helium (constituting most of the remaining 30%) and possibly

[1]The mass and luminosity of a given stellar system are commonly defined in terms of the solar values, mass $M_{\odot} = 1.99\times10^{30}$ kg and luminosity $L_{\odot} = 3.85\times10^{33}$ erg/s respectively.

trace amounts of heavier elements. The initial collapse of an interstellar cloud of gas takes place in isothermal equilibrium since heat is efficiently lost from the system through the emission of electromagnetic radiation. As density increases, the collapsing gas becomes opaque to radiation and thus the temperature rises. This leads to the dissociation of hydrogen molecules followed by the ionisation of hydrogen atoms. Eventually, the internal pressure become sufficiently large to oppose further gravitational contraction and a state of hydrostatic equilibrium is established in the core of the collapsing cloud. The energy transport processes supporting the system (referred to as a *protostar*) are highly convective. However, once most hydrogen has become fully ionised, the opacity[2] of the core falls and heat is efficiently radiated into the surrounding stellar envelope. As a consequence, the core gradually shrinks in size and the temperature rises steadily. Once core temperatures reach $T \approx (1\text{-}2)\times10^7$ K [9] hydrogen ions possess sufficient energy to undergo nuclear fusion through a series of reactions referred to as the proton-proton (P-P) chain (Figure 1.2), the net result of which is the conversion of four hydrogen nuclei into an alpha particle (^{4}He nucleus). Since the mass of a ^{4}He nucleus is lower than that of four hydrogen nuclei, these processes are accompanied by a release of energy (approximately 27 MeV for a full sequence).

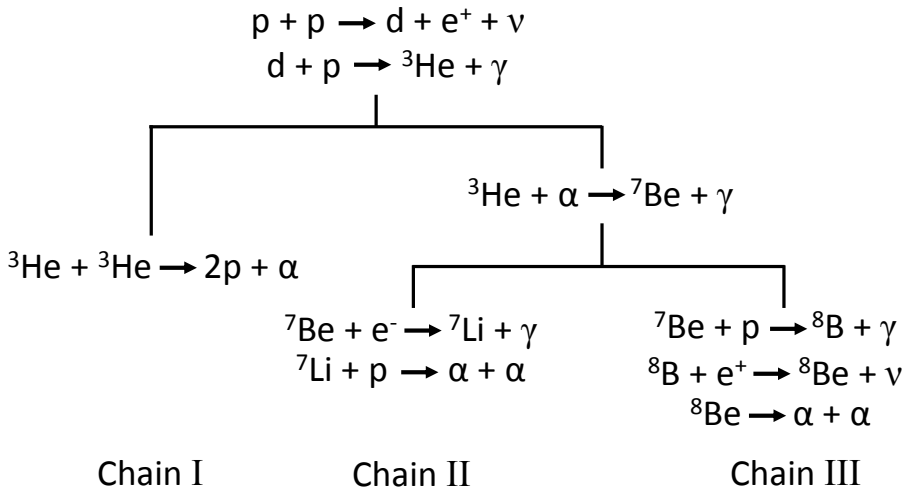

Figure 1.2: The proton-proton (P-P) chain reactions.

[2]At low temperature the opacity of a gas is mainly due to photo-absorption processes while free electron scattering dominates once a significant fraction of atoms have become ionised.

For stars with masses above $M \approx 1.5 M_{\odot}$ that contain trace amounts of carbon, nitrogen and oxygen, hydrogen burning can take place via a series of reactions (shown in Figure 1.3) known as the CNO cycles. The net result of the CNO cycles is identical to that of the P-P chains, *i.e.* the conversion of four protons into a ^{4}He nucleus. The heavier elements involved in the various stages of the CNO cycles (carbon, nitrogen and oxygen) act as catalysts leaving their abundances almost unchanged. The temperature dependencies of the reaction rates involved in the P-P chains and CNO cycles (illustrated in Figure 1.4) means that the former process dominates the energy production at temperatures below approximately 0.02 GK.

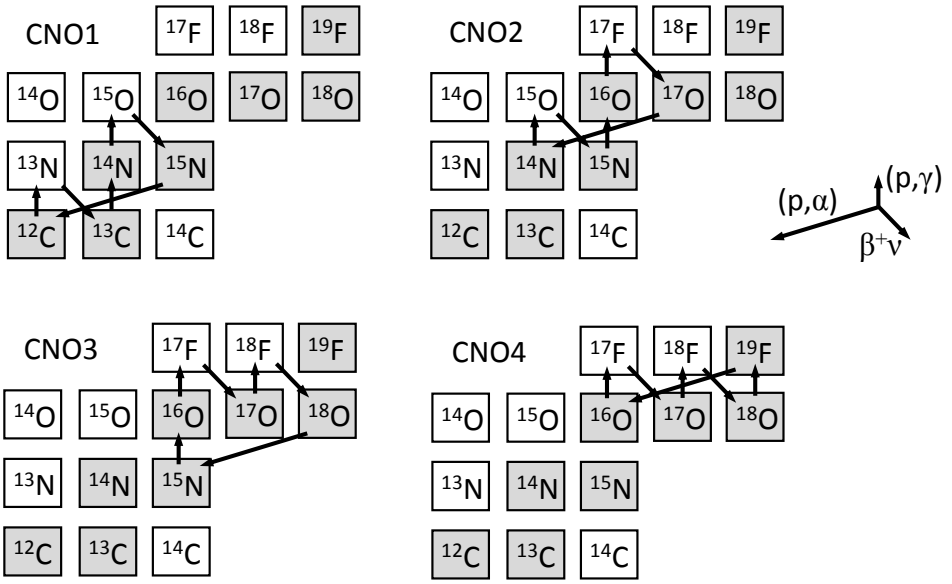

Figure 1.3: The CNO cycles. The net effect of this series of reactions is the fusion of hydrogen into helium. Stable isotopes are shown in grey.

The energy provided by the fusion of hydrogen to helium (via the proton-proton chains and CNO cycles) prevents the core of a protostar from further contraction. The phase of stellar evolution characterised by hydrostatic core hydrogen burning (so-called quiescent burning) is referred to as the *main sequence* and persists for approximately 10^{10} years for solar mass stars [7]. Stars remain part of the main sequence until hydrogen is depleted in their cores (which are then composed almost entirely of helium).

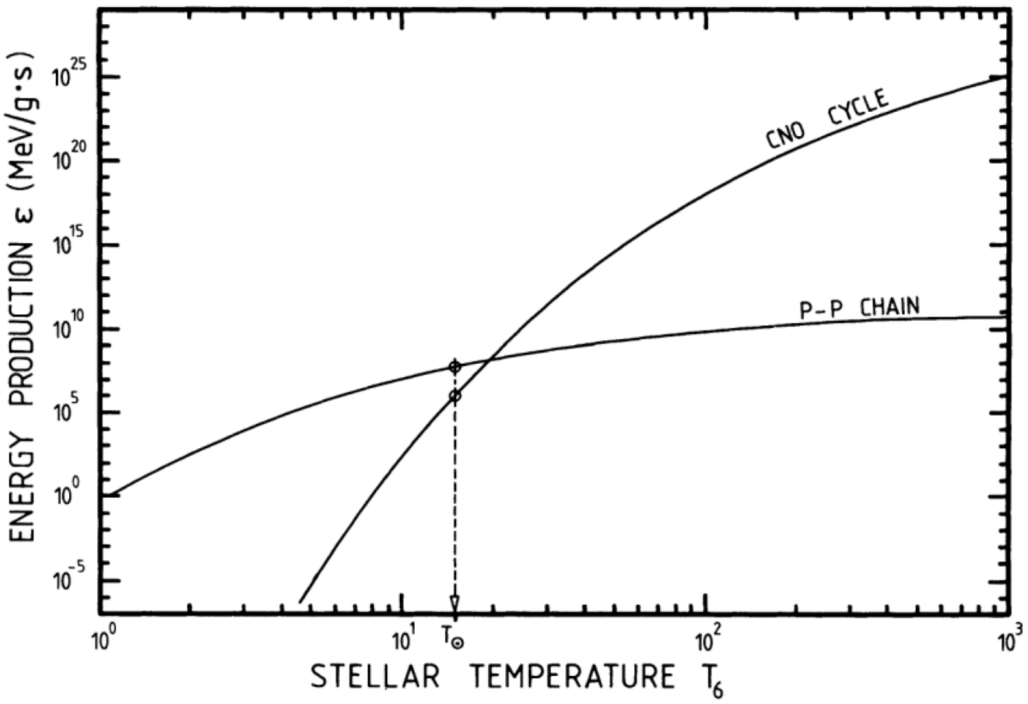

Figure 1.4: The energy production rate of the P-P chains and CNO cycles as a function of temperature [9].

In the following section I will describe the *red giant* phase of stellar evolution which is common to main sequence stars of all masses and of particular importance in the context of classical novae events.

1.3 Red giant stars

As hydrogen is depleted in the central region of a main sequence star the burning zone evolves into a shell surrounding an inner helium core. With no energy source supporting the core it slowly shrinks in volume, increasing the temperature at the base of the hydrogen burning region. This increases the rate of CNO cycle reactions, causing the outer regions of the star to expand and cool. This reduction in surface temperature is accompanied by a reddening of the emitted electromagnetic spectrum and the star is therefore referred to as a *red giant*. The gradual accumulation of helium from the hydrogen burning shell leads to the slow contraction (and heating) of the core of a red giant star. Eventually, helium

burning is ignited (at approximately $T = 0.1$ GK) via the *triple-alpha process* [10] which synthesises ^{12}C. Further alpha-capture reactions may lead to the production of ^{16}O, ^{20}Ne, ^{24}Mg and ^{28}Si. The star is now referred to as an *asymptotic giant branch* (AGB) star, in reference to its position on the *Hertzsprung-Russell* (H-R) *diagram*[3].

1.4 White dwarf stars

White dwarfs are the remnants of stars in the mass range $2M_\odot \leq M \leq 11M_\odot$ and are mainly composed of electron-degenerate matter. Here I summarise the origin of white dwarf stars and describe their key properties.

Helium burning asymptotic giant branch stars in the mass range $2M_\odot \leq M \leq 9M_\odot$ lead to the formation of stellar cores composed predominantly of carbon and oxygen, while slightly higher mass stars ($9M_\odot \leq M \leq 11M_\odot$) produce oxygen and neon cores as a result of alpha-capture reactions occurring with carbon and oxygen nuclei. As the mass of the C-O or O-Ne core increases due to the accretion of processed material from the helium burning shell, the density becomes so large that quantum effects due to the Pauli exclusion principle must be taken into account. Under such conditions matter is supported by electron degeneracy pressure, which inhibits further compression and maintains hydrostatic equilibrium. The equation of state for non-relativistic electron degenerate matter is of the form [7]:

$$P_{\text{deg}} \propto \rho^{\frac{5}{3}} \tag{1.1}$$

where ρ is density. Since the pressure, P_{deg}, is independent of temperature, any rise in temperature cannot be counteracted by an expansion in volume. Only once the temperature reaches approximately $T = 1$ GK does it become possible to populate electronic states above the *Fermi energy*[4] and the system reverts to an ideal gas (this is often described as the 'lifting' of electron degeneracy). These

[3]The Hertzsprung-Russell (H-R) diagram plots the distribution of stars on the luminosity versus effective temperature plane for a given stellar population [8]. Stars undergoing similar phases of stellar evolution are found to occupy only certain regions on this diagram.

[4]In a fully degenerate system, electrons occupy all quantum states up to a certain energy level. The difference in energy between the highest and lowest occupied state is referred to as the Fermi energy.

properties of electron-degenerate matter have direct implications for classical novae, as explained in Section 1.6.

The regions of an asymptotic giant branch star surrounding the degenerate core exist in an unstable configuration involving the periodic extinction and re-ignition of both helium and hydrogen burning shells (Figure 1.5). This ultimately leads to a series of thermal pulsations that eject almost the entire hydrogen-helium envelope from the surface of the star forming a *planetary nebula*. The degenerate C-O or O-Ne core (white dwarf) which is the remnant of this process undergoes no further nucleosynthesis. The maximum possible mass for a white dwarf is known as the *Chandrasekhar limit* and equals approximately $M = 1.4\,\mathrm{M}_{\odot}$, beyond which matter cannot be supported by electron degeneracy pressure.

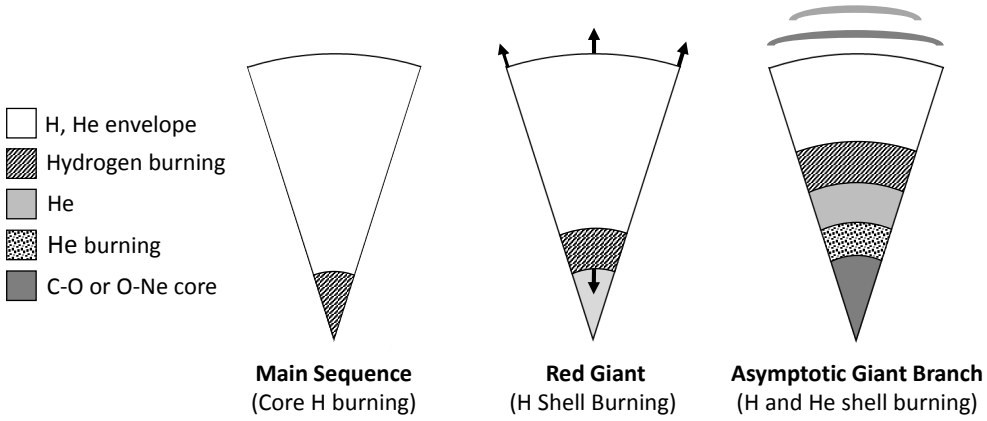

Figure 1.5: Interior composition of a main sequence, red giant and asymptotic giant branch (AGB) star. During the red giant phase the hydrogen-rich envelope expands as the core contracts (indicated by arrows).

1.5 Binary systems

Most stars are thought to exist in gravitationally bound systems consisting of two or more members in orbit around their common centre-of-mass [8]. Binary systems represent the most likely of such configurations. The region of space gravitationally bound to each of the two orbiting stars can be visualised by plotting equipotential surfaces enclosing volumes of space referred to as *Roche lobes* [11]. If one of the stars expands to such an extent that its Roche lobe is

completely filled, as for instance may happen during the red giant phase of stellar evolution, then material is free to flow onto the companion through the so-called *Inner Lagrangian Point* (Figure 1.6) and an accretion disk is formed (due to the conservation of angular momentum). This scenario can only arise if the two stars orbit in relatively close proximity, *i.e.* they exist in a *semi-detached* (as opposed to a *detached*) binary system.

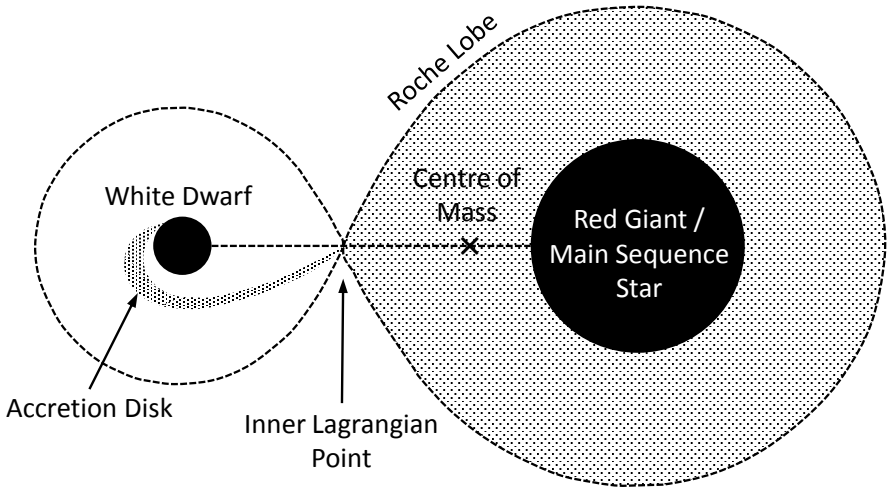

Figure 1.6: Illustration of a semi-detached binary system consisting of a white dwarf star and a red giant or main sequence companion, which has filled its Roche lobe. If the companion is expanding, matter can flow through the inner Lagrangian point leading to the formation of an accretion disk around the white dwarf.

1.6 Classical nova model

The precursor to a classical nova is a semi-detached binary system consisting of a white dwarf star and a less evolved main sequence or red giant companion. In this scenario (depicted in Figure 1.6), matter is accreted onto the surface of the white dwarf at a rate of approximately 10^{-8}-10^{-9} $M_{\odot}$ yr^{-1} [8]. As this hydrogen-rich material from the envelope of the red giant or main sequence companion accumulates, it is compressed and heated as a result of the intense gravitational field on the surface of the white dwarf. Eventually, the density at the base

of the accumulated layer becomes so high that matter is supported by electron degeneracy pressure (Section 1.4). As mass transfer proceeds, the temperature at the base of the accreted layer increases and eventually hydrogen burning is ignited (at $T \approx$ (1-2)$\times 10^7$ K [9]) first via the proton-proton chains followed by the CNO and hot-CNO (Section 1.8) cycles. The energy released by these nuclear reactions raises the temperature further, which in the absence of cooling due to expansion, increases the nuclear reaction rates. This positive feedback mechanism leads to an explosive thermonuclear runaway process and the temperature increases exponentially. Once the temperature reaches a point where the degeneracy is lifted the plasma reverts back to an ideal gas and most of the processed nuclear matter (typically 10^{-3}-10^{-5} $M_\odot$ [12]) is ejected into the interstellar medium. Figure 1.7 show an artist's interpretation of an accreting binary system prior to a classical nova explosion.

The maximum temperature reached during a classical nova depends on the initial temperature of the white dwarf and the mass and composition of the accreted envelope of material. The first two of these properties are affected by the white dwarf core composition. For novae systems comprising a C-O white dwarf, maximum temperatures between 0.1 and 0.2 GK are expected, whereas temperatures as high as 0.4 GK are possible in the case of an O-Ne white dwarf [13]. The heightened spectral abundances of elements such as carbon, oxygen and neon in the ejecta of novae (Section 1.7) is indicative of mixing processes between the accreted layer and the surface of the white dwarf [14]. The relative proportion of each element reflects the composition of the white dwarf star, which ultimately depends on the mass of its progenitor as discussed in Section 1.4. Following the outburst associated with a nova explosion, mass accretion resumes and the cycle continues. Recurrence time-scales for classical novae are expected to range from 10^4-10^5 years depending on the mass of the white dwarf and the accretion rate of material onto its surface. If a sufficient amount of matter is transferred onto the surface of an accreting white dwarf star its mass may approach the Chandrasekhar limit [11], possibly triggering a *type-1a supernova* and completely destroying the white dwarf star. It should be noted that the exact mechanism responsible for these events remains unclear.

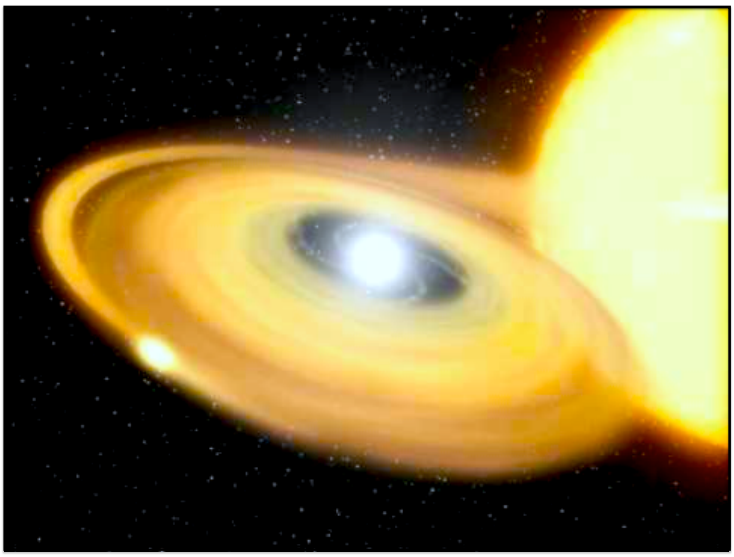

Figure 1.7: Artist's interpretation of a classical nova [15].

1.7 Observational features of classical novae

From an observational perspective, classical novae are characterised by the rapid increase (by 7-20 orders of magnitude [8]) in the luminosity of a pre-existing star. Such events are common and approximately 30 are predicted to occur each year in our galaxy alone [16]. Figure 1.8 shows a typical light curve from a nova event (Sagittarii 2012 [17]), while Figure 1.9 presents an optical image of another recently discovered example [18].

The observed light curves from different novae often exhibit large variations in various aspects of their time evolution, but generally reach a maximum luminosity of 10^4-10^5 $L_\odot$ within only a few days of their initial appearance [19]. This sharp peak in brightness, which persists for a few days at most, is followed by a gradual decline that usually takes place over the course of many weeks.

From analysing optical, ultraviolet and infrared spectra, the majority of observed novae show evidence of an enhanced abundance in isotopes such as carbon, nitrogen and oxygen with respect to solar system values. Approximately 30% of novae are also strongly enriched in neon [12].

Classical novae belong to a wider class of events referred to as *cataclysmic variables*, a category which also includes so-called *dwarf novae*. Dwarf novae are much less luminous than classical novae and are observed with typical recurrence

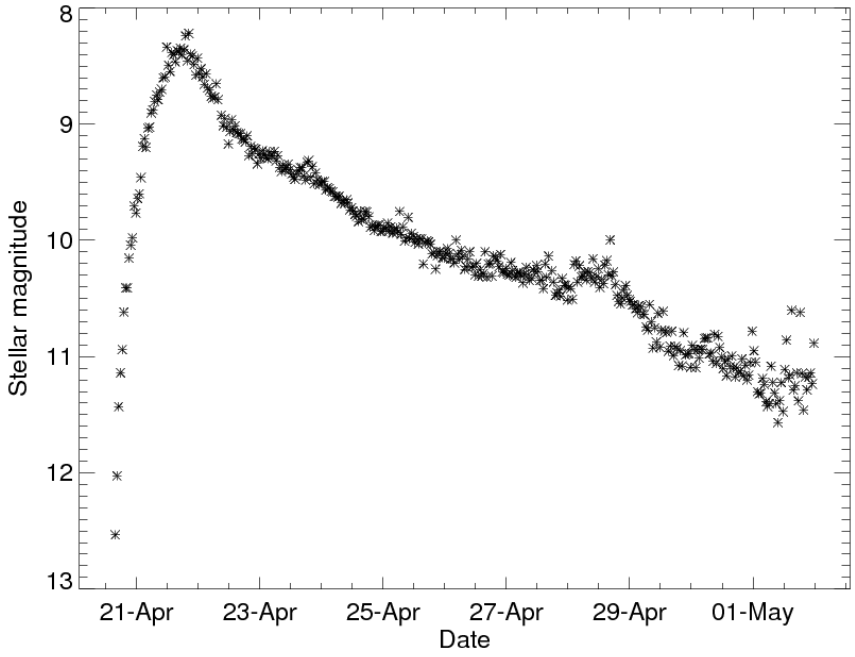

Figure 1.8: Example of the lightcurve (visual magnitude versus time) for a recent nova event (Sagittarii 2012) [17].

times of only 30-300 days [8]. Although dwarf novae and classical novae are believed to originate from the same type of astrophysical site, the physical mechanism underlying each event is believed to be distinctly different.

No classical nova has been observed to occur more than once in the same system. This is presumably because the interval between successive eruptions is greater than the time-scale over which observational records exist.

1.8 The $^{17}O(p,\gamma)^{18}F$ reaction in classical novae

During the thermonuclear runaway episode of a classical nova event, hydrogen burning proceeds predominantly through a chain of fusion reactions referred to as the hot-CNO cycles (Figure 1.10), which operate at temperatures above approximately 0.1 GK. At these elevated temperatures proton-capture reactions on unstable nuclei such as ^{13}N become faster than their β^+ decay, resulting in a transition between hydrogen burning via the CNO1 and hot-CNO cycles.

As indicated in Figure 1.10, the $^{17}O(p,\gamma)^{18}F$ reaction forms part of the hot-CNO cycles, which in addition to (p,γ) and (p,α) reactions also involves the β^+

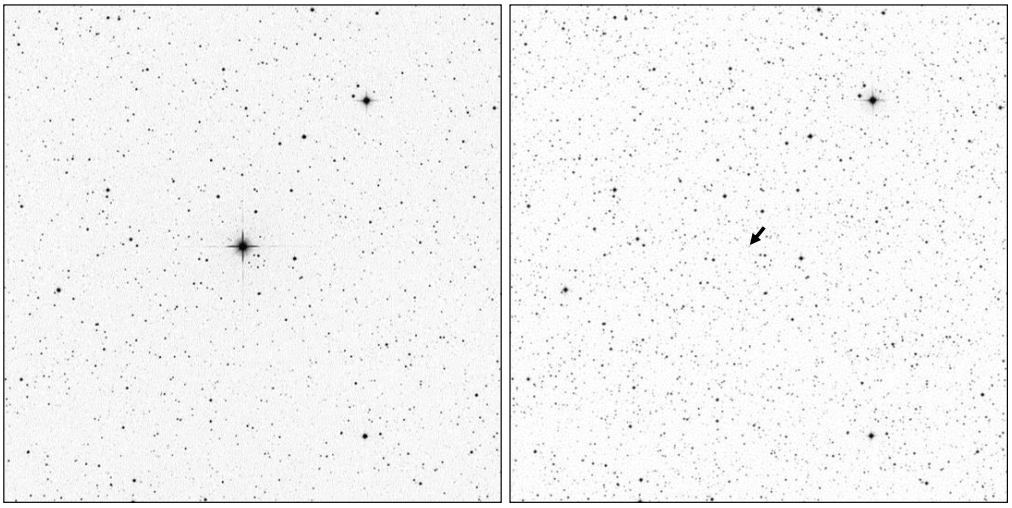

Figure 1.9: Optical image of a recently discovered classical nova of magnitude 6.8 (left-hand panel) [18]. The right-hand panel indicates the same area of sky prior to the appearance of the nova.

decay of ^{14}O and ^{15}O. Since the decay of radioactive isotopes is largely insensitive to temperature, the half-lives of these β^+ unstable nuclei moderate the rate of energy production during the thermonuclear runaway phase of a classical nova. At later stages the energy released as a result of the decay of these nuclei contributes to the ejection of material from the white dwarf.

Although the ^{17}O$(p,\gamma)^{18}$F reaction plays only a minor role in generating energy, its importance relates to the nucleosynthesis of certain rare isotopes, such as ^{15}N, $^{17/18}$O and $^{18/19}$F [13, 20, 21]. Competition between the ^{17}O$(p,\gamma)^{18}$F and the faster ^{17}O$(p,\alpha)^{18}$F reaction (not shown in Figure 1.10) directly governs the synthesis of ^{18}F, which decays to produce ^{18}O. Proton-capture reactions involving ^{18}O subsequently lead to the production of ^{15}N and ^{19}F. Classical novae also represent an important source of pre-solar grains [22], evidence of which has been found in meteoritic samples [23, 24].

The radioactive nucleus ^{18}F is of particular importance as the 511 keV annihilation γ rays following the β^+ decay of ^{18}F ($t_{1/2} = 109.77$ min [25]) could potentially provide an observable signature of novae events. Although ^{18}F is not the only source of 511 keV γ rays produced in classical novae, it is a prime candidate for detection since its relatively long lifetime ($\tau = 158$ minutes) means that the expanding envelope has sufficient time to cool and become transparent

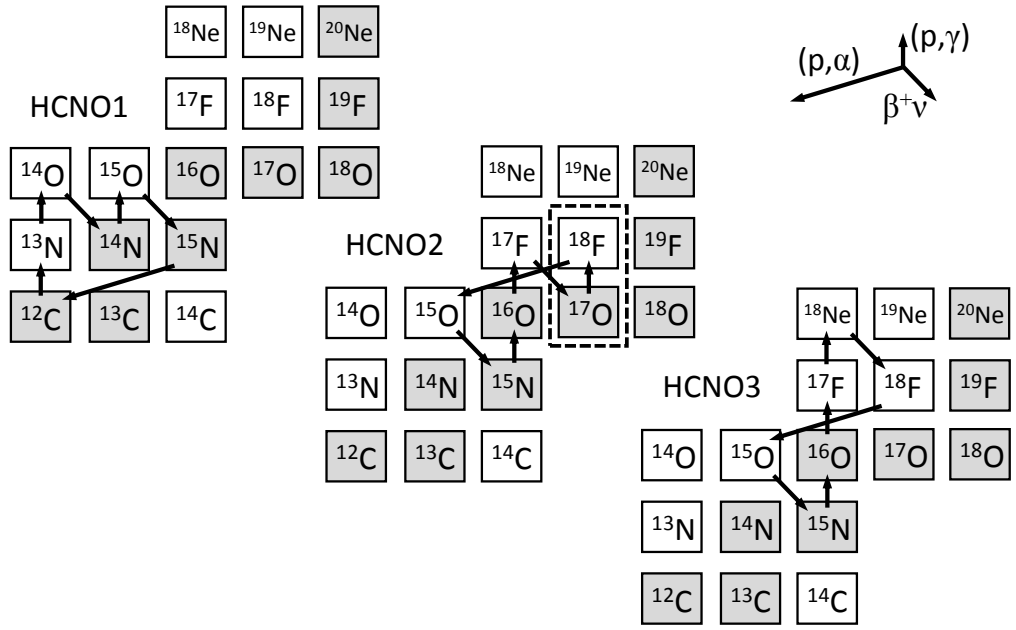

Figure 1.10: The hot-CNO cycles, which operate at temperatures between T = 0.1-0.4 GK during classical novae. The net result of this series of reactions, which includes $^{17}O(p,\gamma)^{18}F$ (dashed box), is the fusion of hydrogen into helium. Stable isotopes are shown in grey.

to γ rays prior to ^{18}F decay.

A simulated γ-ray spectrum from a classical nova explosion is presented in Figure 1.11. The distinct peak at 511 keV mainly originates from positron annihilation following the β^+ decay of ^{18}F, while the continuum at lower energy is largely due to Compton scattering of the γ rays from the decay of para- and ortho-positronium.

If future satellite missions (such as those of the INTEGRAL γ-ray telescope [26]) prove successful in detecting γ rays from the decay of ^{18}F this could provide valuable information regarding the nucleosynthesis and hydrodynamical processes taking place during classical novae, thus constraining existing theoretical models. However, this requires the various reaction rates affecting the production of ^{18}F to be accurately determined, thus providing the motivation for the present experimental study of the $^{17}O(p,\gamma)^{18}F$ reaction[5].

[5]As previously mentioned, the $^{17}O(p,\gamma)^{18}F$ reaction is in direct competition with the $^{17}O(p,\alpha)^{14}N$ reaction, the rate of which is relatively unconstrained at novae temperatures (T = 0.1-0.4 GK). The $^{17}O(p,\alpha)^{14}N$ reaction is presently being studied by the LUNA collaboration.

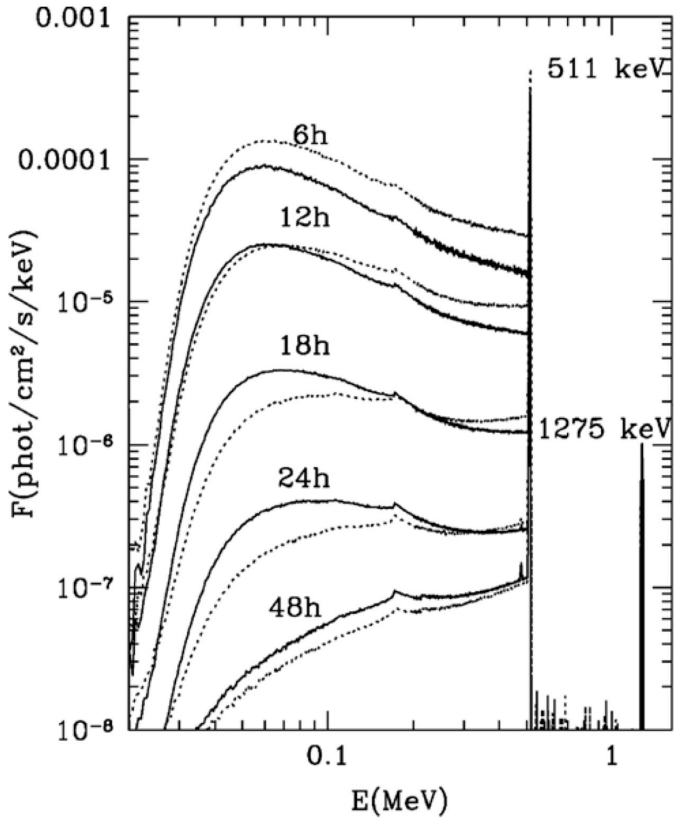

Figure 1.11: Simulated nova spectrum of γ-ray flux (at a distance of 1 kpc) versus energy, at a series of times after the initial event [19]. The peak at 511 keV is predominantly due to positron annihilation following the β^+ decay of ^{18}F. The continuum at lower energies is the result of Compton scattering of the γ rays from the decay of para- and ortho-positronium. The peak at $E_\gamma = 1275$ keV originates from the decay of ^{22}Na.

Chapter 2

Thermonuclear Reactions in Stars

Many different nuclear reactions occur during explosive astrophysical events such as classical novae. The role that a given reaction plays in the energy generation and nucleosynthesis involved in such phenomena is determined by its reaction rate at the temperatures and densities relevant for a given stellar environment. This chapter provides a brief introduction to the theoretical formalism developed to model stellar reaction rates and describes the conceptual foundations on which much of the work presented in this thesis is based.

2.1 Cross sections and stellar reaction rates

The reaction cross section[1], σ, describes the probability that a given reaction will take place and depends on a number of factors such as the strength of the Coulomb barrier existing between the interacting nuclei and the mechanism by which the reaction proceeds.

Consider a generic reaction of the form:

$$a + X \rightarrow Y + b \tag{2.1}$$

or equivalently, $X(a,b)Y$, using the standard shorthand notation. The system consisting of the initial particles, a and X, is referred to as an *entrance channel*,

[1]Cross sections are typically given in units of barn (1 barn = 1×10^{-24} cm^2).

while the particles, Y and b, are referred to as an *exit channel*.

The amount of energy released during a reaction is given by the reaction Q-value, Q, which is defined in terms of the mass difference between the entrance channel and exit channel constituents:

$$Q = [M(a) + M(X) - M(b) - M(Y)]c^2 \tag{2.2}$$

The reaction rate corresponding to the process described above can be expressed as:

$$\mathrm{r}_{aX} = N_{\mathrm{X}} N_{\mathrm{a}} v\sigma(v) \tag{2.3}$$

where r_{aX} is the number of reactions occurring per unit time, in a unit volume of stellar gas consisting of N_{a} particles of type a and N_{X} particles of type X. The cross section, $\sigma(v)$, is written explicitly in terms of the relative velocity, v, between the two particles in the entrance channel. In a stellar plasma, the interacting nuclei exhibit a range of velocities, distributed according to a probability function, $\phi(v)$, which satisfies the condition:

$$\int_0^\infty \phi(v)dv = 1 \tag{2.4}$$

Taking this spread of velocities into consideration, the total reaction rate becomes:

$$\mathrm{r}_{aX} = \mathrm{N_X N_a} \int_0^\infty \phi(v)v\sigma(v)dv \equiv \mathrm{N_X N_a} < \sigma v >_{aX} \tag{2.5}$$

where $< \sigma v >_{aX}$ is defined as the *reaction rate per particle pair*.

The energy available for a reaction to take place is determined by the temperature of the particular stellar environment under consideration. For stellar interiors, temperatures are sufficiently high that matter can be treated as fully ionised and the plasma is well approximated by an ideal gas, *i.e.* a mixture of free, non-interacting particles. This approximation requires the further assumption that nuclei are non-degenerate (Chapter 1) and that their motion can be treated as non-relativistic. For an ideal gas, the relative velocity of interacting nuclei is described by the Maxwell-Boltzmann (M-B) distribution:

$$\phi(v) = 4\pi v^2 \left(\frac{\mu}{2\pi kT}\right)^{\frac{3}{2}} \exp\left(-\frac{\mu v^2}{2kT}\right) \tag{2.6}$$

where T denotes absolute temperature and k represents the Boltzmann constant. The reduced mass of the system, μ, is defined as $\mu = m_{\mathrm{a}} m_{\mathrm{X}}/(m_{\mathrm{a}}+m_{\mathrm{X}})$. Alternatively, Equation 2.6 can be expressed in terms of kinetic energy, E, as:

$$\phi(E) \propto E\exp\left(-\frac{E}{kT}\right) \tag{2.7}$$

Inserting this Maxwellian energy distribution into Equation 2.5, the reaction rate per particle pair becomes:

$$< \sigma v >= \left(\frac{8}{\pi\mu}\right)^{\frac{1}{2}} \frac{1}{(kT)^{\frac{3}{2}}} \int_0^\infty \sigma(E) E \exp\left(-\frac{E}{kT}\right) dE \tag{2.8}$$

As previously mentioned, the reaction cross section, $\sigma(E)$, in Equation 2.8 depends on the mechanism by which the reaction proceeds at a given energy. All nuclear processes contributing to the total reaction cross section can be classified as either *resonant* or *non-resonant*, the distinction between which is discussed in the following sections.

2.2 Non-resonant reactions induced by charged particles

In order to undergo a nuclear reaction, charged particles must possess sufficient energy to penetrate the potential barrier that exists between them. This potential consists of two main components: the repulsive Coulomb potential between two positively charged nuclei and the centrifugal barrier associated with their relative orbital angular momentum. The Coulomb potential experienced by two particles of charge Z_{a} and Z_{X}, separated by a distance r is given by:

$$V_c(r) = \frac{Z_a Z_X e^2}{4\pi\epsilon_0 r} \tag{2.9}$$

where e is the fundamental elementary charge and ϵ_0 is the *permittivity of free space*.

The centrifugal barrier between two particles with relative orbital angular

momentum, l, is written as:

$$V_{cf}(r) = \frac{l(l+1)\hbar^2}{2\mu r^2} \tag{2.10}$$

where the reduced Plank constant is denoted by $\hbar$.

Figure 2.1 shows the total potential for the $p + {}^{17}\mathrm{O}$ entrance channel assuming a relative orbital angular momentum of $l = 1$ (p-wave transmission). The *height* of the potential barrier, E_B, is equivalent to the total potential calculated at the nuclear interaction distance[2], R_n, which represents the point of transition between the long range repulsive potential defined by Equations 2.9 and 2.10 and the attractive nuclear potential resulting from the strong force. No exact analytical form exists for the strong nuclear potential, which is often approximated using a square-well or a Woods-Saxon function. A schematic representation of the combined potential arising from the strong, Coulomb and centrifugal components is shown in Figure 2.2.

From a classical point of view, interacting charged particles (with zero relative angular momentum) must acquire an energy greater than the Coulomb barrier *height*, E_C, in order for a nuclear reaction to take place[3]. However, from a quantum mechanical perspective the Coulomb barrier can be penetrated at energies much lower than E_C through a process referred to as *quantum mechanical tunnelling*. Taking this effect into consideration, the probability of barrier penetration is given by the Gamow Factor, P_G:

$$P_\mathrm{G} = \exp(-2\pi\eta) \tag{2.11}$$

where η is the Sommerfeld parameter and the term $2\pi\eta$ can be written as:

$$2\pi\eta = 31.29 Z_1 Z_2 \left(\frac{\mu}{E}\right)^{\frac{1}{2}} \tag{2.12}$$

with the centre of mass energy, E, given in units of keV and μ in atomic mass units[4] (amu). It should be noted that Equation 2.11 is an approximation, which is only valid for s-wave (l=0) transmission at energies that are small compared to the Coulomb barrier height, *i.e.* $E \ll E_\mathrm{C}$.

[2]The nuclear interaction distance can be approximated by $R_\mathrm{n} = R_0(A_1^{1/3} + A_2^{1/3})$ where R_0 = 1.3 fm and A_i is the atomic mass number of the interacting nuclei [9].

[3]For the ${}^{17}\mathrm{O} + p$ reaction this would require temperatures greater than T = 10 GK.

[4]1 amu = 931.49 MeV/c^2.

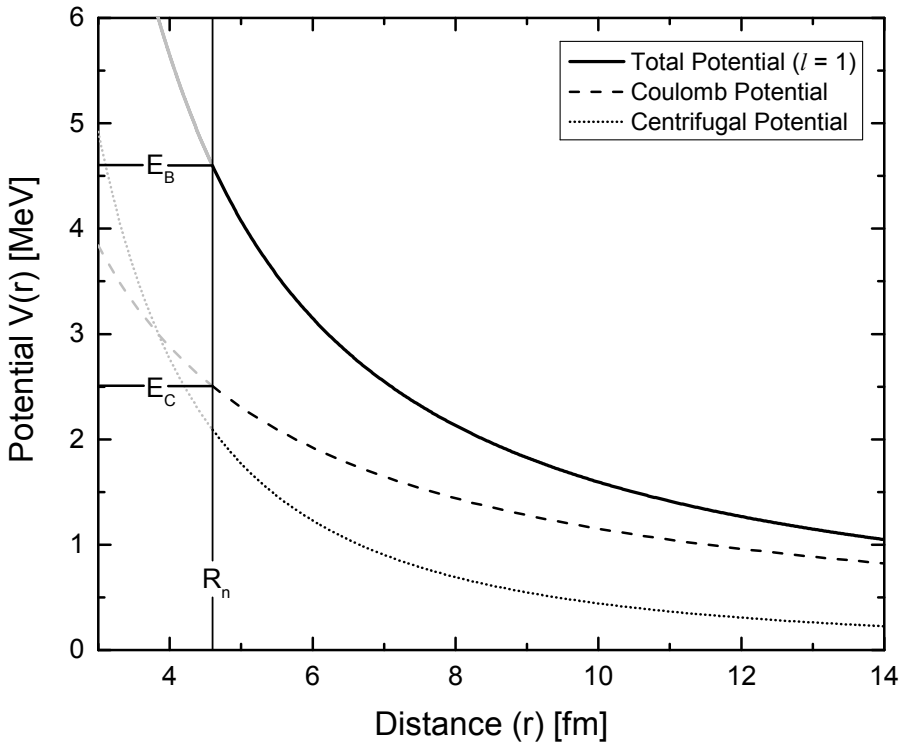

Figure 2.1: The Coulomb and centrifugal components of the potential felt by the entrance channel particles of the ^{17}O(p,γ)^{18}F reaction, assuming a relative orbital angular momentum of $l = 1$. The potential barrier height, E_{B} is evaluated at the nuclear interaction distance, R_{n}. The height of the Coulomb barrier is represented by E_{C}. In this case, $R_{\mathrm{n}} \approx 4.6$ fm, $E_{\mathrm{C}} \approx 2.5$ MeV and $E_{\mathrm{B}} \approx 4.5$ MeV.

The non-resonant cross section can be expressed in terms of the barrier penetrability as:

$$\sigma(E) = \frac{1}{E}\exp(-2\pi\eta)S(E) \tag{2.13}$$

where the $1/E$ is a non-nuclear term[5] related to the de Broglie wavelength, λ. The final term appearing in Equation 2.13 is the astrophysical S-factor, $S(E)$, which is introduced to account for the purely nuclear component of the cross section. Expressing the cross section in this form allows the energy dependence to be largely factored out. For non-resonant reactions, $S(E)$ is a smoothly varying function of energy and much more amenable to extrapolation than $\sigma(E)$, as

[5]From purely geometrical considerations, the cross section for two colliding particles is related to the reduced de Broglie wavelength, $\lambda\!\!\!^{-}$, by the expression: $\sigma(E) \propto \pi\lambda\!\!\!^{-2} \propto 1/E$.

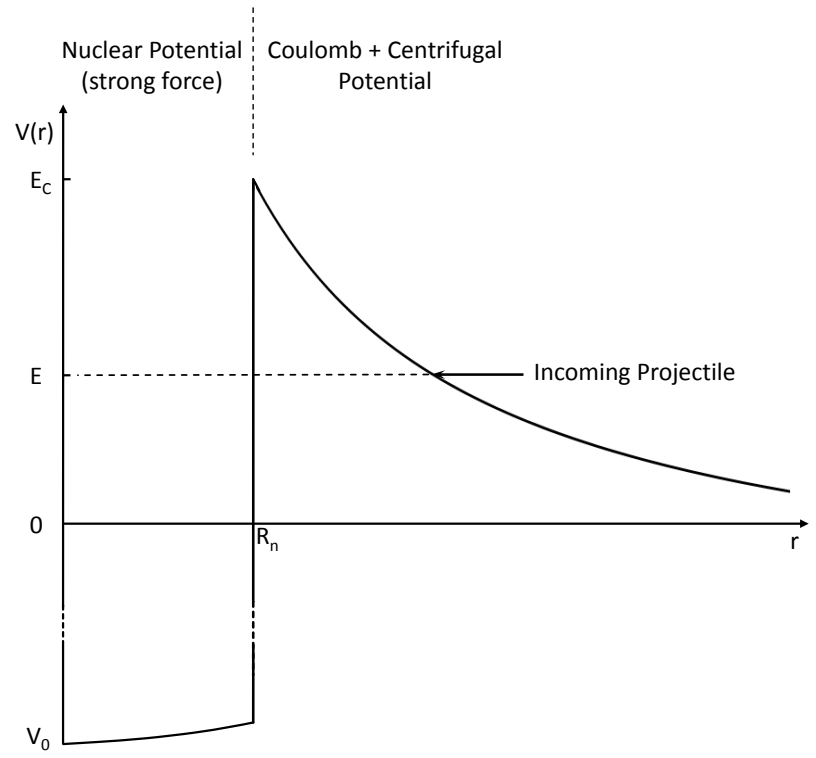

Figure 2.2: Schematic representation of the combined Coulomb, centrifugal and nuclear potentials experienced by two interacting nuclei. In overcoming the potential barrier, an incoming projectile enters a region ($r < R_{\mathrm{n}}$) dominated by strong nuclear force.

demonstrated in Figure 2.3.

Substituting Equation 2.13 into the previous expression for the non-resonant reaction rate per particle pair (Equation 2.8) gives:

$$< \sigma v >= \left(\frac{8}{\pi\mu}\right)^{\frac{1}{2}} \frac{1}{(kT)^{\frac{3}{2}}} \int_0^\infty S(E)\exp\left(-\frac{E}{kT} - 2\pi\eta(E)\right) dE \qquad (2.14)$$

where the term, exp(-E/kT), originates from the M-B distribution of particles energies, and exp(-$2\pi\eta$) parameterises the probability of penetrating the Coulomb barrier. The energy, E_0, corresponding to the maximum reaction rate at a given temperature can be calculated by differentiating Equation 2.14.

The product of the two exponential terms in Equation 2.14 leads to a peak in the reaction rate, referred to as the *Gamow Peak*, as illustrated for the

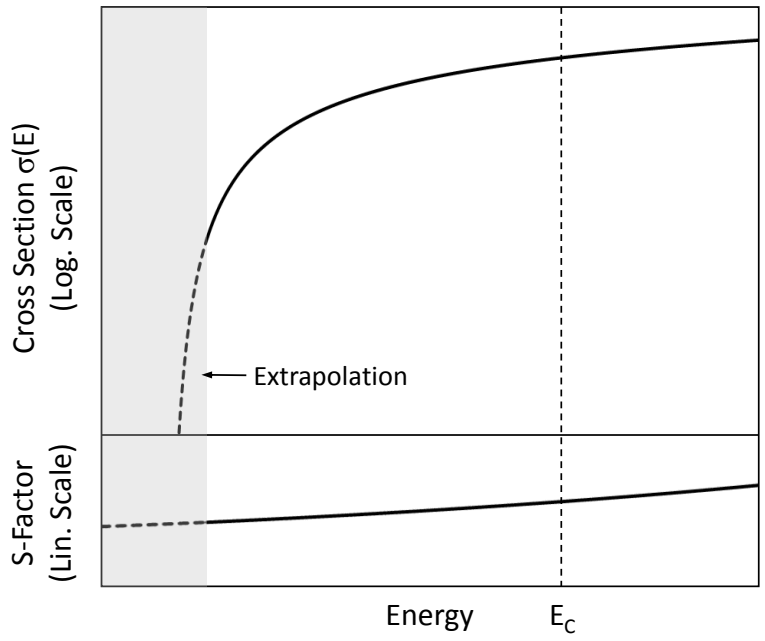

Figure 2.3: The cross section (upper plot) and the corresponding astrophysical S-factor (lower plot) for a typical non-resonant reaction. The grey area represents the region of astrophysical importance where data extrapolation is required. The S-factor is more accurately extrapolated down to these low energies than the cross section.

^{17}O(p,γ)^{18}F reaction in Figure 2.4. The shape of the Gamow peak can be approximated using a Gaussian function (Figure 2.4, lower panel):

$$\exp\left(-\frac{E}{kT}-\frac{b}{\sqrt{E}}\right)=A\exp\left(\frac{-(E-E_0)^2}{\left(\frac{\Delta E_0}{2}\right)^2}\right) \tag{2.15}$$

where $b=(2\mu)^{1/2}\pi \mathrm{e}^2 Z_\mathrm{a} Z_\mathrm{X}/\hbar$ and ΔE_0 is the $1/e$ width of the Gamow peak. Differentiating Equation 2.15, setting to zero and solving for E_0 yields:

$$E_0=\left(\frac{bkT}{2}\right)^{\frac{2}{3}}=1.22(Z_a^{\,2}Z_X^{\,2}\mu T_6^{\,2})^{\frac{1}{3}}\ \ (\mathrm{keV}) \tag{2.16}$$

where T_6 is a shorthand notation for $T\times10^6$ K. The energy E_0 is located well above the mean thermal energy, kT.

The width of the Gamow peak, ΔE_0, is given by the expression:

$$\Delta E_0=\frac{4}{\sqrt{3}}(E_0kT)^{\frac{1}{2}}=0.749(Z_1^{\,2}Z_2^{\,2}\mu T_6^{\,5})^{\frac{1}{6}}\ \ (\mathrm{keV}) \tag{2.17}$$

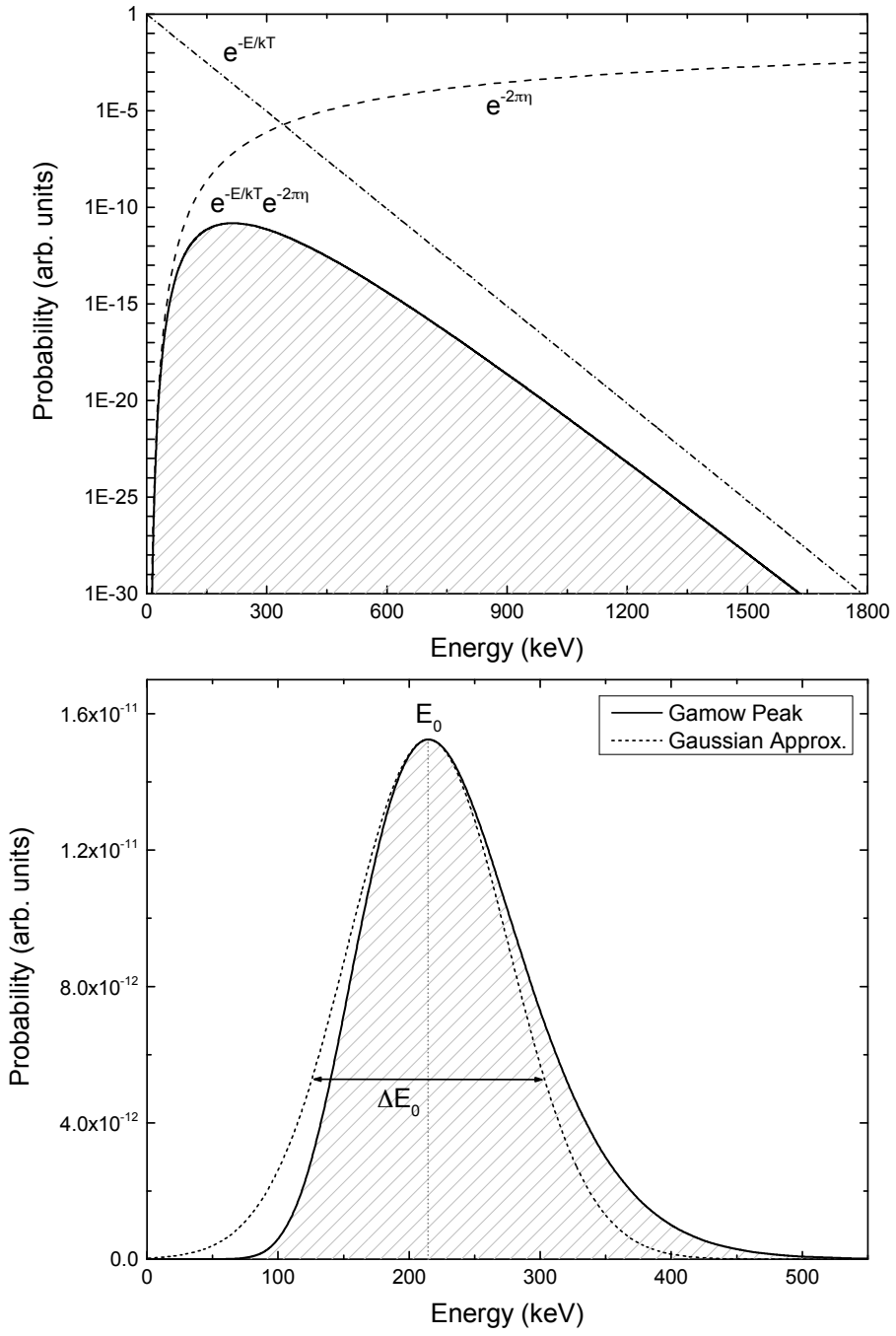

Figure 2.4: The Gamow peak (shaded area) calculated for the ^{17}O$(p,\gamma)^{18}$F reaction at a temperature of $T = 0.3$ GK (appropriate for classical novae). The terms associated with the M-B distribution of particle velocities and the Gamow factor modelling the probability of penetrating the Coulomb barrier are also plotted. Lower panel: A linear scale plot of the Gamow peak (solid line). The Gamow energy, E_0, and Gamow peak width, ΔE_0, are determined from a Gaussian approximation (dotted line).

The narrow energy range defined by ΔE_0 is often referred to as the *Gamow window* and, for the purposes of nuclear astrophysics, defines the temperature range in which the cross section of a reaction should be determined[6]. In the case of classical novae, outburst temperatures are predicted to range from $T = 0.1$-0.4 GK as described in Chapter 1. For these conditions the centroid of the Gamow peak for the $^{17}\mathrm{O}(p,\gamma)^{18}\mathrm{F}$ reaction lies between $E_{\mathrm{cm}} = 100$-260 keV.

2.3 Narrow resonance reaction formalism

So far our discussion has been limited to the non-resonant reaction mechanism, which can take place at any interaction energy. Alternatively, a reaction may proceed through the formation of an excited state of energy E_{x} in a compound nucleus, C, if the energy present in the entrance channel closely corresponds to the energy of a state in the compound nucleus (Figure 2.5). Such reactions are referred to as resonant and occur in a 2-step process (formation and decay of the excited compound nucleus, C^*):

$$a + X \rightarrow C^* \rightarrow Y + b \tag{2.18}$$

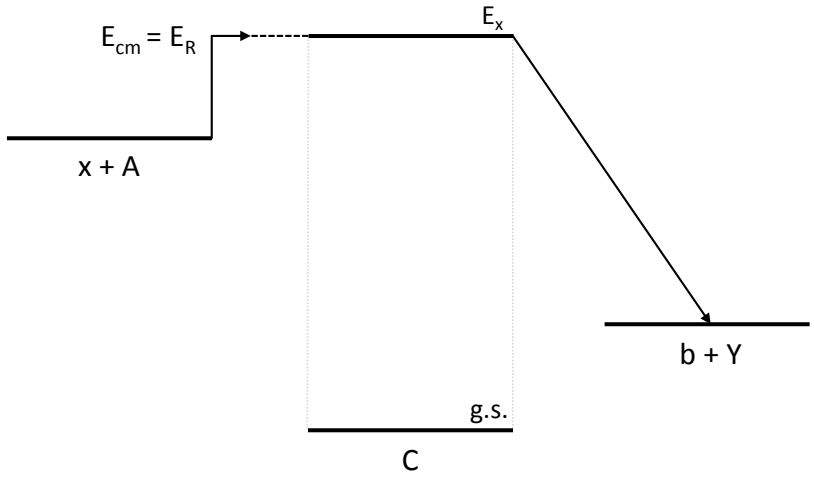

Figure 2.5: Energy level diagram depicting a resonant reaction proceeding through the formation of an excited state in the compound nucleus, C.

[6]Strictly speaking this is only true for non-resonant reactions as the presence of resonances can change the energy at which a reaction most likely occurs, as discussed in Chapter 4.

In addition to the condition that $E_{\mathrm{cm}} = E_{\mathrm{R}}$ (the resonance energy in the centre of mass reference frame), conservation of angular momentum and parity requires that:

$$\begin{aligned} \vec{J} &= \vec{J_a} + \vec{J_X} + \vec{l} \\ \pi(J) &= \pi(J_a)\pi(J_X)(-1)^l \end{aligned} \tag{2.19}$$

where $\vec{J}$ represents the angular momentum (spin) of the resonant state formed in the compound nucleus. The angular momenta of the entrance channel particles are represented by $\vec{J}_{\mathrm{a}}$ and $\vec{J}_{\mathrm{X}}$ while $\vec{l}$ is the relative orbital angular momentum existing between them.

Resonances can significantly enhance the cross section of a reaction (sometimes by several orders of magnitude) and become particularly important if they fall within the Gamow energy region. The cross section associated with a given resonance is directly proportional to the probability of forming the corresponding excited state in the compound nucleus combined with the probability of the subsequent de-excitation of this state via a particular decay channel. Consistent with Heisenberg's uncertainty principle, these formation and decay probabilities are represented by energy quantities known as partial widths, Γ_i. The total width, Γ, of a resonance is obtained by summing the partial widths associated with all energetically allowed decay channels.

The cross section for a single, isolated[7], resonance is given by the Breit-Wigner formula:

$$\sigma_{\mathrm{BW}}(E) = \pi\lambda\!\!\!^{-2}(1+\delta_{aX})\frac{(2J+1)}{(2J_X+1)(2J_a+1)}\frac{\Gamma_a\Gamma_b}{(E-E_R)^2+\frac{1}{4}\Gamma^2} \tag{2.20}$$

where E_{R} is the centre of mass energy of the resonance and $\lambda\!\!\!^{-}$ represents the reduced de Broglie wavelength, in the centre of mass reference frame. The partial width of the entrance channel is denoted as Γ_{a}, while Γ_{b} refers to the specific decay channel under consideration. The total width is given by Γ. The term containing the Kronecker delta, δ_{aX}, accounts for the possibility of identical

[7]A resonance is referred to as isolated if its width is much smaller than the energy gap between adjacent states. In situations where a large number of partially overlapping resonances are populated simultaneously, a different theoretical treatment is required [27].

particles in the entrance channel.

Inserting Equation 2.20 into Equation 2.8 yields the result:

$$\begin{aligned} < \sigma v > &= \left(\frac{8}{\pi\mu}\right)^{\frac{1}{2}} \frac{1}{(kT)^{\frac{3}{2}}} \int_0^\infty \sigma_{\mathrm{BW}}(E) E \exp\left(-\frac{E}{kT}\right) dE \\ &= \frac{\sqrt{2\pi}\hbar^2}{(\mu kT)^{\frac{3}{2}}} \omega \int_0^\infty \frac{\Gamma_a \Gamma_b}{E - (E_R)^2 + \frac{1}{4}\Gamma^2} \exp\left(-\frac{E}{kT}\right) dE \end{aligned} \tag{2.21}$$

where $\omega = (1+\delta_{\mathrm{aX}})(2J+1)/[(2J_{\mathrm{X}} + 1)(2J_{\mathrm{a}} + 1)]$.

If the energy E_{R} is much greater than the total width of the resonance, Γ, the resonance is referred to as *narrow*. For narrow resonances, the M-B factor and partial widths are approximately constant over the energy range spanned by the resonance allowing the resonant reaction rate to be written as:

$$< \sigma v > = \frac{\sqrt{2\pi}\hbar^2}{(\mu kT)^{\frac{3}{2}}} \exp\left(-\frac{E_R}{kT}\right) \omega \frac{\Gamma_a \Gamma_b}{\Gamma} 2 \int_0^\infty \frac{\Gamma/2}{(E_R - E) + \frac{1}{4}\Gamma^2} dE \tag{2.22}$$

where the partial widths outside the integral are calculated at the resonance energy, $E = E_{\mathrm{R}}$. Evaluating Equation 2.22 and making a further simplification by replacing the ratio of widths by the factor, $\gamma = \Gamma_{\mathrm{a}}\Gamma_{\mathrm{b}}/\Gamma$, leads to the expression:

$$< \sigma v > = \left(\frac{2\pi}{\mu kT}\right)^{\frac{3}{2}} \hbar^2 \exp\left(-\frac{E_R}{kT}\right) \omega\gamma \tag{2.23}$$

where $\omega\gamma$ is referred to as the *resonance strength*:

$$\omega\gamma = (1 + \delta_{aX}) \frac{2J + 1}{(2J_X + 1)(2J_a + 1)} \frac{\Gamma_a \Gamma_b}{\Gamma} \tag{2.24}$$

2.4 Broad resonance reaction formalism

As stated in the previous section, treating the widths appearing in Equation 2.21 as constant is only appropriate for narrow resonances. If the resonance is relatively broad ($\Gamma/E_{\mathrm{R}} \geq 0.1$) then the energy dependence of these widths is no longer negligible and must be taken into consideration when calculating the cross

section. This is achieved by modifying Equation 2.20 as follows:

$$\sigma_{\mathrm{BW}}(E) = \sigma_{\mathrm{BW}}(E_R)\frac{E_R}{E}\frac{\Gamma_a(E)}{\Gamma_a(E_R)}\frac{\Gamma_b(E)}{\Gamma_b(E_R)}\frac{\left(\frac{1}{2}\Gamma(E_R)\right)^2}{(E-E_R)^2+\left(\frac{1}{2}\Gamma(E)\right)^2} \tag{2.25}$$

where $\sigma(E_{\mathrm{R}})$ is the cross section evaluated at the resonance energy, $E = E_{\mathrm{R}}$.

The partial width energy dependence associated with particle (as opposed to electromagnetic) emission or absorption is well approximated by the *penetration factor*, $P(E)$, which must be evaluated numerically by computing the *Coulomb wave functions* [28]. The partial widths associated with processes producing γ rays varies as E_γ^{2l+1} (the γ-ray energy to the power of $2l$+1). Substituting these quantities into Equation 2.25 and assuming the exit channel involves γ-ray emission, leads to the expression:

$$\sigma_{\mathrm{BW}}(E) = \sigma_{\mathrm{BW}}(E_R)\frac{E_R}{E}\frac{P_a(E)}{P_a(E_R)}\frac{E_\gamma^{2l+1}(E)}{E_\gamma^{2l+1}(E_R)}\frac{\left(\frac{1}{2}\Gamma(E_R)\right)^2}{(E-E_R)^2+\left(\frac{1}{2}\Gamma(E)\right)^2} \tag{2.26}$$

The reaction rate associated with populating a broad resonance can be determined by substituting Equation 2.26 into Equation 2.21 and numerically integrating.

Calculating the total reaction rate is often complicated by the presence of multiple resonances inside the effective energy region and/or tails from broad resonances at higher energies. Figure 2.6 illustrates a typical situation, where both broad and narrow resonances contribute to the measured S-factor. Sub-threshold resonances can also have an influence if their high energy tails extend beyond the threshold energy. Any interference effects between resonances with the same spin and parity must also be taken into account.

As we shall see in the following section, the $^{17}\mathrm{O}(p,\gamma)^{18}\mathrm{F}$ reaction proceeds via both resonant and non-resonant processes at the energies relevant for classical novae.

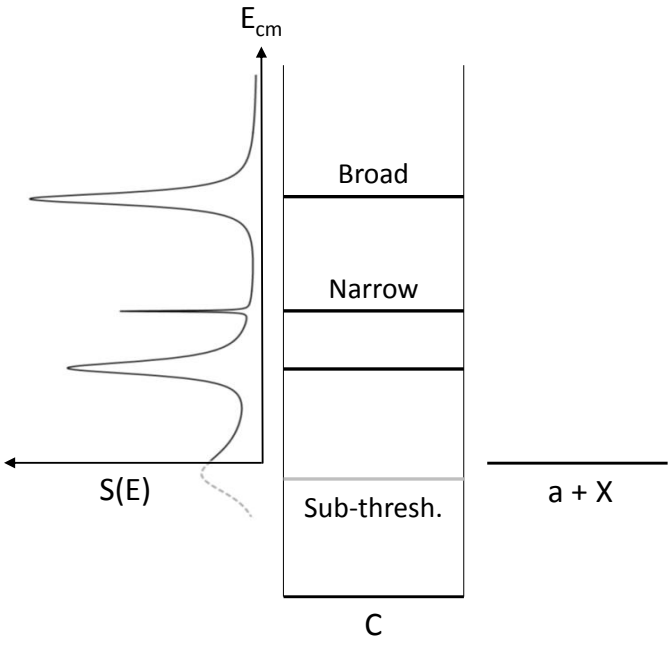

Figure 2.6: The astrophysical S-factor as a function of energy for a typical reaction that proceeds through the formation of narrow, broad and sub-threshold resonances.

2.5 The ^{17}O(p,γ)^{18}F reaction

The non-resonant component of the ^{17}O(p,γ)^{18}F reaction takes place via the direct capture (DC) reaction mechanism. This process involves prompt γ-ray emission due to the formation of ^{18}F directly from the entrance channel (p + ^{17}O). The energy of these γ rays are equal to the energy difference between the entrance channel and the state populated in ^{18}F. An energy level diagram depicting the DC reaction mechanism is shown alongside the equivalent diagram for a resonant (p,γ) reaction in Figure 2.7.

Gamma rays associated with the formation of a state in ^{18}F are referred to as *primary* γ rays, while those resulting from the state's subsequent decay are referred to as *secondary* γ rays. This distinction is important for the present study of the ^{17}O(p,γ)^{18}F reaction as will become apparent in Chapter 6. The specific transitions that can occur are determined by the selection rules governing the conservation of spin and parity.

The direct capture (DC) process strongly contributes to the ^{17}O(p,γ)^{18}F reaction rate at energies inside the classical novae Gamow window ($E_{\rm cm}$ = 100-

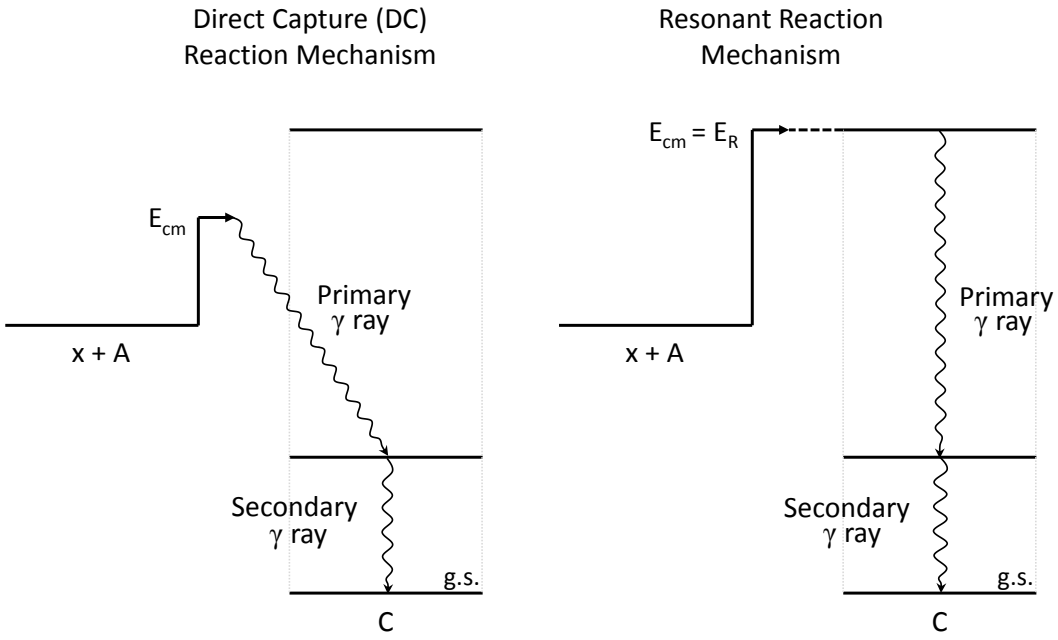

Figure 2.7: Energy level diagrams illustrating the direct capture (DC) and resonant reaction mechanisms.

260 keV). In this energy range, the total cross section is further enhanced by the tails of two broad resonances located at $E_{\mathrm{R}} = 577$ keV and $E_{\mathrm{R}} = 677$ keV, corresponding to states in ^{18}F at $E_x = 6163.2$ keV and $E_x = 6283.2$ keV, respectively. Since this contribution arises from the low energy tail of these two resonances, the resultant cross section varies relatively smoothly with energy. It is therefore convenient to group the broad resonant and DC components of the $^{17}\mathrm{O}(p,\gamma)^{18}\mathrm{F}$ reaction under the heading of 'non-resonant process'. This helps in distinguishing the above contributions from that of a single narrow resonance populated at an energy of $E_{\mathrm{R}} = 183$ keV (corresponding to the $E_x = 5789.8$ keV state in ^{18}F). This resonance is located directly inside the Gamow window for classical novae and represents an important contribution to the total $^{17}\mathrm{O}(p,\gamma)^{18}\mathrm{F}$ reaction rate.

The resonant and non-resonant processes described above may each lead to the formation of various excited states in ^{18}F, which then decay to the ground state via γ-ray decay cascades. Figure 2.8 shows the energy level scheme for ^{18}F, where only the resonant states relevant to the present study are shown.

The following chapter summarises the previous experimental investigations of

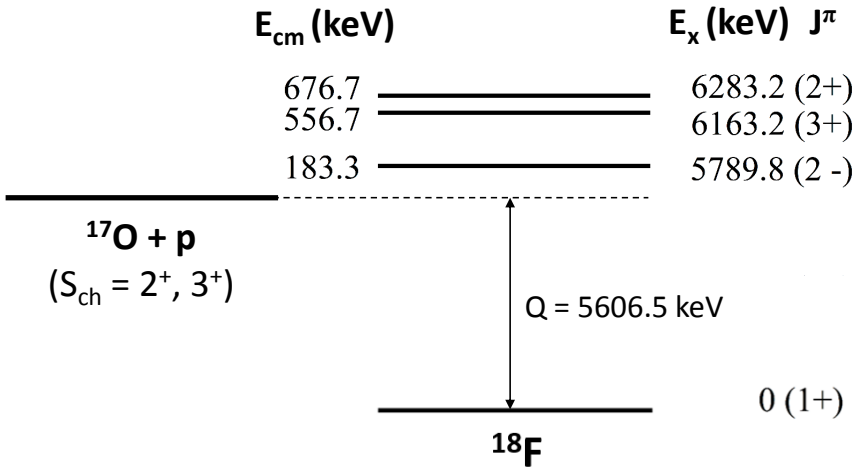

Figure 2.8: The energy level scheme for ^{18}F (information from [29]). Only the three resonances relevant to the present study are shown. The entrance channel spin is denoted by S_{ch}.

the resonant and non-resonant components of the ^{17}O$(p,\gamma)^{18}$F reaction.

Chapter 3

Current Status of the $^{17}O(p,\gamma)^{18}F$ Reaction

Several experimental studies have been dedicated to measuring the cross section of the $^{17}O(p,\gamma)^{18}F$ reaction, given its importance for astrophysical events such as classical novae. The corresponding reaction rate remains relatively uncertain, due to a lack of accurate experimental data at sufficiently low energy.

3.1 Non-resonant component of the $^{17}O(p,\gamma)^{18}F$ reaction

The first measurement of the $^{17}O(p,\gamma)^{18}F$ reaction was performed by C. Rolfs in 1973 [30] using a proton beam impinging on a solid, ^{17}O enriched, Ta_2O_5 target. Proton currents between 120-200 μA were provided by two separate Van de Graaff accelerators at the University of Toronto, Canada and McMaster University, Canada. This combination allowed for measurements of the total $^{17}O(p,\gamma)^{18}F$ reaction cross section over a large energy range, E_{cm} = 300-1900 keV. The angular distributions of DC γ-ray transitions to several states in ^{18}F were measured using two HPGe detectors placed at 0° and 90° with respect to the beam axis. These measurements provided information on the level structure of ^{18}F in good agreement with shell model calculations. The yield of the strongest ^{18}F transition, 937→0 keV, was used to calculate the total cross section relative[1]

[1]Relative measurements such as this benefit from reduced systematic uncertainties, providing an identical experimental setup is used in both cases.

to that of the accurately known ^{16}O(p,γ)^{17}F reaction, measured in the same study [30].

Figure 3.1 shows the cross section measured in [30] as a function of proton energy. The two broad resonances at $E_{\mathrm{R}} = 557$ and 677 keV are indicated. In order to extract the purely DC component of the ^{17}O(p,γ)^{18}F reaction, Rolfs sought to identify the energies at which the cross section was free from the influence of these resonances. This was deemed to be the case for the points in Figure 3.1 above approximately $E_{\mathrm{p}} = 1.4$ MeV. The S-factor corresponding to these high energy data (lower plot of Figure 3.1) was fitted using a standard theoretical formalism developed to describe the DC reaction mechanism [31]. For this calculation Rolfs opted to approximate the nuclear interior using a square-well potential. The resultant fit (solid line in lower plot of Figure 3.1) was extrapolated to lower energies relevant for stellar astrophysics and found to be in fairly good agreement with the S-factor values associated with the four lowest energy points around $E_{\mathrm{p}} = 400$ keV (boxed in Figure 3.1).

However, a subsequent study performed by Fox *et al.* [32, 33] suggested that the low energy data obtained by Rolfs may be affected by the tails of the two broad resonances at $E_{\mathrm{R}} = 557$ and 677 keV. This assertion was supported by a refined analysis of the DC reaction mechanism. By using a more realistic Woods-Saxon potential (as opposed to the square-well approximation of Rolfs), Fox *et al.* demonstrated that the predicted DC S-factor at an energy of E_{cm}= 200 keV was up to 45% lower and displays a different energy dependence. Thus, it seems implausible that the four lowest energy points measured by Rolfs arise from purely DC processes. Interestingly, Fox *et al.* were unable to reproduce the DC S-factor fit presented by Rolfs using either a square-well or Wood-Saxon potential, which further questioned the reliability of the conclusions reached in [30]. Fox *et al.* adopted an alternative approach to determine the DC contribution that did not rely on information obtained in [30]. This involved calculating the absolute DC S-factor on a purely theoretical basis[2], where the only experimental inputs required were the spectroscopic factors associated with the transitions to each relevant state in ^{18}F. Fox *et al.* determined the following parameterisation for the DC S-factor, valid for energies below $E_{\mathrm{cm}} = 1$ MeV:

[2]A detailed discussion of this calculation is beyond the scope of this thesis and can be found for example in [34].

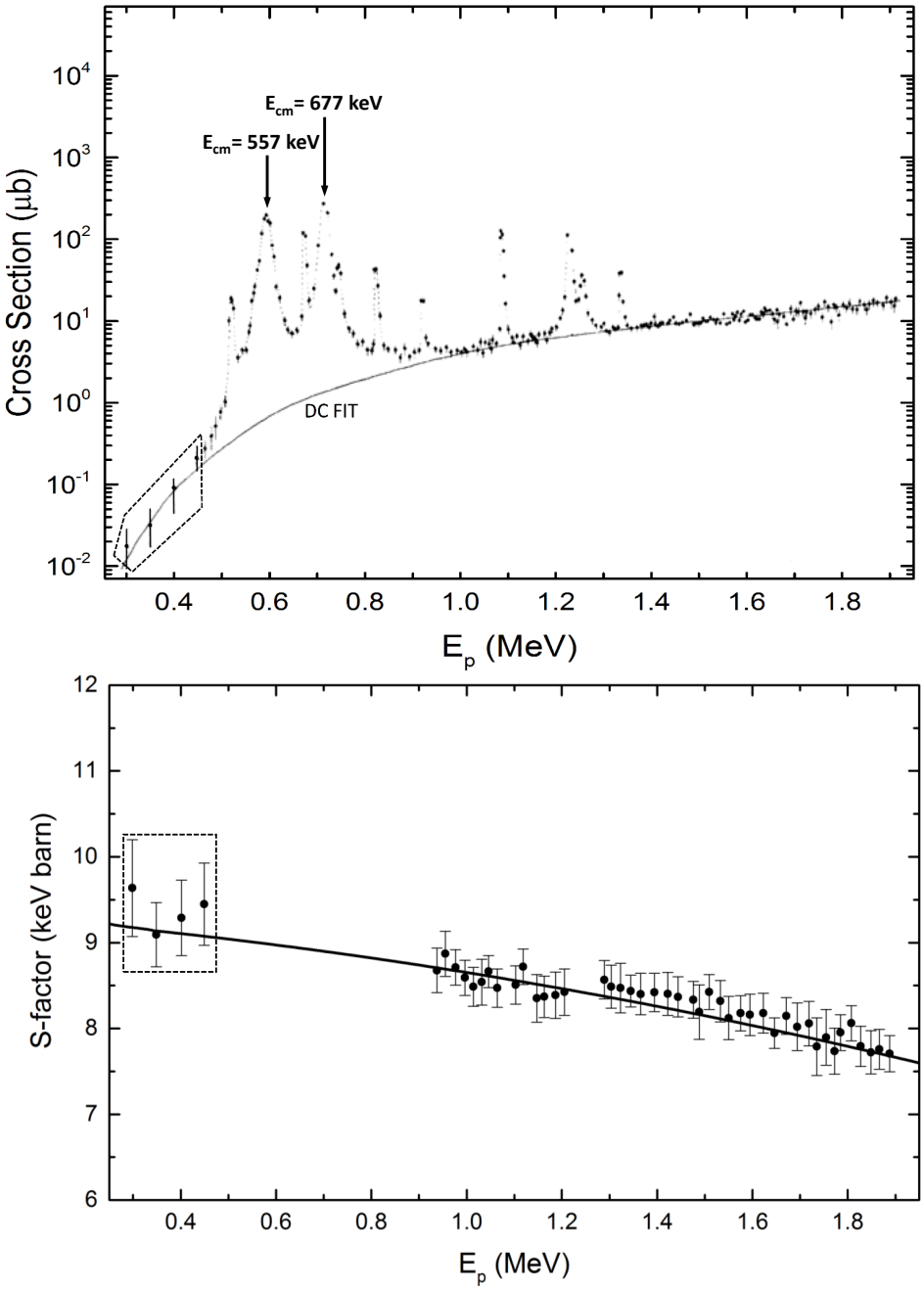

Figure 3.1: The $^{17}O(p,\gamma)^{18}F$ reaction cross section (upper plot) and corresponding S-factor (lower plot) measured in [30] (adapted from Figures 11 and 17 in [30]). The broad resonances at $E_R = 557$ keV and $E_R = 677$ keV are indicated. The four lowest points measured by Rolfs [30] are boxed.

$$S_{DC}(E) = 3.74 + (6.76 \times 10^{-4})E - (2.5 \times 10^{-7})E^2 \quad (3.1)$$

with E in keV and S in keV barn. However, because of the relatively large uncertainties (estimated as 50% on average) associated with the spectroscopic factors used in calculating the above result, the total S-factor parameterisation presented in [33] is unreliable.

An independent re-analysis of the existing data was undertaken in a subsequent study performed by Chafa *et al.* [35, 36]. Key to this effort was correcting the four lowest energy points of [30] for the contribution from the tails of the two broad resonances at $E_{\mathrm{R}} = 557$ and 677 keV. The broad resonance component of the total S-factor was estimated using the standard Breit-Wigner formalism (Chapter 2) and energy dependent partial widths taken from [25] and [37]. This calculation resulted in S-factor corrections of approximately 20-50% to Rolfs' four original low-energy data points. Chafa *et al.* included these corrected data in fitting the DC S-factor, the result of which is shown in Figure 3.2. Their fit deviates significantly from the high energy measurements of [30] between approximately $E_{\mathrm{cm}} = 0.9$-1.8 MeV. In order to explain this discrepancy, Chafa *et al.* suggested that, like the low energy points discussed above, the data around $E_{\mathrm{cm}} = 1$ MeV were also affected by the presence of the $E_{\mathrm{R}} = 557$ and 677 keV broad resonances. However, Chafa *et al.* did not include this further correction (estimated to be up to 15%) in their final fit.

Chafa *et al.* also performed the first experimental measurement of the $^{17}\mathrm{O}(p,\gamma)^{18}\mathrm{F}$ reaction at energies inside the Gamow window for classical novae. Instead of detecting prompt γ rays, the measurements of [36] employed the activation technique, whereby a $^{17}\mathrm{O}$ target was irradiated with protons and the 511 keV annihilation γ rays resulting from the β^+ decay of $^{18}\mathrm{F}$ ($t_{\frac{1}{2}} = 110$ min) were counted. A single measurement of the total cross section was performed at an energy of $E_{\mathrm{cm}} = 190$ keV, albeit with a relatively large uncertainty of about 50% (mainly statistical). This result is approximately 50% higher than the parametrisation of Fox *et al.* [33].

Figure 3.2 shows the DC parameterisations of [30], [33] and [36]. The absolute magnitude and energy dependence of the DC S-factor obtained in each of these studies are in clear disagreement.

More recently, several relatively accurate measurements of the $^{17}\mathrm{O}(p,\gamma)^{18}\mathrm{F}$

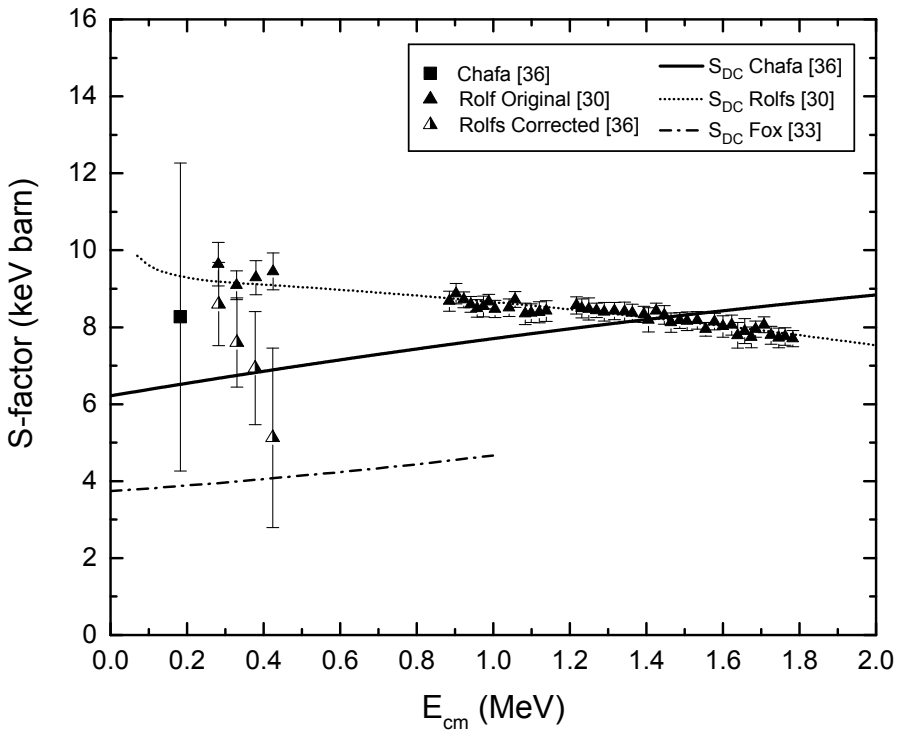

Figure 3.2: The $^{17}O(p,\gamma)^{18}F$ reaction S-factor as measured by Rolfs [30] (solid triangles) and Chafa *et al.* [36] (single solid square). The half-filled triangular symbols represent the correction to the low energy data of [30] (as proposed in [36]) due to the influence of the $E_R = 557$ and 677 keV broad resonances. The DC parameterisations of [30], [33] and [36] are also shown.

reaction cross section at energies approaching the Gamow window for classical novae have been performed at the Laboratory for Experimental Nuclear Astrophysics (LENA) in the US, by Newton *et al.* [38]. The experimental procedure followed was similar to that of [30] and [33], whereby prompt γ rays produced by a proton beam impinging on a solid, ^{17}O enriched, Ta_2O_5 target, were detected in order to infer the $^{17}O(p,\gamma)^{18}F$ reaction cross section. The S-factor results of Newton *et al.* are presented in Figure 3.3 alongside those obtained in the previous investigations described above. The constant DC contribution of (4.6 ± 0.1) keV barn extracted in the work of Newton *et al.* agrees within approximately 20% with the theoretical determination of Fox *et al.* [33], thus supporting the approach used to calculate the DC S-factor in [33].

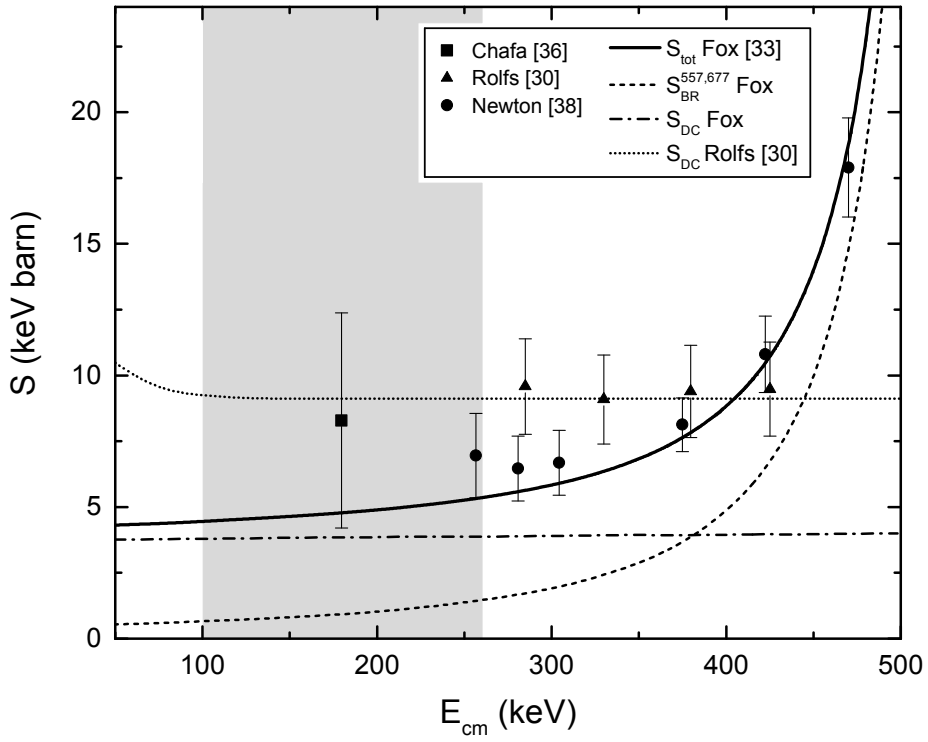

Figure 3.3: The ^{17}O(p,γ)^{18}F reaction S-factor as measured by Rolfs [30] (triangles), Chafa *et al.* [36] (single square) and Newton *et al.* [38] (circles). The grey area represents the Gamow window for classical novae. The data points from [38] are in good agreement with the total S-factor of Fox *et al.* [33] (solid line).

3.2 The E_{R} = 183 keV resonance

Thus far our discussion has concentrated on the non-resonant (DC plus broad resonance tails) contributions to the ^{17}O(p,γ)^{18}F reaction. As previously mentioned, the presence of a narrow resonance at E_{R} = 183 keV also contributes to the total reaction rate in the energy region relevant for classical novae.

Following a similar experimental approach to that of [30], this resonance was first observed by Fox *et al.* [33] using solid, ^{17}O enriched, Ta_2O_5 targets. Proton beams of up to 100 μA were produced by the 1MV JN Van de Graaff accelerator at LENA. The E_x = 5790 keV level in ^{18}F (corresponding to the E_{R} = 183 keV resonance) was observed to decay exclusively to the states at E_x = 937 and 1080 keV (see Figure 6.9), with branching ratios of 40% and 60%, respectively. The intensity of the prompt γ rays from these two primary transitions, as well as

those from the subsequent decay to the ground state of ^{18}F, were used to infer the $E_{\mathrm{R}} = 183$ keV resonance strength by means of the thick-target yield approach (Chapter 4). This analysis resulted in a resonance strength of:

$$\omega\gamma_{183}^{\mathrm{Fox}} = (1.2 \pm 0.2) \times 10^{-6}\mathrm{eV}$$

This value is approximately a factor of 2 lower than the result of a subsequent measurement performed by Chafa *et al.* [36] using the activation technique:

$$\omega\gamma_{183}^{\mathrm{Chafa}} = (2.2 \pm 0.4) \times 10^{-6}\mathrm{eV}$$

3.3 The ^{17}O$(p,\gamma)^{18}$F reaction rate

Prior to the investigation of Fox *et al.* [33], the uncertainty associated with the ^{17}O$(p,\gamma)^{18}$F reaction rate spanned several orders of magnitude [39] in the temperature range applicable to classical novae (T = 0.1-0.4 GK). This was predominantly due to the lack of information concerning the strength of the E_{R} = 183 keV resonance. Incorporating the E_{R} = 183 keV resonance strength as measured in [33] and the DC S-factor determination of [38], the recommended value for the total ^{17}O$(p,\gamma)^{18}$F reaction rate is as published in the compilation of Iliadis *et al.* [40]. Figure 3.4 illustrates the uncertainty associated with this rate, which is as high as 50% inside the Gamow window for classical novae (shaded area).

3.4 Motivation for present study

This chapter has provided an overview of the current experimental information concerning the ^{17}O$(p,\gamma)^{18}$F reaction.

In summary:

- Only a single measurement [36] of the ^{17}O$(p,\gamma)^{18}$F reaction cross section exists inside the Gamow window for classical novae (E_{cm} = 100-260 keV). The uncertainty associated with this data point is approximately 50%.

- The theoretical models used to estimate the direct capture (DC) component of the ^{17}O$(p,\gamma)^{18}$F reaction suffer from relatively large uncertainties

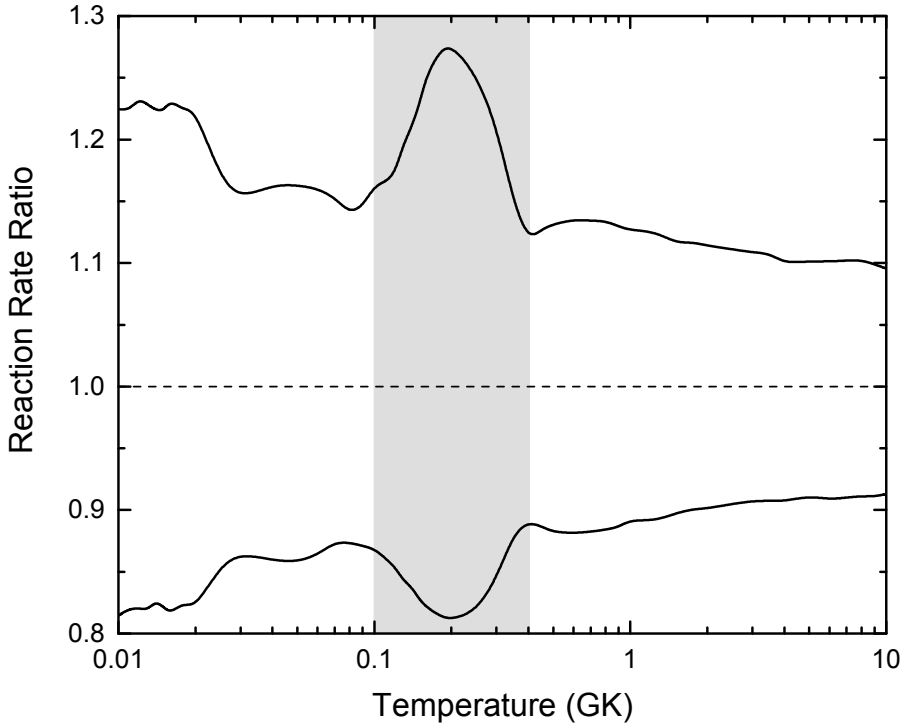

Figure 3.4: Ratio of the upper and lower $^{17}O(p,\gamma)^{18}F$ reaction rates to the recommended value as presented in [40]. The temperature range relevant for classical novae (T = 0.1-0.4 GK) is highlighted in grey.

(approximately 50% in [33] and [36]) and often rely on extrapolating data acquired at higher energy.

- There is presently a significant discrepancy (approximately a factor of 2) in the measured value of the $E_R = 183$ keV resonance strength.

These factors severely limit the accuracy to which the $^{17}O(p,\gamma)^{18}F$ reaction rate can be determined, as evident from Figure 3.4. The present study aimed at performing the first accurate measurements of the total $^{17}O(p,\gamma)^{18}F$ reaction cross section at energies between $E_{cm} = 200$-370 keV (inside the Gamow energy range for classical novae). In addition to the non-resonant component of this reaction, the strength of the $E_R = 183$ keV resonance has been measured in an attempt to solve the discrepancy between the values obtained in the previous investigations of [33] and [36].

In order to provide two independent measurements of the $^{17}O(p,\gamma)^{18}F$ reaction

cross section, the present study has been performed using both the activation and prompt γ-ray detection techniques. The work presented in this thesis relates exclusively to the prompt γ-ray analysis, which has been carried out in fulfilment of my PhD. A detailed account of the activation measurements has been published elsewhere [2].

In order to measure the extremely weak signal from the ^{17}O(p,γ)^{18}F reaction, it has been necessary to perform measurements deep underground in an environment where the background due to cosmic γ-rays is sufficiently suppressed. The location of these measurements is described in Chapter 5.

3.5 Later measurements of the ^{17}O(p,γ)^{18}F reaction

For completeness of information, I report here on the results from two further studies of the ^{17}O(p,γ)^{18}F reaction, which were published during the course of the present investigation (and following the publication of [1]).

The first of these was carried out by Hager *et al.* [41] using the DRAGON recoil separator [42] at TRIUMF, Canada. In contrast with previous investigations of the ^{17}O(p,γ)^{18}F reaction, the measurements of [41] were performed in inverse kinematics, *i.e.* using a ^{17}O beam incident on a hydrogen gas target. The total cross section was determined by measuring the yield of the recoiling ^{18}F nuclei in coincidence with the prompt γ rays from the ^{17}O(p,γ)^{18}F reaction. The measurements of Hager *et al.* were acquired at energies $E_{\rm cm}$ = 258-470 keV and are generally in good agreement with those of [38] (which cover a similar energy range).

The second study was carried out by Kontos *et al.* [43] at the Nuclear Science Laboratory of the University of Notre Dame, US. This work involved measuring the cross section for the ^{17}O(p,γ)^{18}F reaction over an energy range $E_{\rm cm}$ = 345-1700 keV and performing an R-matrix analysis[3] in order to aid the extrapolation of the S-factor down to novae energies. As with a number of previous investigations of the ^{17}O(p,γ)^{18}F reaction, solid, ^{17}O enriched, Ta_2O_5 targets were used. Proton

[3]The R-matrix formalism is a theoretical framework developed by A. M. Lane and R. G. Thomas [44] to calculate the cross section of a given nuclear reaction based on physical parameters such as the partial widths, energies and spin-parity of relevant resonances.

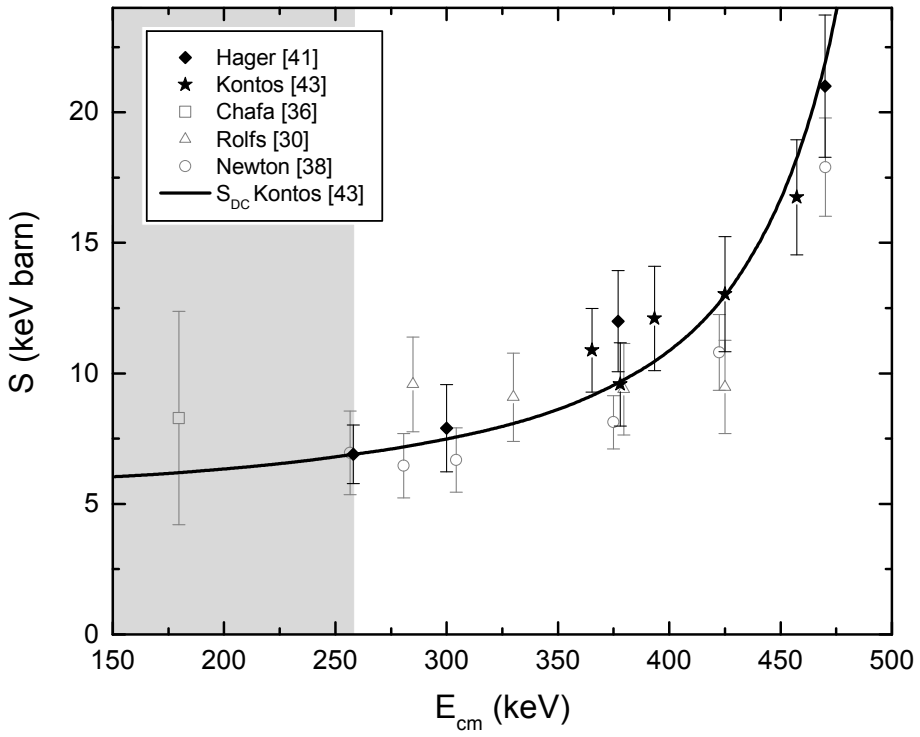

Figure 3.5: The total $^{17}O(p,\gamma)^{18}F$ reaction S-factor as determined in the work of Hager *et al.* [41] (solid diamond symbols) and Kontos *et al.* [43] (solid star symbols). Measurements performed prior to the studies of [41] and [43] are shown by open symbols. The total S-factor fit (solid line) resulting from the R-matrix analysis of [43] is also shown. There exists no accurate experimental data inside novae energy region (shaded area).

beams were provided by 1 MV and 4 MV Van de Graff accelerators and the prompt γ-ray yields associated with transitions to and from states in ^{18}F were measured using four HPGe detectors. For each observed primary transition, the experimental cross section at a given energy was extracted from the measured yield following an R-matrix approach (details in [43]). An R-matrix fit to the total cross section was then performed simultaneously for the $^{17}O(p,\gamma)^{18}F$ and $^{17}O(p,\alpha)^{18}F$ reactions, where experimental information concerning the latter was taken from [45]. This allowed the DC contribution to the $^{17}O(p,\gamma)^{18}F$ reaction cross section as well as the resonance strengths and widths of the six measured resonances between E_{cm} = 490-1037 keV to be determined. The total S-factor of Kontos *et al.*, when extrapolated to the energy region of astrophysical importance, is generally found to be in reasonable agreement with

the experimental results of the previous investigations discussed earlier in this chapter. Although systematically higher, the S-factor parameterisation of Kontos *et al.* is compatible with the result reported in [33] given the large uncertainties associated with each result (approximately 50% for [33] and 23% for [43]).

The measurements of Kontos *et al.* provide the most accurate determination to date of the partial widths associated with the two broad resonances at $E_{\mathrm{R}} =$ 577 and 677 keV (see Table 6.3). As we shall see, this information is essential in order to estimate the contribution from the tails of these resonances to the total cross section measured in the present study.

An overview of all experimental results available so far is presented in Figure 3.5. The S-factor values obtained in [41] and [43] are shown using solid symbols.

Chapter 4

Experimental Approach

The present study has aimed at determining the resonant and non-resonant contributions to the ^{17}O(p,γ)^{18}F reaction cross section by performing measurements using a proton beam incident on a solid ^{17}O enriched target. The prompt γ rays associated with this reaction have been analysed following the *thick-target yield* approach.

The reaction cross section (or resonance strength) involving γ ray cascades can be determined from measuring the yield associated with either the primary or secondary transitions, each being indicative of the production of the compound nucleus, here ^{18}F. The combined yield of all primary transitions is proportional to the total cross section. Similarly, the combined yield of all secondary γ rays to the ground state of ^{18}F provides a measure of the total cross section as they correspond to reactions forming ^{18}F. Detecting both primary and secondary γ rays therefore allows for two independent determinations of the reaction cross section.

In this chapter I will first discuss some general experimental considerations before describing the thick-target yield approach applied in this study.

4.1 Stopping power and energy loss

In passing through matter, charged particles lose energy primarily as a result of inelastic collisions with atomic electrons. Projectiles also lose energy through elastic scattering events with other nuclei, although this process is generally negligible at energies E>30 keV/u [46]. The rate of energy loss is referred to

as the *linear stopping power*, $\epsilon_{\mathrm{lin}}(E)$:

$$\epsilon_{lin}(E) = -\frac{dE}{dx} \tag{4.1}$$

where dE is the energy lost in penetrating a distance, dx, through a given medium.

The term stopping power more commonly refers to the *mass stopping power*, ϵ(E), which is defined in terms of the energy loss per unit areal density, ρ (typically given in units of atoms cm^{-2}):

$$\epsilon(E) = -\frac{dE}{d\rho} = -\frac{1}{N}\frac{dE}{dx} \tag{4.2}$$

where N is the number density (atoms per cm^3) of the target material.

Although a comprehensive theoretical treatment of the interaction of charge particles in matter is prohibitively complex, the Bethe formula [46] provides fairly accurate predictions of the electronic component of the stopping power for high energy projectiles (E>0.6 MeV/u):

$$-\frac{dE}{dx} = \frac{4\pi e^4 z^2}{m_{\mathrm{e}} v^2} NB \tag{4.3}$$

where

$$B \equiv Z\left[ln\left(\frac{2m_{\mathrm{e}}v^2}{I}\right) - ln\left(1 - \frac{v^2}{c^2}\right) - \frac{v^2}{c^2}\right]$$

These equations describe the theoretical stopping power for a projectile of charge, z, and velocity, v, passing though a medium composed of atoms of atomic number, Z. The ionisation potential is represented by the empirically determined parameter, I, and m_{e} is the rest mass of an electron (m_{e} = 511.0 keV/c^2). In Equation 4.3, the factor, B, varies smoothly as a function of energy. This means that the stopping power is approximately inversely proportional to energy (since $E \propto v^2$), reflecting the fact that charged particles lose relatively more energy the longer they spend in the vicinity of electrons. As a consequence of the charge dependence of the Coulomb potential (Equation 2.9), the stopping power is also proportional to the charge, z, of the incident projectile.

For projectile energies lower than approximately E<30 keV/u the nuclear component of the stopping power must also be considered. In this energy regime,

charge particles no longer possess sufficient energy to lead to significant ionisation of the target atoms, and may lose charge through the acquisition of electrons. This means that Equation 4.3 no longer accurately models the stopping power, which must often be determined from the results of experimental measurements.

Thus far we have limited our discussion to the stopping power for targets composed of purely one element. In practice, nuclear physics experiments often involve using solid targets where the nuclei of interest for the particular reaction under investigation form part of a chemical compound. In this case a quantity known as the *effective stopping power*, ϵ_{eff}, must be calculated:

$$\epsilon_{\text{eff}} = \epsilon_a + \sum_i \frac{N_i}{N_a}\epsilon_i \tag{4.4}$$

where the relevant target nuclei, N_a, are referred to as *active* nuclei and N_i are the additional *inactive* nuclei which do not participate in the reaction.

For the Ta_2O_5 targets used in this study (Chapter 6), the effective stopping power is given by:

$$\epsilon_{\text{eff}}(^{17}\text{O}) = \left(\epsilon(^{17}\text{O}) + \frac{\text{N}(^{16}\text{O})}{\text{N}(^{17}\text{O})}\epsilon(^{16}\text{O}) + \frac{\text{N}(^{18}\text{O})}{\text{N}(^{17}\text{O})}\epsilon(^{18}\text{O}) + \frac{\text{N(Ta)}}{\text{N}(^{17}\text{O})}\epsilon(\text{Ta})\right) \tag{4.5}$$

Since the stopping powers of different isotopes of oxygen are approximately equal, this expression can be simplified as:

$$\epsilon_{\text{eff}}(^{17}\text{O}) = \left(\frac{\text{N(O)}}{\text{N}(^{17}\text{O})}\epsilon(\text{O}) + \frac{\text{N(Ta)}}{\text{N}(^{17}\text{O})}\epsilon(\text{Ta})\right) \tag{4.6}$$

The effective stopping power for protons incident on a Ta_2O_5 target, 66% enriched in ^{17}O (active nuclei), is shown in Figure 4.1 as a function of proton energy.

Projectiles follow a range of unique trajectories due to statistical variations in the number of collisions within a target medium. This effect is referred to as straggling and leads to a distribution in the velocities of projectiles after passing through a given target material, as illustrated in Figure 4.2. Figure 4.3 shows the degree to which straggling affects a beam of mono-energetic protons with initial energy, $E_0 = 300$ keV, passing through a 0.2 μm (typical of the targets used in this study) layer of Ta_2O_5.

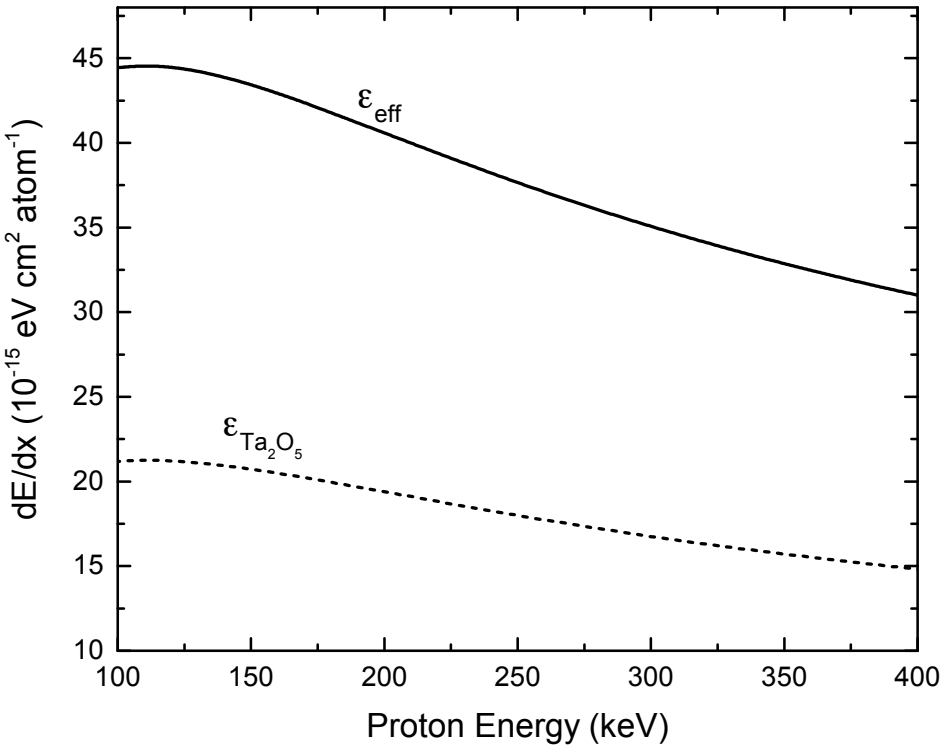

Figure 4.1: The *effective* stopping power (solid line) for protons incident on a Ta_2O_5 target, 66% enriched in ^{17}O (active nuclei). The *absolute* stopping power of Ta_2O_5 is also shown (dashed line) as calculated using SRIM [47].

The computer code SRIM [47] was used to provide the stopping power information required for the analysis of the present measurements of the $^{17}O(p,\gamma)^{18}F$ reaction. These calculations are based on experimental measurements as well as the theoretical predictions of Equation 4.3.

4.2 Yields and cross sections for charged-particle-induced reactions

In order to experimentally determine the absolute cross section of a given nuclear reaction, one or more of the reaction products must be detected and identified. In the case of the present study this involved measuring the intensity of prompt γ rays from the $^{17}O(p,\gamma)^{18}F$ reaction.

The *reaction yield* is defined as the ratio of the total number of reactions, N_R, to the total number of incident beam particles, N_b. The measured yield

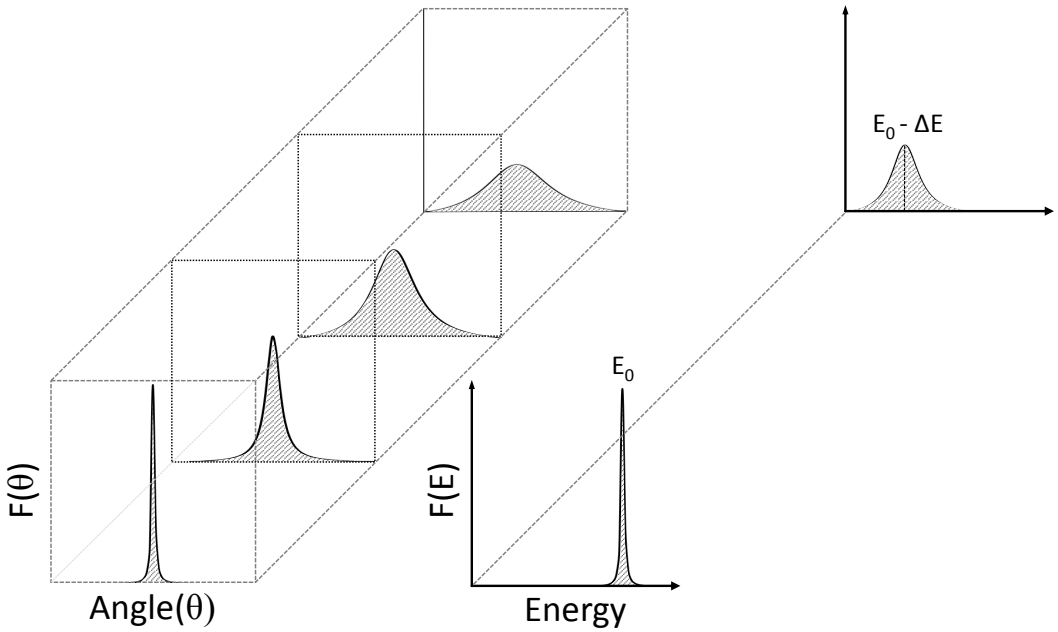

Figure 4.2: An illustration showing the effects of beam straggling. The incident beam is originally collimated and approximately mono-energetic. As the beam penetrates the target medium, the velocity distribution of the projectiles diverges due to statistical fluctuations in the number of collisions. This is indicated by the broadening of the probability distributions associated with the scattering angles, F(θ), and energies, F(E).

depends not only on the reaction cross section, σ, but also on the number of target nuclei available for interactions and hence on the target thickness. For a target sufficiently thin that the beam energy, E_0, and reaction cross section can be treated as constant, the yield is given by:

$$Y = \frac{N_{\mathrm{R}}}{N_b} = \sigma(E_0) N_t \Delta x \tag{4.7}$$

where N_{t} is the number of target nuclei per unit volume and Δx is the (linear) target thickness.

The energy lost by the beam in passing through the target is generally non-negligible (see Section 4.1) and the energy dependence of the cross section must be taken into account. The total reaction yield is then expressed as an integral over the thickness of the target:

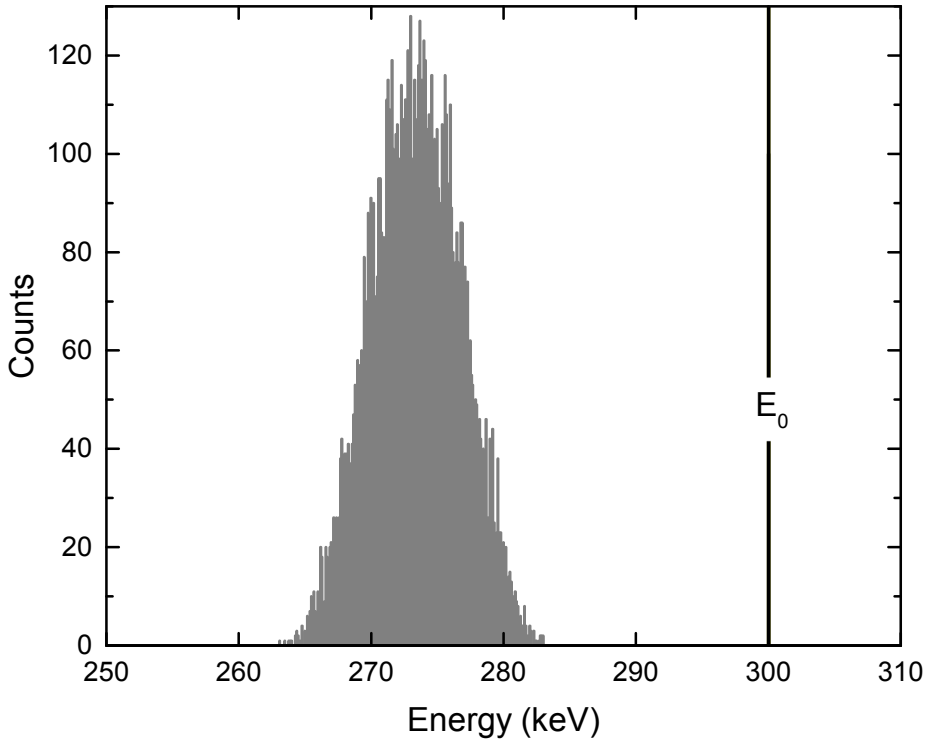

Figure 4.3: The distribution of proton energies after passing through a 0.2 μm layer of Ta_2O_5 for an initially mono-energetic beam of protons with energy, E_0 = 300 keV (Spectrum simulated for 10000 projectiles using SRIM [47]).

$$Y = \int \sigma(x) N_t(x) dx = \int_{E_0 - \Delta E}^{E_0} \frac{\sigma(E)}{\epsilon(E)} dE \tag{4.8}$$

where $\epsilon(E)$ is the stopping power (Section 4.1) and describes the extent to which incident particles lose energy as a result of interactions inside the target[1]. For light ions such as protons, the stopping power is often weakly dependent on energy and approximately constant over the target thickness.

4.2.1 Non-resonant reactions

For non-resonant reactions the cross section typically changes little over the target thickness. Equation 4.8 can thus be written as:

[1]If the target consists of a compound containing inert particles, *i.e.* nuclei other than the species relevant to the reaction under investigation, the effective stopping power must be determined as discussed in Section 4.1.

$$Y = \frac{S(E_{\text{eff}})}{\epsilon(E_0)} \int_{E_0-\Delta E}^{E_0} \frac{1}{E} e^{-2\pi\eta(E)} dE \tag{4.9}$$

The measured yield is an average value resulting from reactions occurring at a range of energies (E_0 to E_0-ΔE) throughout the target. The S-factor determined from Equation 4.9 should therefore be associated with an *effective energy*, E_{eff}, that is equivalent to the energy at which 50% of the total yield is obtained (Figure 4.4). Provided the cross section remains approximately constant over the target thickness, the effective energy is simply given by energy mid-way through the target ($E_{\text{eff}} = E_0$ - $\Delta E/2$). Often this is not the case and a more accurate value of the mean effective energy can be calculated using the expression [48]:

$$E_{\text{eff}} = \frac{\int_{E_0-\Delta E}^{E_0} E\sigma(E)dE}{\int_{E_0-\Delta E}^{E_0} \sigma(E)dE} \tag{4.10}$$

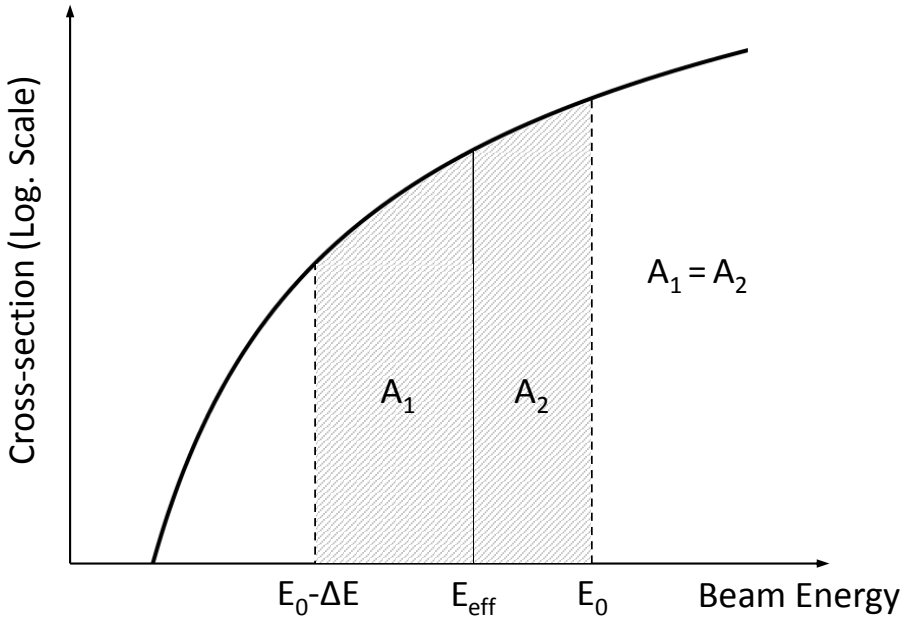

Figure 4.4: The effective interaction energy, E_{eff}, is equivalent to the energy at which 50% of the total yield is obtained. As the yield is directly proportional to the integral of the reaction cross section (Equation 4.8), E_{eff} corresponds to the energy bisecting the two equal areas labeled A_1 and A_2.

4.2.2 Resonant reactions

For resonant reactions proceeding through the formation of an isolated, narrow, resonance, the cross section is described by the Breit-Wigner formalism presented in Chapter 2. Combining Equations 2.20 and 4.8 allows the measured yield from such a resonance to be expressed in terms of the resonance strength, $\omega\gamma$, target thickness, ΔE, and initial beam energy, E_0, as:

$$\begin{aligned} Y(E_0) &= \int_{E_0-\Delta E}^{E_0} \frac{1}{\epsilon(E)} \frac{\lambda_R^2}{4\pi} \omega \frac{\Gamma_a \Gamma_b}{(E_{\mathrm{R}} - E)^2 + \Gamma^2/4} dE \\ &= \frac{\lambda_{\mathrm{R}}^2}{2\pi} \frac{\omega\gamma}{\epsilon_{\mathrm{R}}} \frac{\Gamma}{2} \int_{E_0-\Delta E}^{E_0} \frac{1}{(E_{\mathrm{R}} - E)^2 + (\Gamma^2/2)^2} dE \\ &= \frac{\lambda_{\mathrm{R}}^2}{2\pi} \frac{\omega\gamma}{\epsilon_{\mathrm{R}}} \frac{\Gamma}{2} \left[\arctan\left(\frac{E_0 - E_{\mathrm{R}}}{\Gamma/2} \right) - \arctan\left(\frac{E_0 - E_{\mathrm{R}} - \Delta E}{\Gamma/2} \right) \right] \end{aligned} \tag{4.11}$$

where the de Broglie wavelength, λ_{R}, and stopping power, ϵ_{R}, are evaluated at the effective energy, which for a narrow resonance is equivalent to the resonance energy, E_{R}. It is important to point out that Equation 4.11 is defined for a mono-energetic beam and does not account for energy straggling effects inside the target medium.

As mentioned in the previous section, the measured yield is directly proportional to the integral of the cross section over the energy range, ΔE. In the case of a resonance, the cross section is characterised by a symmetric peak of finite width, Γ_{R} (Chapter 2). Depending on the target thickness and initial beam energy only a portion of the total resonant cross section may contribute to the observed yield. For a target sufficiently thick to fully stop the incoming beam (*i.e.* an 'infinitely thick' target), incrementally increasing the beam energy (from a point, E_0, below the resonance), leads to the resonant yield curve (described by Equation 4.11) shown in Figure 4.5. The patterned regions indicate the fraction of the resonant cross section which contributes to the measured yield for the first two points highlighted in the upper plot of Figure 4.5. For the higher energy point (measured at a beam energy of $E_0^{''}$>E_0) the full width of the resonance is covered by the target, and the corresponding yield therefore reaches it maximum value. It can be shown from Equation 4.11 that the maximum yield is given by:

$$Y_{\max} = \frac{\lambda_{\mathrm{R}}^2}{\pi}\frac{\omega\gamma}{\epsilon_{\mathrm{R}}}\frac{\Gamma}{2}\arctan\left(\frac{\Delta E}{\Gamma_R}\right) \tag{4.12}$$

which, in the limit of an infinitely thick target, becomes:

$$Y_{\max} = \frac{\lambda_{\mathrm{R}}^2}{2\epsilon_{\mathrm{R}}}\omega\gamma \tag{4.13}$$

Equation 4.13, generally valid if $\Delta E \gg \Gamma_{\mathrm{R}}$, can be used to determine the resonance strength, $\omega\gamma$, directly from the experimentally measured yield.

The resonance energy, E_{R}, corresponds to the mid-point (half-maximum) of the rising edge of the yield curve shown in Figure 4.5, while the resonance width, Γ_{R}, is equal to the difference between the energies at which 25% and 75% of the maximum yield, $Y_{\max}$, are obtained.

Figure 4.6 presents a similar diagram to Figure 4.5, for measurements performed using a target of finite thickness, ΔE. In this case, the yield curve displays a rising edge (as evident in Figure 4.5) and a falling tail (paramaterised by the second 'arctangent' term in Equation 4.11). The target thickness, ΔE, is related to the full-width at half-maximum (FWHM) of the yield curve, and resonance width, Γ_{R}, as:

$$\mathrm{FWHM} = \sqrt{\Gamma_{\mathrm{R}}^2 + \Delta E^2} \approx \Delta E \quad (\text{for } \Delta E \gg \Gamma_{\mathrm{R}}) \tag{4.14}$$

This equation provides a useful relationship for determining the thickness of a target directly from the measured yield curve.

Energy straggling has the effect of broadening the high energy tail of a resonance profile scan. This effect is clearly visible in the resonance profile scans presented in Chapter 6.

4.3 Gamma-ray peak shape for primary transitions

While the energy of the γ rays resulting from a secondary transition conform to a Gaussian distribution, the γ-ray peak shape associated with a primary transition is modulated by the energy dependence of the cross section as the beam loses energy passing through the target and must be taken into account in the analysis

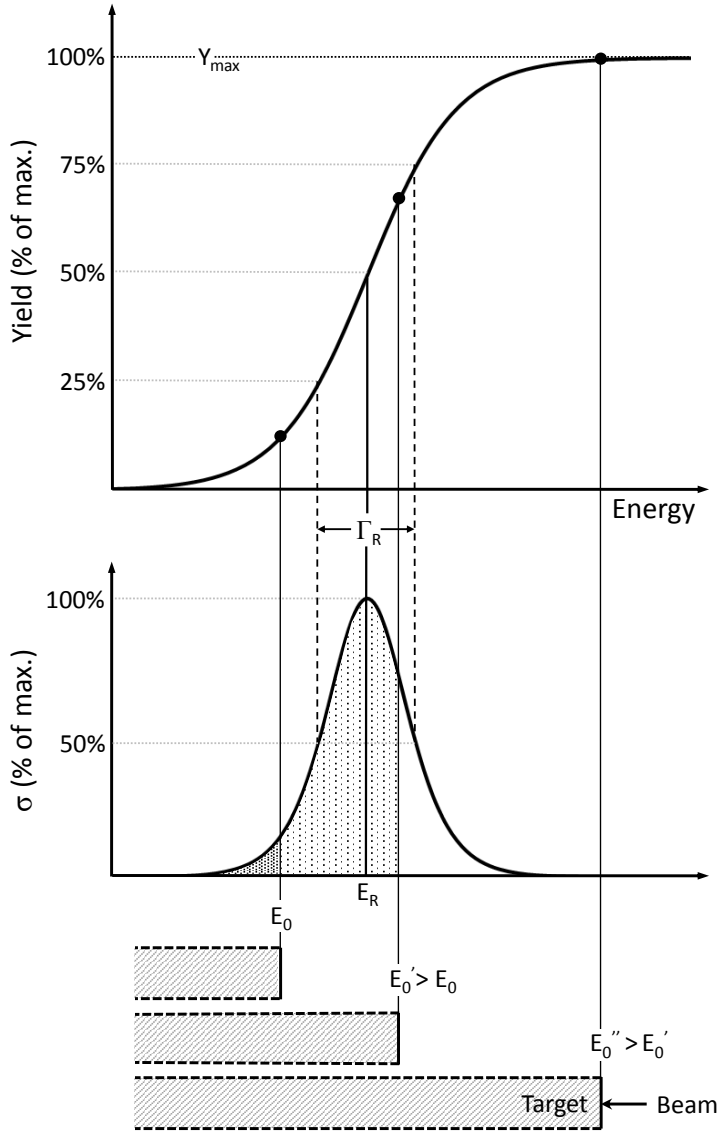

Figure 4.5: Measured yield (upper plot) as a function of beam energy for a resonance measured using an infinitely thick target. The shape of the resonance cross section is given in the lower plot for a resonance of energy E_{R} and width Γ_{R}. The shaded areas correspond to the fraction of the total cross section covered by the target at beam energies of E_0 and $E_0^{'}{>}E_0$. The corresponding yields are shown as solid points on the yield curve. The maximum yield, Y_{max}, is obtained at beam energies of $E{\geq}E_0^{''}$ and includes contributions from the entire resonant cross section.

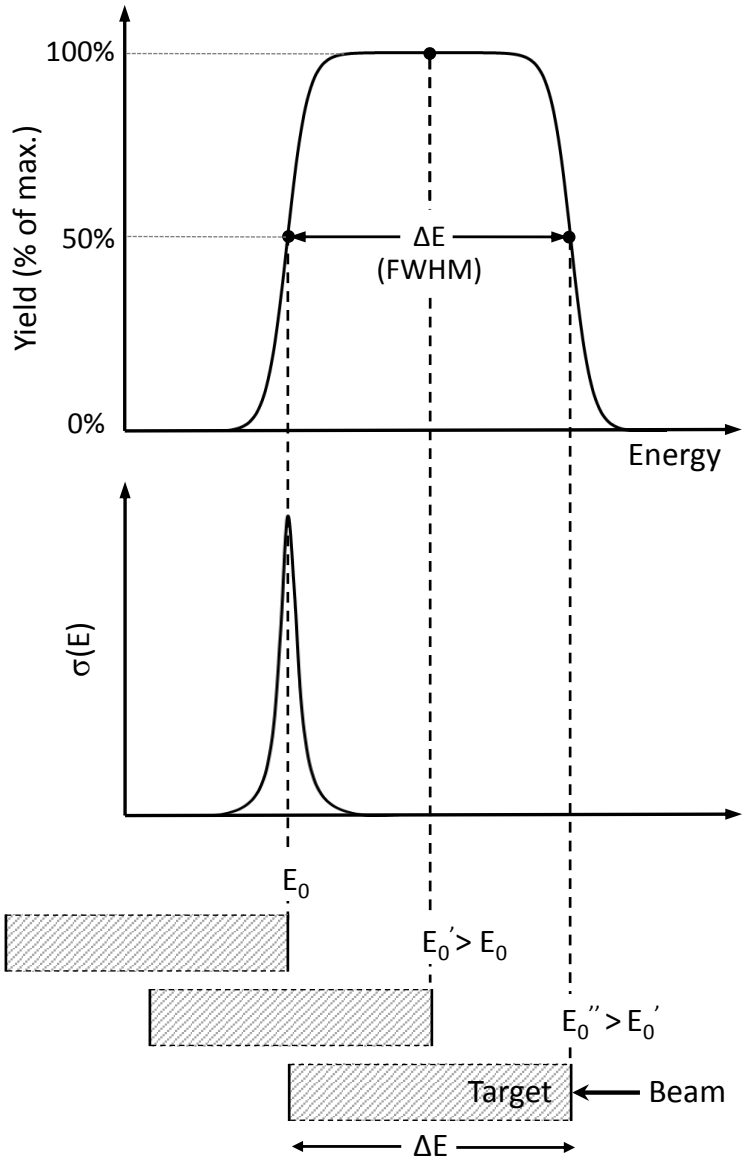

Figure 4.6: Measured yield (upper plot) as a function of beam energy for a resonance measured using a target of finite thickness. The resonant cross section is shown in the lower panel. The yields measured at three different beam energies are indicated as solid points. The target thickness, ΔE, (at beam energy E_0'') is approximately equal to the full-width at half-maxiumum (FWHM) of the yield curve, provided that $\Delta E \gg \Gamma_{\mathrm{R}}$.

of primary transitions. Figure 4.7 illustrates the peak shape associated with a (non-resonant) primary γ-ray transition.

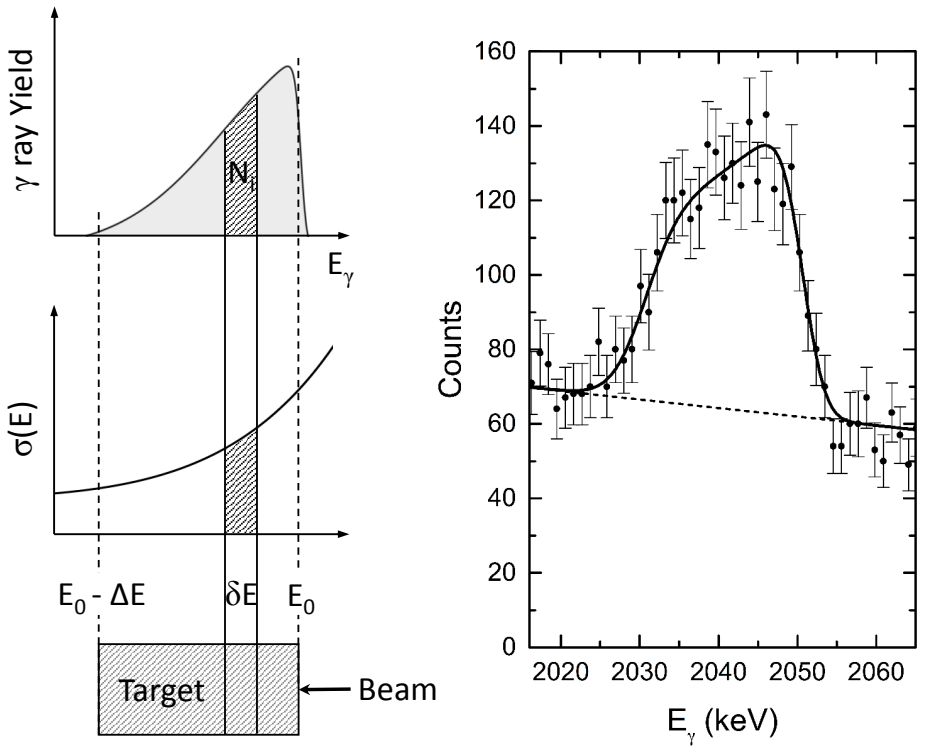

Figure 4.7: Left: The characteristic γ-ray peak shape resulting from a primary transition reflects the energy dependence of the cross section as the beam loses energy inside the target. The number of counts, N_i, corresponding to a thin slice of the target of width, δE, is proportional to the integral of the cross section. Right: Example of a primary γ-ray transition (R/DC$\rightarrow$3839 keV) from the present study of the ^{17}O$(p,\gamma)^{18}$F reaction.

The number of γ rays associated with reactions occurring inside a thin slice, i, of width δE of the target (Figure 4.7) is obtained by differentiating Equation 4.8:

$$N_i = N_p \frac{\sigma_i(E)}{\epsilon_i(E)} \delta E \tag{4.15}$$

where $N_{\rm p}$ is the number of protons incident on the target.

This expression must be modified in order to account for experimental effects such as the detector efficiency:

$$N_i = N_p \frac{\sigma_i(E)\eta(E_{\gamma,i})P_i(E)}{\epsilon_i(E)}\delta E \tag{4.16}$$

where $\eta(E_{\gamma,i})$ is the photo-peak efficiency (Appendix A). The function $P_{\rm i}(E)$ is introduced to model the shape of the target profile and ensure that $N_{\rm i}$ falls to zero outside its limits *i.e.* outside the energy range spanned by the target. Equation 4.16 allows the S-factor to be obtained directly from fitting the observed γ-ray peak shape[2], as described in Chapter 6.

The energy of a DC γ ray is related to the interaction energy, $E_{\rm cm}$, (at a given point inside the target) by the expression:

$$E_\gamma = E_{\rm cm} + Q - E_x - \Delta E_{\rm Rec} + \Delta E_{\rm Dop} \tag{4.17}$$

where Q is the reaction Q-value (Q= 5606.5 keV for the ^{17}O(p,γ)^{18}F reaction [49]) and E_x is the energy of the level populated in the resultant nucleus (^{18}F). The recoil energy of the nucleus of mass M is given by: $\Delta E_{\rm Rec}$=$\frac{E_\gamma^2}{2Mc^2}$, while $\Delta E_{\rm Dop}$ is the correction due to the Doppler effect. The Doppler energy shift of γ rays detected at an angle θ with respect to an emitting nucleus travelling at velocity, v, is given by: $\Delta E_{\rm Dop} = \frac{v}{c}E_\gamma \cos(\theta)$.

4.4 True coincidence summing effects

Any study that infers the cross section of a reaction from the detection of γ rays associated with a decay cascade must account for the possibility of detecting one or more of these γ rays in coincidence. If this occurs within a timescale shorter than the resolving time of the detector, then an event with energy equal to the sum of the individual γ rays will be recorded. This effect is referred to as *true coincidence summing* (TCS) and becomes particularly prevalent when the solid angle subtended by the detector is large.

The importance of correcting for TCS effects is clearly illustrated by considering a simple γ-ray decay scheme such as the one shown in Figure 4.8. In this example the state labelled as S_1 can either decay directly to the ground state with the emission of the γ ray labelled γ_0, or decay through an intermediate

[2]The resolution of the detector also influences the observed peak shape associated with a primary γ-ray transition. This effect is discussed in Chapter 6.

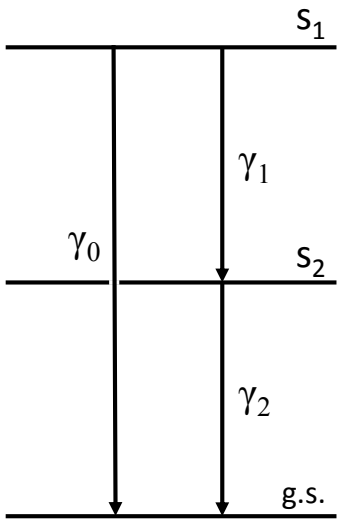

Figure 4.8: A schematic energy level diagram showing a simple γ-ray decay scheme. The state S_1 may decay to the ground state either directly or via the intermediate state, S_2. In the presence of true coincidence summing effects, the γ-ray yield associated with γ_1 and γ_2 will be lower than the 'true' yield (due to summing-out) while the yield corresponding to γ_0 will be artificially higher as a result of summing-in. See text for further details.

state (S_2) with the emission of two successive γ rays, γ_1 and γ_2. If the efficiency for detecting each of these γ rays is sufficiently high, they will often be detected in coincidence. This means that the measured yield of γ_1 and γ_2 will be lower than the 'true' yield since some of these γ rays will instead appear as counts with an energy identical to that of γ_0. Consequently, the yield associated with the ground state transition, γ_0, will be higher than the 'true' yield expected in the absence of TCS effects. The apparent loss and gain of counts for these three transitions is referred to a summing-out and summing-in, respectively.

It is possible to estimate the magnitude of these summing effects given the branching ratios of the relevant states involved in the decay cascade. For the example presented in Figure 4.8, the summing-corrected yields, $N_{i_{pri}}$, $N_{i_{sec}}$ and $N_{i_{gs}}$ for each of the three transitions, γ_1, γ_2 and γ_0, can be written in terms of the branching ratios and detection efficiency as:

$$N_{\mathrm{gs}} = Y\left(b_{\mathrm{gs}}\eta_{\mathrm{fe}}(E_{\mathrm{gs}}) + \sum_i b_i\eta_{\mathrm{fe}}(E_{i_{\mathrm{sec}}})\eta_{\mathrm{fe}}(E_{i_{\mathrm{pri}}})\right) \tag{4.18}$$

$$\begin{aligned} N_{i_{\mathrm{pri}}} &= Y b_i\eta_{\mathrm{fe}}(E_{i_{\mathrm{pri}}})(1-\eta_{\mathrm{tot}}(E_{i_{\mathrm{sec}}})) \\ N_{i_{\mathrm{sec}}} &= Y b_i\eta_{\mathrm{fe}}(E_{i_{\mathrm{sec}}})(1-\eta_{\mathrm{tot}}(E_{i_{\mathrm{pri}}})) \end{aligned} \tag{4.19}$$

where Y is the total number of reactions, b_i is the branching ratio of the i-th transitions. The full-energy peak efficiency, η_{fe}, and total efficiency, η_{tot}, appearing in these equations are discussed in Appendix A. It should be noted that equations 4.18 and 4.19 only hold for isotropic angular distributions and in the absence of any angular correlation between γ rays.

Chapter 5

Experimental Setup

Directly measuring the cross sections of charged-particle induced reactions at astrophysically relevant energies is often extremely challenging as a result of the exponential drop in the cross section at energies below the Coulomb barrier. In performing such measurements (that often involve cross sections in the range of pico to femto barn or lower) background radiation from cosmic rays becomes increasingly problematic. Here I provide a brief account of the origin and implications of this cosmic γ-ray background before describing the LUNA underground facility where the present prompt γ-ray measurements of the ^{17}O(p,γ)^{18}F reaction cross section have been performed. The experimental apparatus used for the activation study is also briefly discussed.

5.1 Cosmic background considerations

The Earth is continually bombarded by charged particles - predominantly high energy protons (92%) and alpha particles (7%) - of cosmic origin[1]. These so-called *cosmic rays* interact with nuclei in the upper atmosphere (via the strong nuclear force) producing mainly pions (π), which subsequently decay to muons (μ) and muon neutrinos (ν_μ) via weak nuclear interactions:

[1]Cosmic rays are detected over a wide energy range between 10^2-10^{13} MeV and are believed to originate mainly from supernovae events [50].

$$\begin{aligned} \pi^+ &\rightarrow \mu^+ + \nu_\mu \\ \pi^- &\rightarrow \mu^- + \bar{\nu_\mu} \end{aligned} \tag{5.1}$$

The neutral pion, π^0, decays electromagnetically into two γ rays.

Muons are unstable particles, decaying on the time-scale of μs to produce electrons and positrons:

$$\begin{aligned} \mu^+ &\rightarrow e^+ + \nu_e + \bar{\nu_\mu} \\ \mu^- &\rightarrow e^- + \bar{\nu_e} + \nu_\mu \end{aligned} \tag{5.2}$$

The muons and electrons produced in the processes described by Equations 5.1 and 5.2 are referred to as *secondary* cosmic rays. Muons are the most penetrating component of this secondary radiation and account for approximately 70% of the particles reaching the Earth's surface (the remaining 30% consists mainly of electrons). Figure 5.1 illustrates some of the processes described above.

On entering a dense medium (such as a detector) high energy (typically 10^0 - 10^3 MeV) muons emit Bremsstrahlung radiation[2] in the form of X rays and γ rays. In the energy region above approximately $E_\gamma = 3$ MeV, a typical γ-ray spectrum will be dominated by these cosmic γ-ray events, masking any low intensity signal. One way to significantly reduce the effects of cosmic rays is to perform experiments deep underground where the muon flux is heavily attenuated by the overlying rock. This possibility is realised at the Laboratori Nazionali del Gran Sasso (LNGS), Italy, where the present measurements have been performed using the Laboratory for Underground Nuclear Astrophysics (LUNA) accelerator facility [52].

[2]In addition to energy loss due to electron excitation and ionisation, and elastic collisions with target nuclei (Chapter 4), there is one further process by which extremely high energy (E>10 MeV) ions can lose energy. This involves the emission of electromagnetic radiation (referred to *Bremsstrahlung* radiation [51]) as a result of the deceleration of charged particles in the presence of an electromagnetic field.

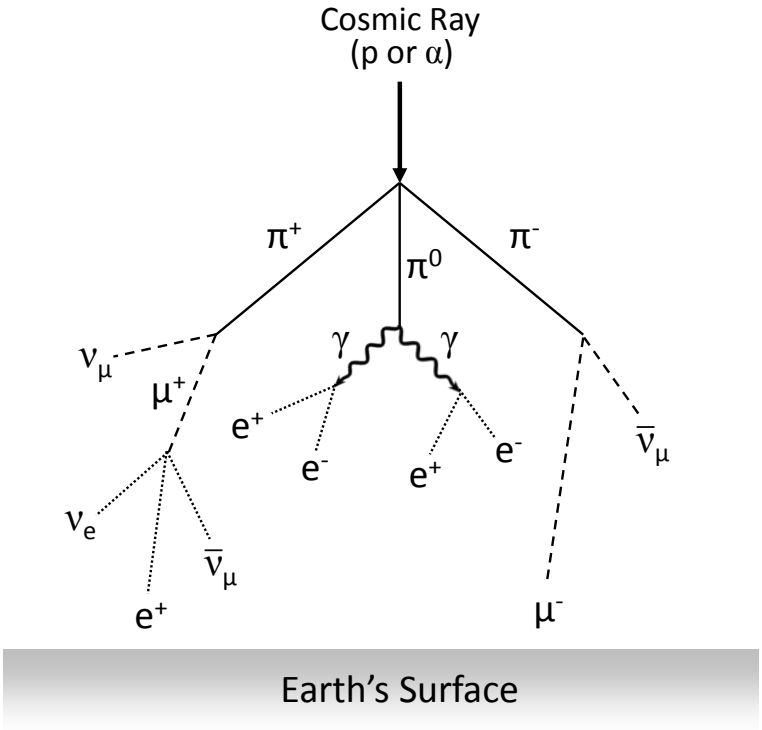

Figure 5.1: Cosmic rays (mainly protons and alpha particles) may interact with atoms in the upper atmosphere to produce pions, which ultimately decay into muons and electrons. Many of these particles reach the Earth's surface leading to the production of γ rays via the Bremsstrahlung process.

5.2 The underground LUNA facility

Owing to the unique location of the LNGS facility underneath the central Appenine mountain range, the cosmic muon flux is reduced by a factor of approximately 10^6 compared with that measured at the Earth's surface [53]. This translates into a cosmic γ-ray flux in the region E_γ = 3-8 MeV approximately 2500 times lower than can be achieved above ground [54]. For this reason, the LUNA accelerator facility served as an ideal location to undertake the present low-energy investigation of the ^{17}O(p,γ)^{18}F reaction. The location of the LUNA accelerator facility inside the LNGS laboratory is shown in Figure 5.2. A comparison between γ-ray spectra acquired using a high purity germanium (HPGe) detector (125% relative[3] efficiency) positioned above ground (grey spectrum) and at the LUNA

[3]Relative to a standard 3×3 inch NaI crystal.

underground facility (black spectrum) is presented in the upper panel of Figure 5.3. Above $E_\gamma = 3$ MeV, the cosmic-ray background is reduced to almost zero in the measurement performed underground. Importantly, this is the energy region in which many of the primary transitions from the $^{17}O(p,\gamma)^{18}F$ reaction are expected. For energies below approximately $E_\gamma = 3$ MeV, the background is largely dominated by environmental radioactivity. Some of the most intense sources originate from the radionuclides associated with the decay chains of ^{238}U and ^{232}Th, while the strong line located at $E_\gamma = 1460$ keV is associated with the decay of ^{40}K. This component of background radiation can be significantly reduced using a lead shield, as shown in the lower panel of Figure 5.3.

5.3 Experimental Apparatus

All charged particle accelerators operate utilising the same fundamental principle: the acceleration of ions in the presence of strong electric and/or magnetic fields. Electrostatic accelerators are most commonly used for nuclear astrophysics applications, where beam energies of hundreds of keV to tens of MeV are typically required. The 400kV accelerator installed at LUNA (see Figure 5.4), which is manufactured by High Voltage Engineering [57], is of the Cockcroft-Walton design [58] and is capable of producing proton beams in the energy range 50-400 keV with a maximum current (on-target) of approximately 300 μA. In order to avoid sparks between the various high voltage components, the accelerator is enclosed inside a tank containing an insulating mixture of N_2 and CO_2 at a pressure of 20 bar. Hydrogen (or helium) gas is ionised using a radio frequency (RF) oscillator in order to produce a source of plasma confined by an axial magnetic field. Once extracted from the source and accelerated, the proton beam is guided and focused to the target station using a 45° dipole magnet and a vertical steerer. Insertable Faraday cups positioned before and after the 45° magnet allow monitoring of the beam current, which is essential in order to optimise the beam focussing. Several static collimators are also positioned at various points along the beam-line, ensuring that only the target surface is illuminated by the beam. Immediately prior to entering the target chamber the beam passes through a liquid nitrogen (LN_2) cooled copper tube that serves to

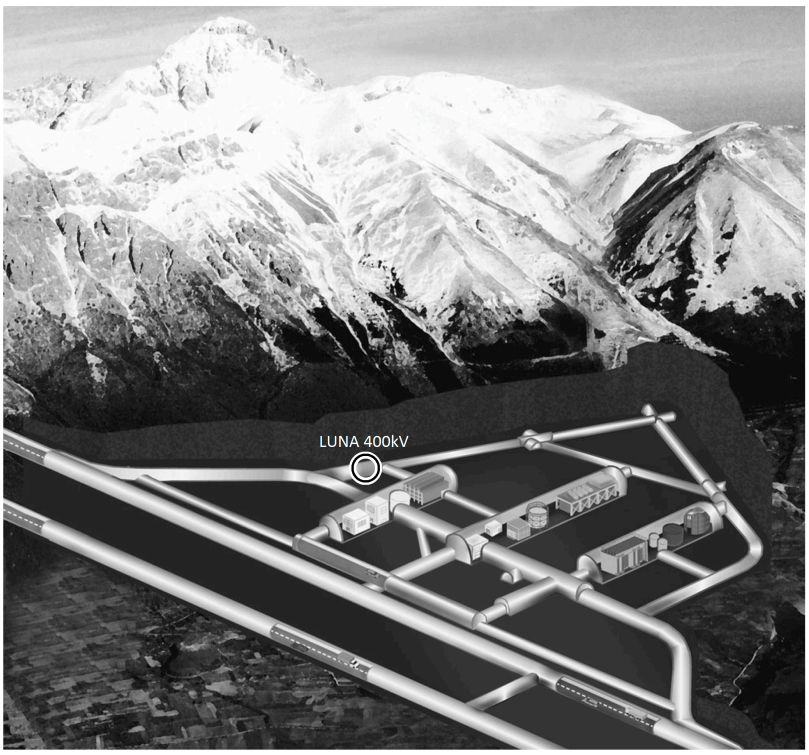

Figure 5.2: The Laboratori Nazionali del Gran Sasso (LNGS) is located underneath the Appenine mountain range in central Italy. Approximately 1400 m of overlying rock strongly attenuates the cosmic-ray flux, leading to an extremely low-level background environment (see text). The LUNA 400kV accelerator facility occupies a relatively small area off one of the passageways, as indicated. Access to the LNGS facility is gained directly from the public highway, which runs through a 10 km long tunnel inside the mountain. Image courtesy of [55].

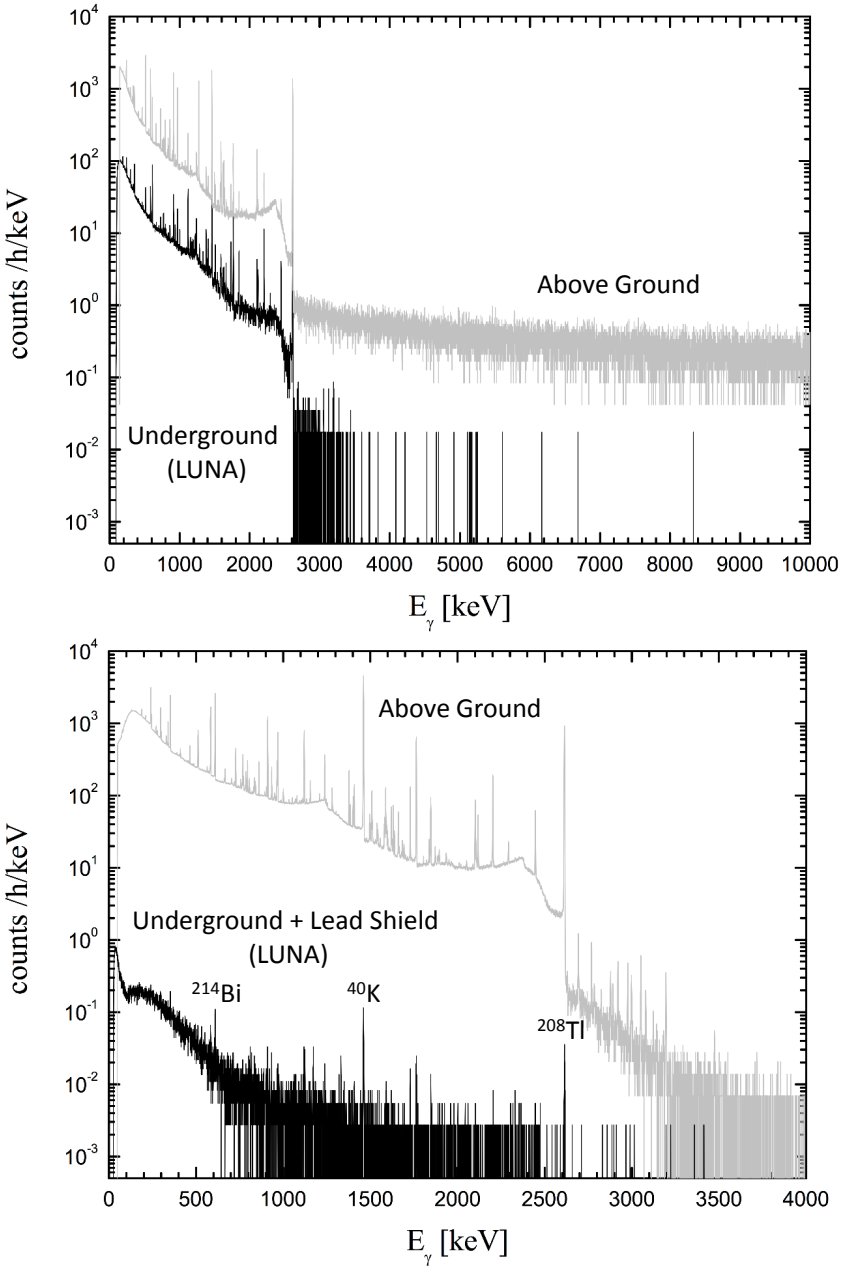

Figure 5.3: Upper panel: γ-ray spectra acquired using a high purity germanium (HPGe) detector positioned above ground (grey) and at the LUNA underground facility (black). Lower panel: The γ-ray spectrum (below $E_\gamma = 4$ MeV) acquired with a thick (approximately 15 cm) lead shield surrounding the LUNA detector. The spectrum shown in grey is acquired above ground with no additional lead shielding [56].

reduce beam-line contaminants[4] and prevents the build-up of carbon on the target surface. A bias voltage of -300 V was applied to the copper tube to suppress secondary electrons emitted when protons strike the target.

The layout of the LUNA accelerator facility in addition to the up-stream portion of the beam-line is shown in Figure 5.6, whereas a detailed diagram of the target chamber is presented in Figure 5.7.

The Ta_2O_5 targets (Section 5.4) used in this investigation were mounted on a flange positioned at 55° with respect to the beam axis. De-ionised water was circulated in order to cool the targets and avoid any damage due to beam-heating effects. A turbo pump installed below the copper tube maintained a pressure of approximately 5×10^{-7} mbar inside the target chamber. The target flange was isolated from all other beam-line components and acted as a Faraday cup allowing the total charge accumulated over the course of a measurement to be determined.

An Ortec [59] high purity Germanium (HPGe) detector of relative efficiency 120% was positioned at 55° relative to the beam axis, at a distance of approximately 1.5 cm from the target surface. The 55° alignment was chosen in order to mitigate any angular distribution effects (as explained in Chapter 6). The detector and attached LN_2 dewar (not shown is Figure 5.6) were mounted on rails to provide access to the target chamber. Additional information relating to HPGe detectors in general can be found in Appendix A. In order to reduce the level of natural and cosmic-ray induced background, the entire target chamber and detector assembly was surrounded by a lead castle approximately 5 cm thick (it was not possible to construct a thicker shield due to space constraints). The shielding led to a further factor of 10 reduction in the level of background below E_γ = 3 MeV. Standard electronics were used for processing the detector signal, which was stored in a 16k-channel analogue-to-digital converter (ADC). The processed digitised data were sent via ethernet cable to a PC running GammaVision analysis software [59] for online analysis of the acquired spectra.

5.4 Tantalum oxide targets preparation

As in a number of previous investigations of the $^{17}O(p,\gamma)^{18}F$ reaction (Chapter 3), the present study was carried out using Ta_2O_5 targets enriched in ^{17}O. A detailed

[4]Contaminant particles dispersed inside the beam-line that come into contact with the LN_2 cooled copper tube will effectively 'freeze' onto its surface, and thus be removed from suspension.

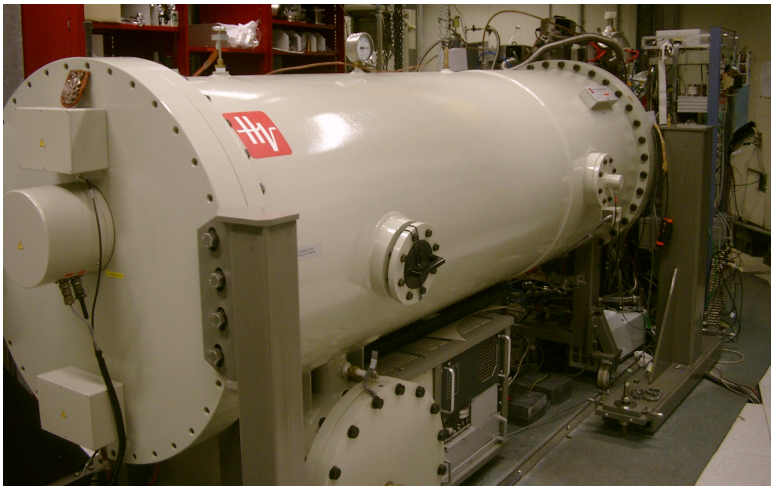

Figure 5.4: The LUNA 400kV accelerator tank.

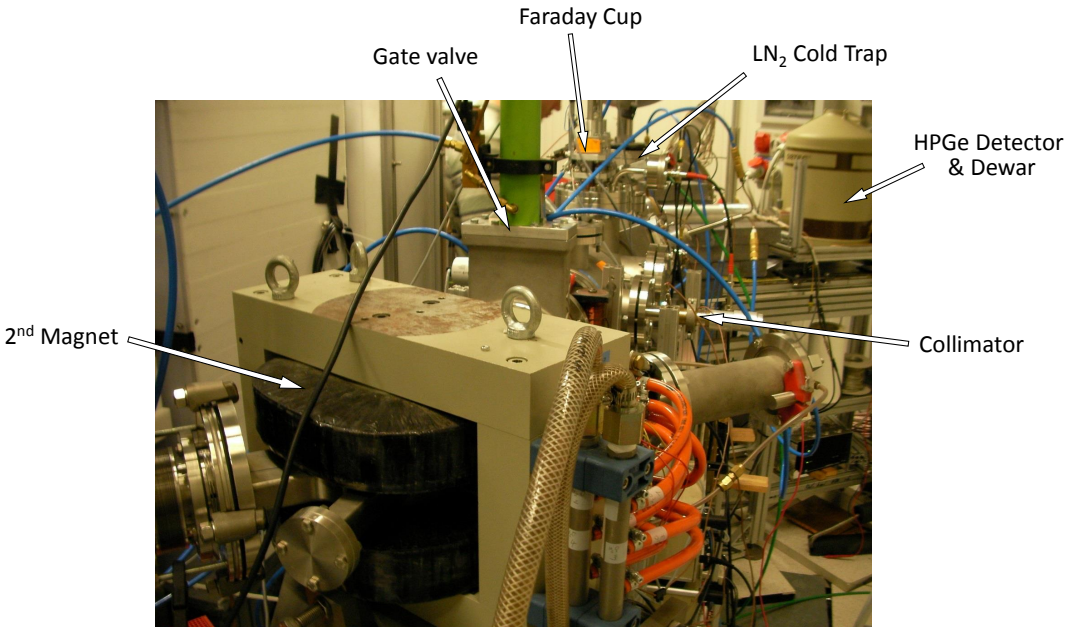

Figure 5.5: Up-stream section of the beam-line, with several key components indicated.

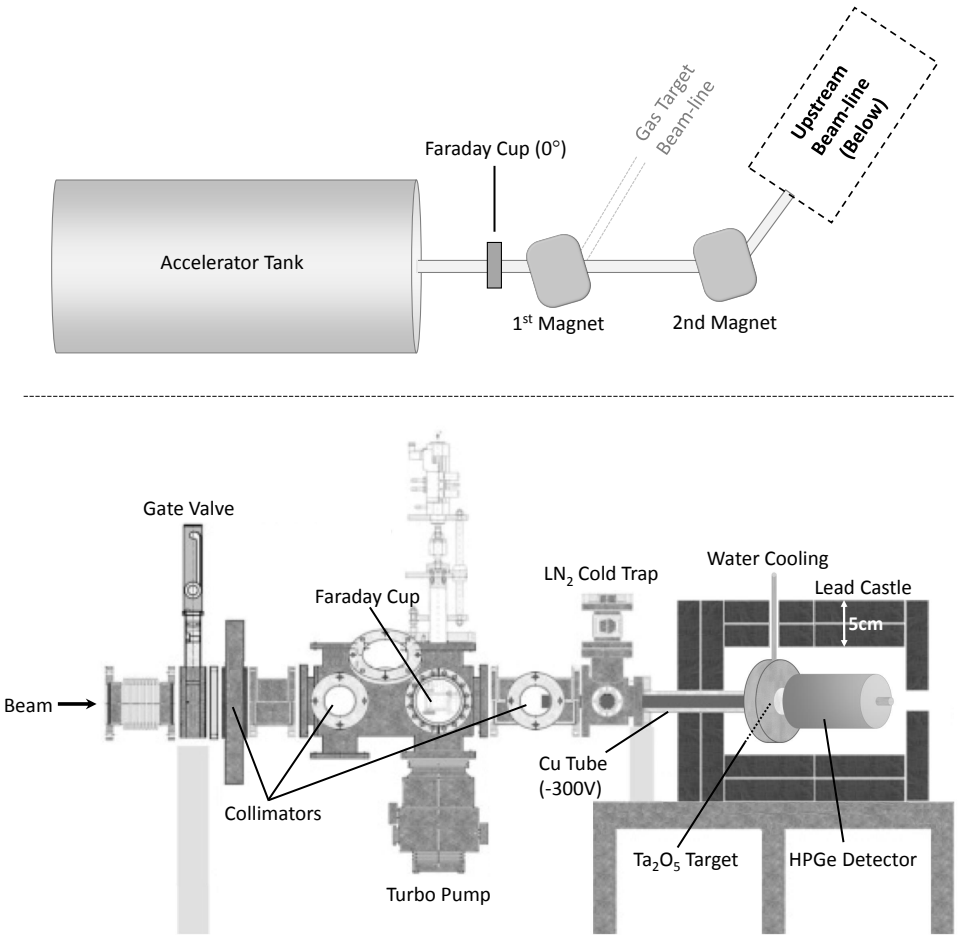

Figure 5.6: Top: Sketch of the 400kV LUNA accelerator facility. Bottom: A diagram illustrating the upstream portion of the beam-line employed in the present investigation.

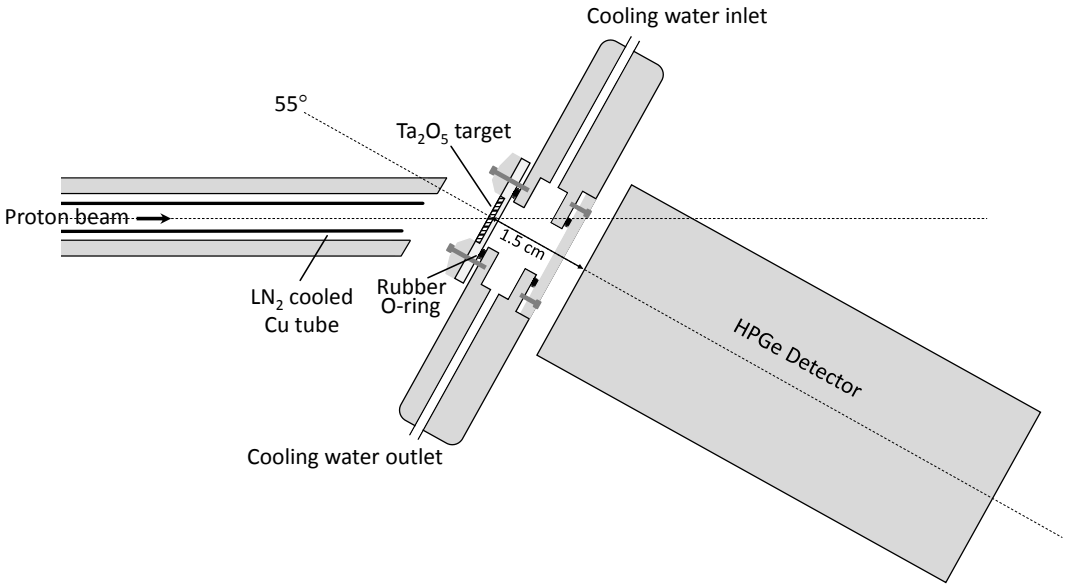

Figure 5.7: Diagram (not to scale) showing the geometry of the target chamber and HPGe detector. The entire target holder assembly (including the exit window) is constructed from stainless steel.

study describing all aspects of the production in addition to a comprehensive analysis of the properties and behaviour of these Ta_2O_5 targets can be found in [60].

The Ta_2O_5 targets required for the present study of the $^{17}O(p,\gamma)^{18}F$ reaction were produced by anodic oxidation of thin tantalum disks (0.3 mm × 40 mm diameter) in isotopically enriched ^{17}O water. This technique has previously been shown to produce homogeneous targets of uniform stochiometry [61]. Prior to anodisation, the tantalum disks were bathed in a citric acid solution for approximately 1 hour at a temperature of 90°C. This etching phase was intended to remove surface impurities and prepare the tantalum for the anodisation process. Citric acid was specifically chosen to avoid fluorine, which gives rise to an intense γ-ray background which hampers the analysis of our spectra at certain measured energies (Chapter 6).

Following the preparation described above, the tantalum disks were immersed in an electrolyte solution consisting of 0.1 mol potassium iodide (KI) salt and the isotopically enriched oxygen water. The ^{17}O content of the water (provided by Cambridge Isotope Laboratories Inc. [62]) was approximately 65-70% but also contained a small amount of ^{18}O ($\sim$5%) for reasons that will be discussed in Chapter 6. A gold-nickel cathode was brought into contact with the surface of the electrolyte solution and used to gradually increase the voltage up to a maximum value of 200 V. This initiated the growth of the oxide layer, at a rate that depends on the applied voltage and the temperature of the electrolyte solution [61]. A diagram of the apparatus used to carry out this procedure is shown in Figure 5.8. Empirically, the formation of Ta_2O_5 as a result of anodic oxidation has been found to obey the following relationship [61]:

$$\frac{I}{d} = a - b \ln t \tag{5.3}$$

where d is the depth of the Ta_2O_5 formed at time, t, after the application of a current of magnitude I. The constant coefficients a and b are temperature dependent parameters. Following a series of tests, the best growth rate was observed at an optimum temperature of 25°C, which was maintained using circulating water.

A photograph of one of the Ta_2O_5 targets produced for this study, before and after beam exposure, is shown in Figure 5.9.

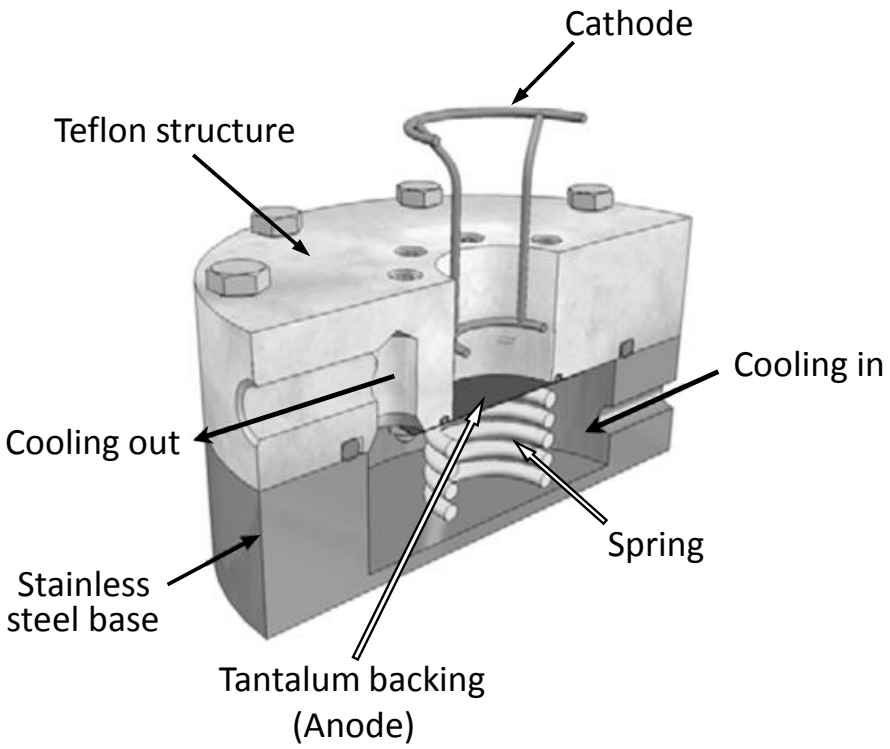

Figure 5.8: Cross-sectional view of the anodisation apparatus used to produce the Ta_2O_5 targets used in this study. The tantalum disk located at the centre of the device acted as the cathode, while a moveable gold-nickel basket acted as the cathode. The electrolytic solution (containing potassium salt in solution with 70% ^{17}O enriched water) filled the cavity directly above the surface of the tantalum. Refrigerated water was circulated below the tantalum backing in order to maintain a constant temperature. Figure adapted from [60].

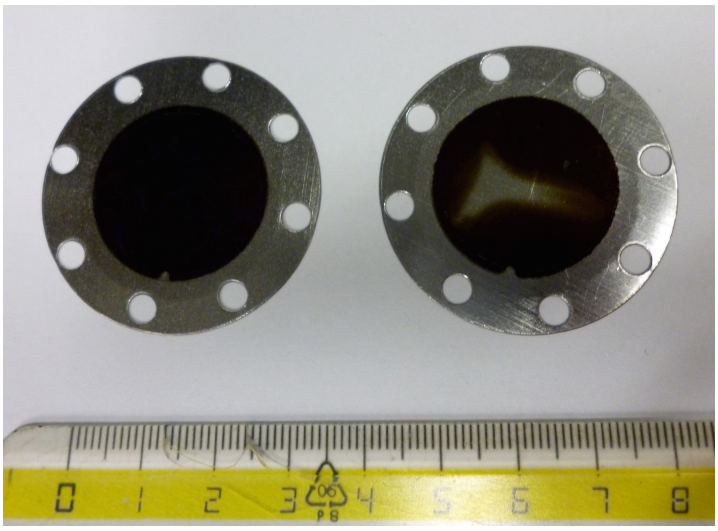

Figure 5.9: Photograph of one of the Ta_2O_5 targets used in the present study before (left-hand image) and after (right-hand image) exposure to the proton beam.

5.5 Activation measurements

As an alternative approach, the activation technique has also been employed in order to investigate the $^{17}O(p,\gamma)^{18}F$ reaction. This method relies on detecting the 511 keV γ rays that are emitted following the β^+ decay of ^{18}F in order to infer the reaction cross section.

The first step in implementing the activation technique involves bombarding a ^{17}O enriched target with protons, thus leading to the accumulation ^{18}F produced via the $^{17}O(p,\gamma)^{18}F$ reaction. This is carried out using Ta_2O_5 targets (produced following the procedure describe above) and the same setup as for the prompt γ-ray measurements. The irradiated targets are then transferred to the low background counting facility of LNGS, the subterranean low level assay (STELLA) [63]. A HPGe detector fully enclosed (4π geometry) inside a 30 cm thick lead and copper shield, continuously flushed with nitrogen[5], was used to detect annihilation γ rays emitted from the target. Spectra were acquired at regular intervals over the course of several hours, allowing the half-life of ^{18}F to be determined and compared with the literature value. The $^{17}O(p,\gamma)^{18}F$ reaction cross section was inferred from measuring the yield of the 511 keV γ rays that

[5]Circulating nitrogen removes radon, which is a contaminant γ-ray emitter present in trace amounts in the natural environment.

result from electron-positron annihilation following the β^+ decay of ^{18}F. One advantage of performing measurements using the activation technique is that no corrections due to the effects of true coincidence summing are required (since no decay cascade occurs).

Although I was not actively involved in analysing the data acquired during the activation measurements, they represent an important point of comparison for the results obtained in the present work. The results from the activation measurements are presented in Chapter 7.

Chapter 6

Data Analysis and Results

In this chapter I describe the data analysis procedure and present the experimental results from the current study of the $^{17}O(p,\gamma)^{18}F$ reaction. In order to measure the reaction cross section, the thickness of our Ta_2O_5 targets and the detection efficiency of our setup had to be determined. Sections 6.1 and 6.2 describe how this information was obtained. Sections 6.3 to 6.8 are devoted to the measured resonant and non-resonant contributions to the total reaction cross section. Finally, the calculation of the $^{17}O(p,\gamma)^{18}F$ reaction rate is presented in Section 6.9.

6.1 Target behaviour under beam bombardment

Extracting absolute measurements of the $^{17}O(p,\gamma)^{18}F$ reaction cross section relies on accurate information concerning the target thickness, which enters explicitly through Equation 4.8. Understanding how the Ta_2O_5 targets used in this study respond to intense proton bombardment was therefore critical. The precise stochiometric ratio of tantalum to oxygen in our targets influences the effective stopping power, which is also a key ingredient in determining the $^{17}O(p,\gamma)^{18}F$ reaction cross section. Here I describe the methods used to determine the thickness of our targets, while details of the measurements performed to determine the stoichiometry and isotopic composition can be found in Appendix B.

As a consequence of the high beam currents (currents up to 300 μA on target) used in this investigation, target deterioration occurs due to protons scattering

nuclei from the target in a process referred to as *sputtering*. The target thickness and homogeneity can be determined by performing measurements of the yield curve associated with populating a narrow resonance (Chapter 4). Our targets were partially enriched (∼5%) in ^{18}O so that the strong, narrow, ^{18}O(p,γ)^{19}F resonance at $E_{\mathrm{R}} = 143$ keV ($E_{\mathrm{p}} = 151$ keV) could be used for this purpose. The corresponding $E_x = 8138$ keV state in ^{19}F decays to the ground state with the emission of γ rays of energy $E_\gamma = 3908$ keV and $E_\gamma = 4230$ keV (Figure 6.1). The combined yield from these two γ-ray transitions was measured for a range of beam energies in order to produce a complete scan of the target profile, as described in Chapter 4. Figure 6.2 shows an example of a series of such scans performed for a target 98% enriched in ^{18}O.

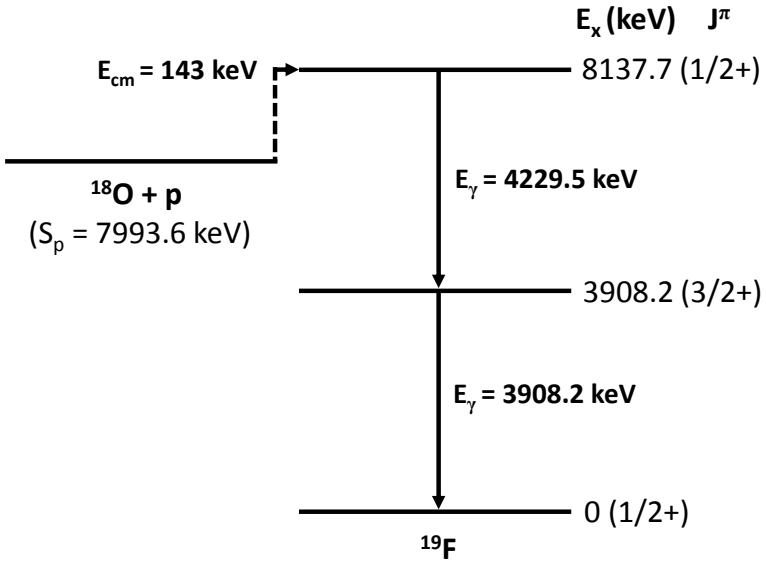

Figure 6.1: Energy level digram for ^{19}F (information from [29]). Only relevant states are shown.

The target profile shown in Figure 6.2 gradually deteriorates as the total accumulated charge on target increases. This is evident from the reduction in overall thickness, which takes place as oxygen is lost from the target.

The experimentally measured yield curve from the $E_{\mathrm{R}} = 143$ keV, ^{18}O resonance, can be fitted[1] using Equation 4.11. In order to determine the thickness

[1]To account for experimental factors such as energy straggling and the resolution of the HPGe detector, the resonance width terms in Equation 4.11 must be modified accordingly.

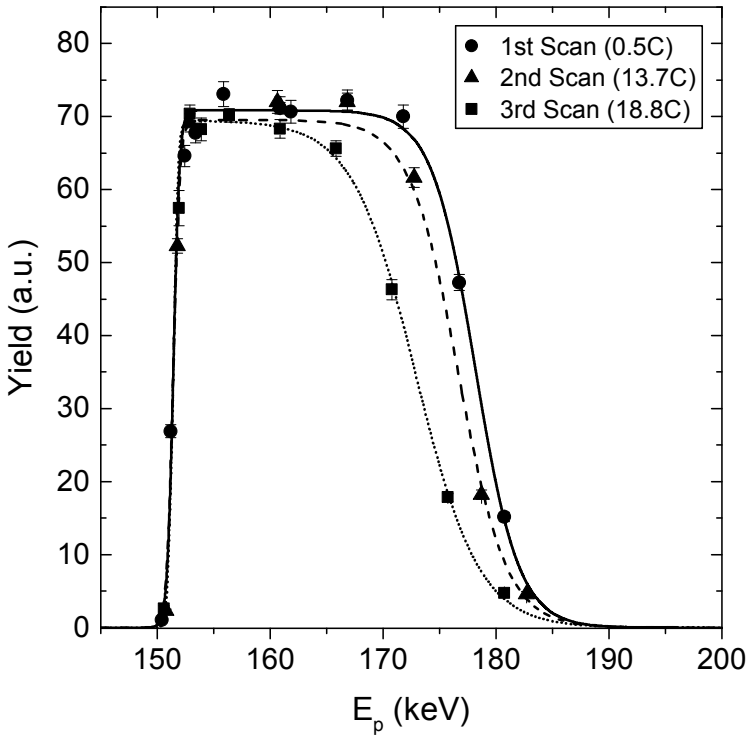

Figure 6.2: A series of target profile scans performed by populating the E_{R}=143 keV, $^{18}O(\mathrm{p},\gamma)^{19}\mathrm{F}$, resonance at a range of beam energies. The thickness of the target is gradually reduced as the amount of accumulated charge increases.

of a given target, I have opted to use an alternative, empirical, formula to fit the measured yield curve (this function is equivalent to Equation 4.11 but analytically simpler to implement):

$$Y = H \frac{1}{1 + e^{\frac{E_R - E_\gamma}{\delta_L}}} \frac{1}{1 + e^{\frac{E_\gamma - E_R - \Delta E}{\delta_R}}} \tag{6.1}$$

where the target thickness is represented by ΔE. The width of the rising and falling edge and plateau height are parametrised by δ_L, δ_R and H, respectively. The resonance energy is $E_{\mathrm{p}} = 151.2$ keV. Performing profile fits for a range of individual targets using Equation 6.1 at different stages of deterioration allows a general relationship between target thickness and accumulated charge to be determined. The resonance scans performed for a selection of the targets used in the present study are shown in Figure 6.3. The difference in plateau height for some of the profile scans shown in Figure 6.3 is not statistically significant.

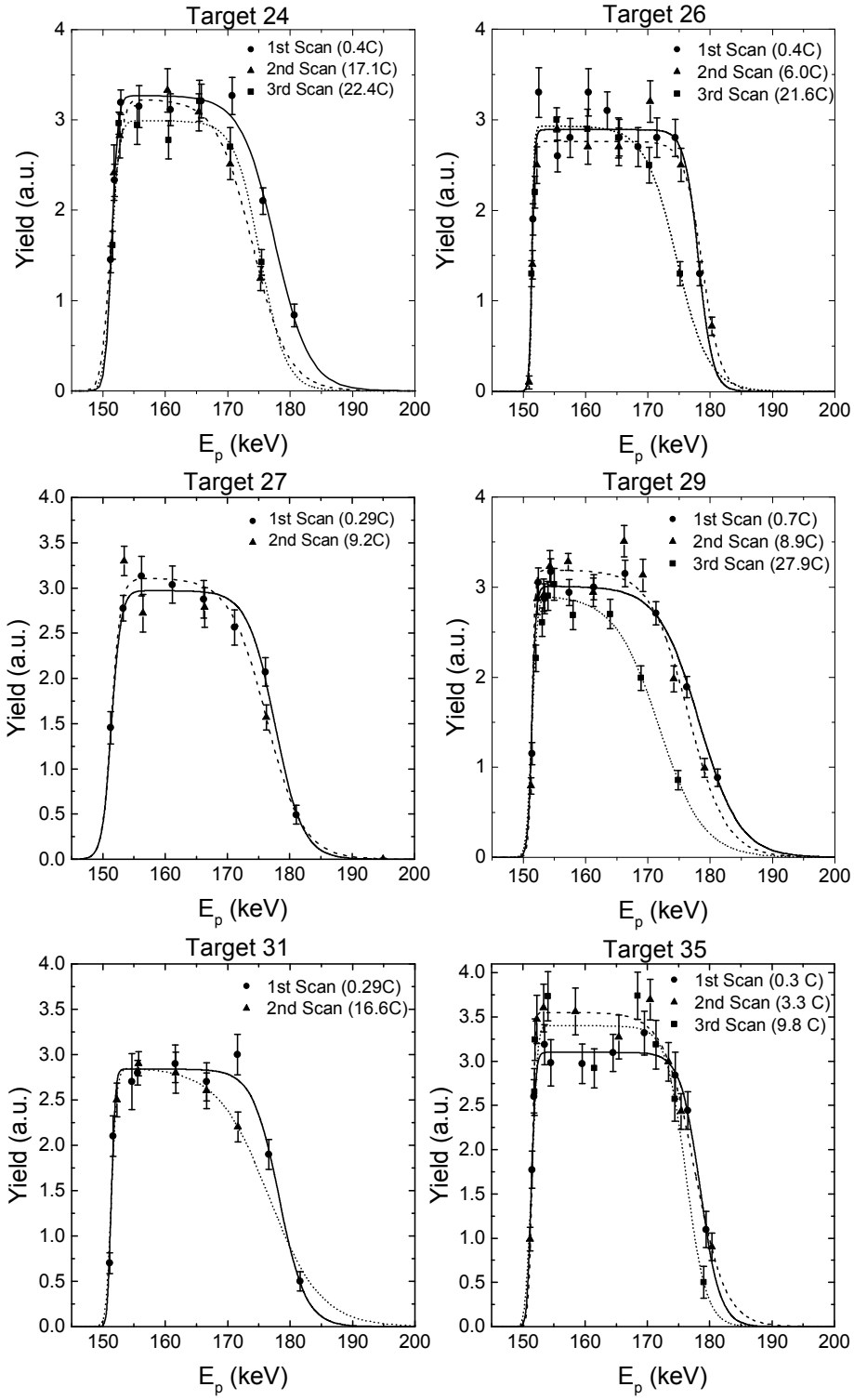

Figure 6.3: Target profile scans performed for a selection of targets used in the present investigation. Most targets begin to show signs of degradation when the total accumulated charge reaches approximately 10C.

Over the course of this investigation measurements were made using many Ta_2O_5 targets, all of which were produced following the procedure described in Section 5.4. Despite the consistent approach used during production, some discrepancies in the rate of degradation were observed for targets produced in different batches. For this reason targets were separated into two groups based on the period in which they were produced.

After fitting the profiles for each target using Equation 6.1, a global fit was performed using a linear function to model the target thickness dependence on accumulated charge. Figure 6.4 presents the results for each of the two separate groups mentioned above. The size of the error bars on each point reflects the variable quality of the profile scans, some of which have too few points to strongly constrain the target thickness. Analysing similar targets together to obtain the average trend ensured that the lack of information that exists for some targets did not adversely effect the accuracy of my results.

The parameter values (intercept and gradient) describing the target thickness as a function of accumulated charge for each of the two groups of targets shown in Figure 6.4 are listed in Table 6.1. The target thickness uncertainty was calculated from the uncertainty associated with the fit parameters and was approximately 4-7% for the targets used in the measurement of the $^{17}O(p,\gamma)^{18}F$ reaction. In cases where complete and precise target profile scans did exist, the target thickness was estimated directly from those data.

In order to calculate the target thickness at a given beam energy, the results obtained from the parameterisation presented in Table 6.1 must be multiplied by the ratio of stopping powers at each energy ($\Delta E_1/\Delta E_2 = \epsilon(E_1)/\epsilon(E_2)$). This was necessary since the target thickness (in energy units) depends on the beam energy. On average this correction was approximately 10%.

Table 6.1: The intercept and gradient parameters associated with the two linear fits shown in Figure 6.4.

	Intercept (keV)	Gradient (keV/C)
Batch 1	26.88 ± 0.16	-0.184 ± 0.012
Batch 2	26.8 ± 0.6	-0.31 ± 0.04

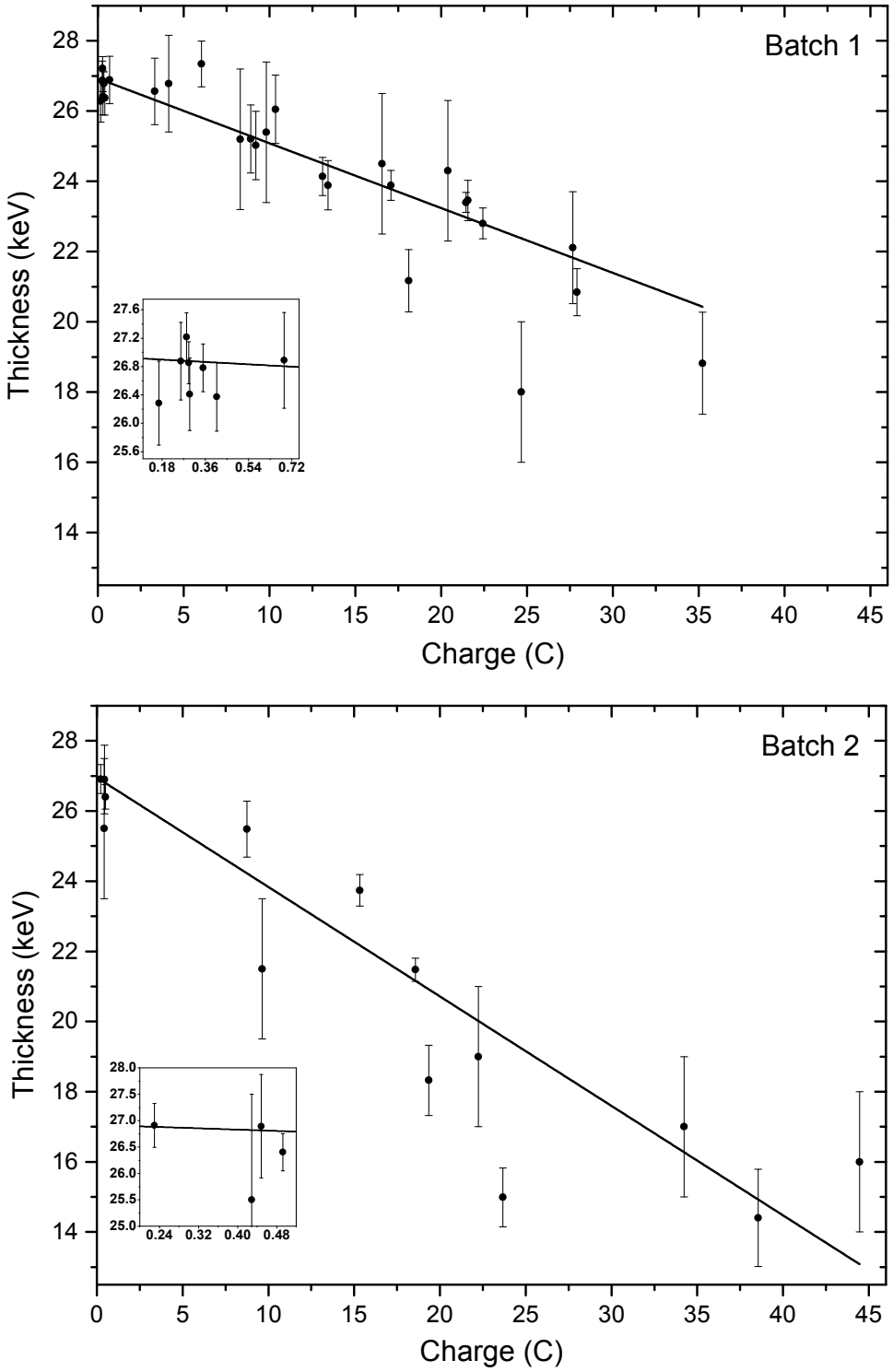

Figure 6.4: Target thicknesses measured for each batch of targets used in the present study. The solid lines represent linear fits to the data (relevant parameters presented in Table 6.1).

6.2 Detector efficiency and calibration

6.2.1 Efficiency

The detection efficiency of our setup was determined using calibrated radioactive sources, and γ rays from the ^{14}N(p,γ)^{15}O reaction.

Gamma rays from the decay cascade of the E_{R} = 259 keV resonance in ^{14}N(p,γ)^{15}O cover an energy range of E_{γ}= 0.7-7.6 MeV (Figure 6.5). Measuring the yield of the primary and secondary γ rays from this resonance, which was populated using a TiN (evaporated) ^{14}N target, allowed the efficiency to be constrained over a relatively wide energy region. The efficiency for the lower energy range between E_{γ} = 650-1200 keV was mainly fixed by the radioactive sources. The sources used were ^{137}Cs and ^{60}Co, which had an activity of approximately 3.44 and 0.85 kBq ($\pm$ 2%), respectively, at the time of measurement.

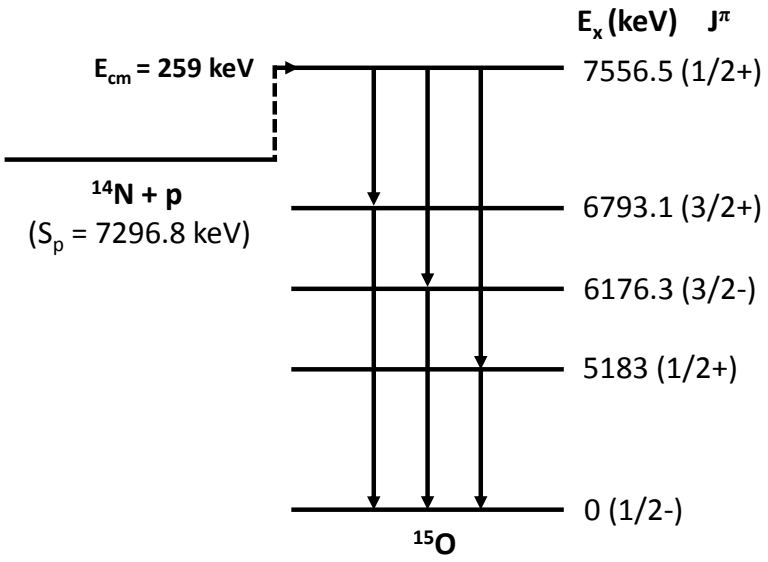

Figure 6.5: Gamma-ray decay scheme associated with populating the ^{14}N + p resonance at E_{R} = 259 keV (information from [29]).

Measurements of the γ-ray yield for each of the transitions from ^{14}N(p,γ)^{15}O, ^{137}Cs and ^{60}Co were made at a range of different distances, d, between the source (or target surface) and front face of the detector. This was done in order to

investigate the influence of true coincidence summing (TCS) (Chapter 4) on our measurements and determine the efficiency of our setup both as a function of γ-ray energy and detector distance. The distances chosen were 1.5, 6.5, 16.5 and 20.5 cm, with the closest distance of 1.5 cm corresponding to the geometry used for all measurements of the ^{17}O(p,γ)^{18}F reaction. In close geometry the effects of summing-out were as high as 20%, while corrections of less than 2% were necessary for the measurements performed at d = 20.5 cm.

The empirical function used to model the full-energy peak efficiency takes the form [64]:

$$\eta_{ph}(d, E_\gamma) = Ae^{[a+b\ln(E_\gamma)+c\ln(E_\gamma)^2]} \tag{6.2}$$

where a, b, and c are free parameters and A is a function of distance, d, that includes the detector dimensions:

$$A = \frac{1 - e^{\frac{d+d_0}{1+\beta\sqrt{E_\gamma}}}}{(d+d_0)^2} \tag{6.3}$$

Here, d_0 is the distance from the point of interaction within the detector and the detector's front face; β is a free parameter. To model the total efficiency the following empirical formula was used [64]:

$$\ln\left(\frac{\eta_{ph}}{\epsilon_{tot}}\right) = k_1 + k_2\ln(E_\gamma) + k_3[ln(E_\gamma)]^2 \tag{6.4}$$

where k_1, k_2 and k_3 are free parameters.

A simultaneous chi-squared fit to the γ-ray yields recorded at all four distances was performed with the parameters mentioned above free to vary (see [65] and [66] for a similar procedure). The expected counts associated with the ^{14}N(p,γ)^{15}O decay cascade were determined using Equation 4.8. The relevant branching ratios for γ-ray transitions in ^{15}O were free to vary within their quoted uncertainty [65], as was the effective stopping power (reflecting the lack of information concerning the ^{14}N abundance in the target).

The resultant efficiency-versus-energy curves for each distance, d, are shown in Figure 6.6 alongside the experimental data. The experimental points have been corrected for the effects of TCS and the associated error bars include both statistical (2-4%) and activity/charge (2-3%) uncertainties. The uncertainty

associated with the efficiency was estimated by varying the fit parameters within their uncertainty and calculating the sigma value of the resultant gaussian distribution of efficiency values. This procedure led to an uncertainty of approximately 5% on η_{ph}.

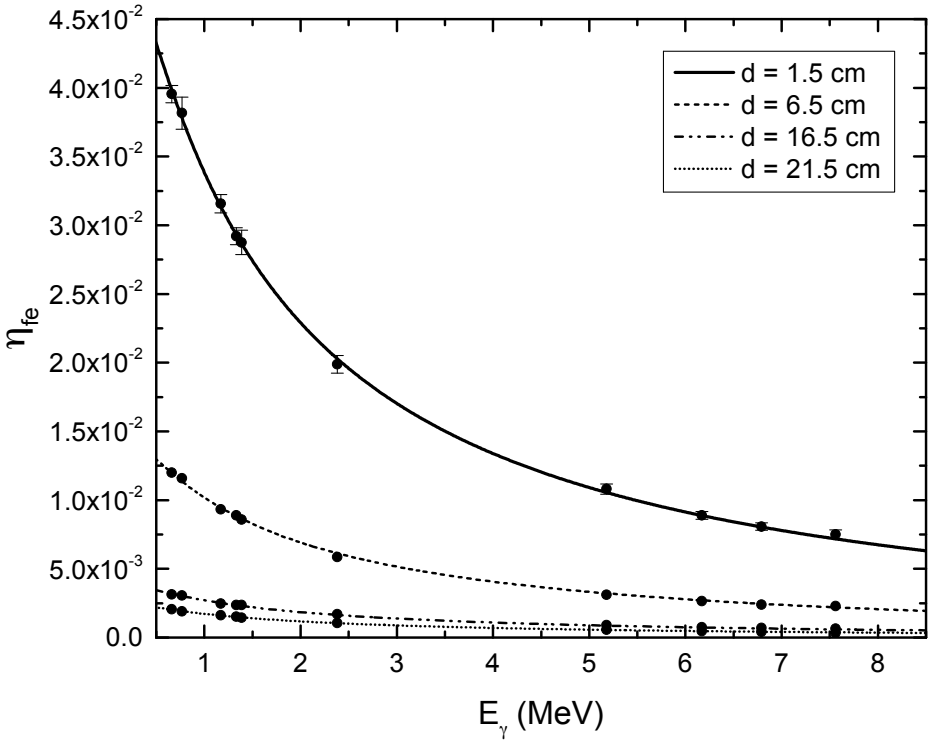

Figure 6.6: Measured full-energy peak (fractional) efficiency (solid points) as a function of γ-ray energy for several different target-to-detector distances. The solid lines represent fits to the experimental data, as described in the text. All measurements of the ^{17}O(p,γ)^{18}F reaction were performed at the closest distance (d = 1.5 cm).

6.2.2 Calibration and resolution

The HPGe detector used in this study was calibrated with reference to several common natural background lines and the four strongest γ rays from the ^{17}O(p,γ)^{18}F reaction. A linear fit (Figure 6.7) was performed in order to determine the following relationship between γ-ray energy and spectrum channel number:

$$E_\gamma = 1.061 \times \text{channel} - 67.3 \quad \text{(keV)} \tag{6.5}$$

This calibration was found to remain consistent throughout the course of the investigation.

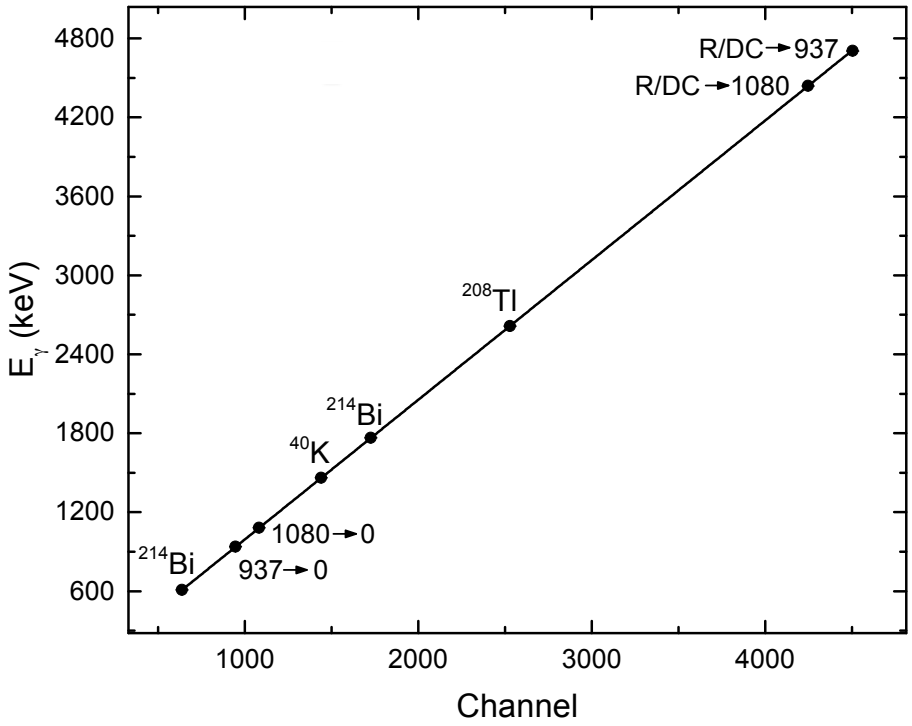

Figure 6.7: Plot of γ-ray energy versus channel number for several natural background lines and the four most intense γ-ray transitions from the ^{17}O(p,γ)^{18}F reaction. The detector calibration was determined by performing a linear fit to the data.

The resolution of the detector was determined as a function of γ-ray energy from the width of several γ-ray lines from natural background and radioactive sources (^{137}Cs and ^{60}Co), which cover an energy range E_γ = 0.6-3 MeV. The resolution was approximately 1-3 keV FWHM between E_γ = 1-5 MeV.

6.3 General considerations on acquired spectra

The first step in the analysis of the γ-ray spectra acquired in the present study of the ^{17}O(p,γ)^{18}F reaction involved identifying all γ rays from the decay cascade of ^{18}F, and gaining an understanding of any background likely to interfere with the analysis of these transitions. Two sample spectra measured at energies of $E_{\rm R}$ = 183 keV (on-resonance) and $E_{\rm cm}$ = 250 keV (off-resonance) are shown in

Figure 6.8. The off-resonance spectrum (lower panel in Figure 6.8) was obtained from a single measurement, while the spectrum measured at the $E_R = 183$ keV resonance energy is the sum of spectra from several measurements. For each of the two spectra shown in Figure 6.8, the total charge was approximately 15C. Time-normalised background spectra are shown in grey. All primary transitions from the $^{17}O(p,\gamma)^{18}F$ reaction are labeled as R(/DC)→X, while the secondary transitions are labelled by the energy of the emitted γ ray. The energy level scheme of ^{18}F is shown in Figure 6.9.

In addition to the transitions originating from the $^{17}O(p,\gamma)^{18}F$ reaction, a large number of background lines have also been identified. Some of the most intense beam-induced background transitions arise from proton capture reactions with ^{11}B and ^{19}F, which exist as contaminants in our Ta_2O_5 targets. The intense background line at $E_\gamma = 6.1$ MeV is due to a strong $^{19}F(p,\alpha\gamma)^{16}O$ resonance populated at an energy of $E_R = 323.3$ keV. At beam energies between $E_{cm} =$ 310-360 keV, γ rays from the decay of this resonance severely hampered the analysis of the most intense transition (R/DC→937 keV) in ^{18}F. For this reason, no measurements of the $^{17}O(p,\gamma)^{18}F$ reaction cross section were performed in this energy region. Another contaminant present in our targets is ^{12}C. The $^{12}C(p,\gamma)^{13}N$ reaction is the origin of the strong peak visible in Figure 6.8 at approximately 2.2 MeV, which results from transitions directly to the ground state of ^{13}N.

6.4 Data taking procedure

The data obtained in the present study of the $^{17}O(p,\gamma)^{18}F$ reaction were acquired following a careful experimental procedure. First the condition and thickness of the target was evaluated by performing a resonance profile scan as described in Chapter 4. Following the scan of the target, the accelerator was tuned to the desired measurement energy, the beam focused onto the centre of the target and its intensity maximised as described in Section 5.3. Data were acquired until between 5-10 C of charge had been accumulated on target.

A second scan of the target profile was then performed in order to check for any degradation in thickness or reduction in maximum yield. Provided no signs of target degradation were observed the beam was re-tuned to the original beam

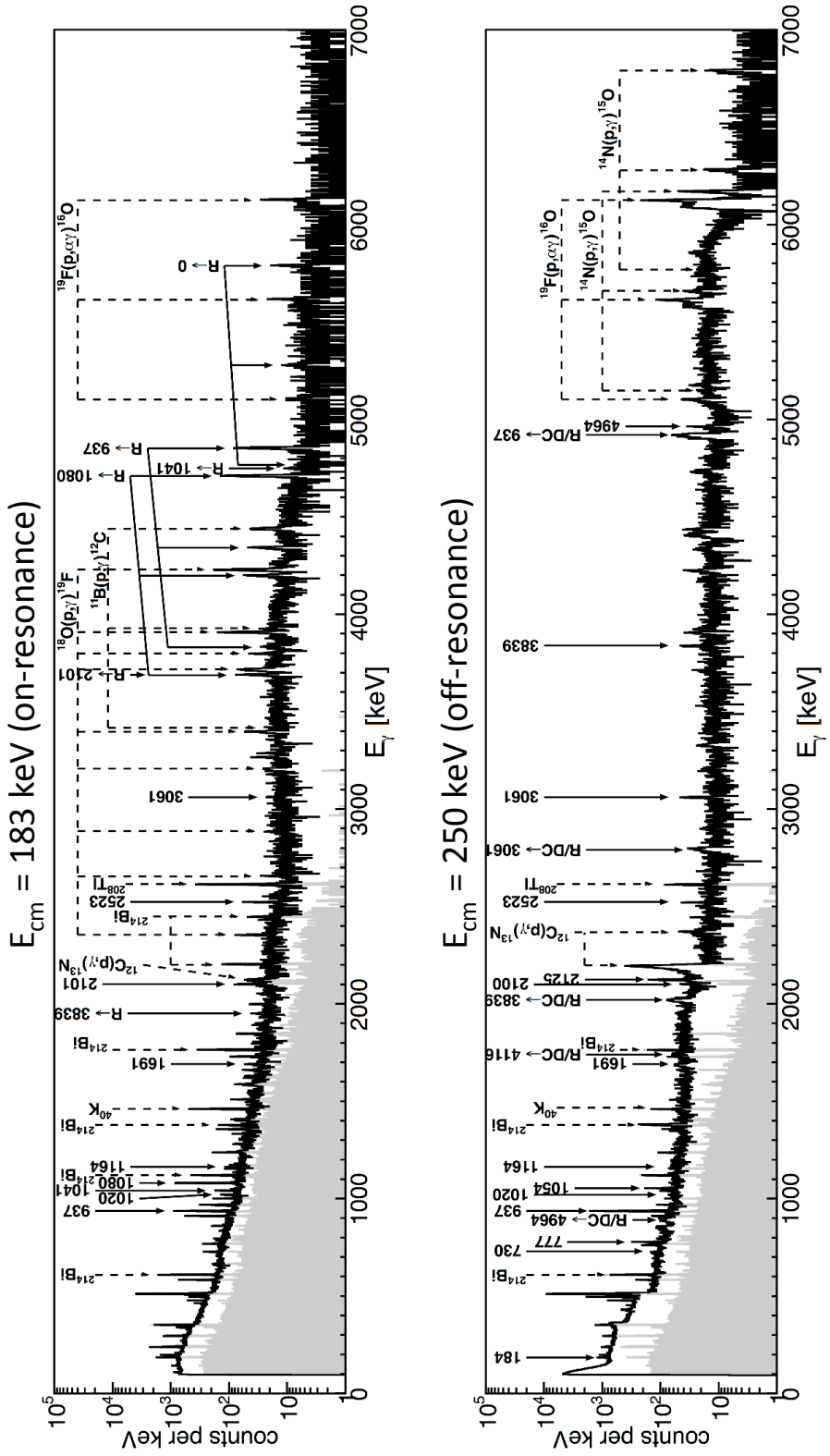

Figure 6.8: Sample spectra measured at energies of $E_{\mathrm{R}} = 183$ keV (on-resonance - top panel) and $E_{\mathrm{cm}} = 250$ keV (off-resonance - lower panel). All primary transitions from the $^{17}\mathrm{O}(p,\gamma)^{18}\mathrm{F}$ reaction are labeled as R(/DC)→X, while the secondary transitions are labelled by the energy of the emitted γ ray. The single- and double-escape peaks (Appendix A) are also indicated. Time normalised background spectra are shown in grey.

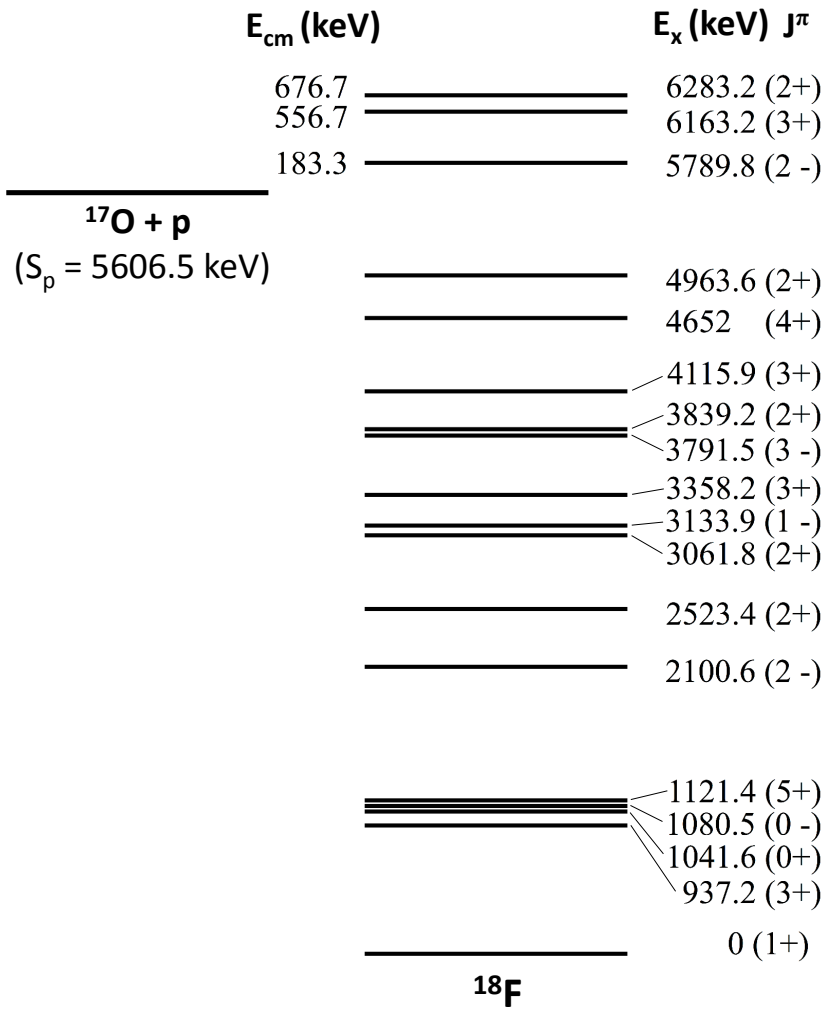

Figure 6.9: The energy level scheme for ^{18}F (information from [29]). Only levels relevant to the present study are shown.

energy and the long measurement recommenced. This cycle of long measurements (typically performed over many hours) of the ^{17}O(p,γ)^{18}F reaction alternated with target scans was continued until the maximum yield obtained in the scan (plateau height) was appreciably lower than that observed in the initial measurement. The lead shield surrounding the detector was then removed and a fresh target installed inside the target chamber. The detector was then carefully re-positioned, the lead shield re-built, and a new measurement started. Figure 6.10 provides graphical representation of the procedure described above.

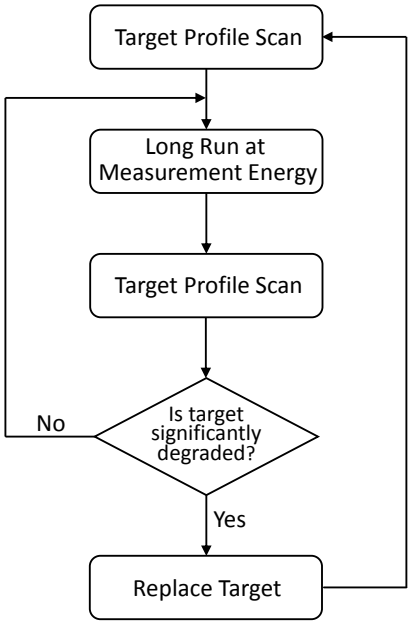

Figure 6.10: Flow chart depicting the data taking procedure employed in the present investigation of the ^{17}O(p,γ)^{18}F reaction.

The total non-resonant S-factor for the ^{17}O(p,γ)^{18}F reaction, and the strength of the $E_{\rm R}$ = 183 keV resonance have been determined by analysing the prompt γ-ray yield associated with transitions to and from the various states populated in ^{18}F. These measurements have been performed in the energy range $E_{\rm cm}$=167-370 keV. Table 6.2 provides information relating to each of the runs analysed in the present study.

In the case of the non-resonant data, the primary and secondary transitions have been analysed separately in order to provide two independent measurements

of the total non-resonant S-factor.

6.5 Primary transitions analysis and results

The γ-ray peak shape associated with a non-resonant primary transition, measured following the thick-target yield approach, was discussed in Chapter 4. For a primary γ-ray transition, the expression for the number of counts, $N_{\rm i}$, observed in channel i (bin width δE) of the spectrum is given by:

$$N_i = N_p \frac{\sigma(E_{p,i})\eta(E_{\gamma,i})P(E_{p,i})}{\epsilon(E_{p,i})}\delta E \tag{6.6}$$

where $\sigma(E_{\rm p,i})$ is the reaction cross section; $N_{\rm p}$ is the number of protons incident on the target (calculated from the accumulated charge); $\eta(\mathrm{E}_{\gamma,i})$ is the full-energy peak efficiency; $\epsilon(E_{\rm p,i})$ is the effective stopping power; and the function $P(E_{\rm p,i})$ models the target profile. In this case, a function with the same form as Equation 6.1 was used for $P(E_{\rm p,i})$, where the relevant parameters (target thickness, rising and falling edge widths) are determined from the target profile fits described in Section 6.1.

The cross section in equation 6.6 can be decomposed into a direct capture (DC) term and a term representing the combined contribution from the tails of the $E_{\rm R} = 557$ keV and $E_{\rm R} = 677$ keV broad resonances. Since the energy dependence of the broad resonance cross section is qualitatively similar to that of the DC process inside the relatively small energy range covered by the target (typically $\Delta E = 20$ keV for the present measurements), it was impossible to disentangle each contribution for a given transition purely based on the γ-ray peak shape. However, the broad resonance contribution for a transition to a given state in ^{18}F can be estimated by calculating the total broad resonance cross section at the relevant measurement energy using Equation 2.26. Information on the partial widths (listed in Table 6.3) of the $E_{\rm R} = 557$ keV and $E_{\rm R} = 677$ keV broad resonances, as well as the corresponding branching ratios (used to weight the broad resonance cross section contribution for a given primary transition) was taken from the recent work of Kontos *et al.* [43]. The penetrability factors appearing in Equation 2.26 were calculated by implementing routines from the GNU scientific library (GSL) [67].

Table 6.2: Information relating to each of the experimental runs dedicated to measuring the resonant and non-resonant components of the $^{17}O(p,\gamma)^{18}F$ reaction cross section. The run corresponding to the $E_R = 183$ keV resonance measurement is highlighted in bold.

Target I.D.	E_p (keV)	I (μA)	Time (h)	Charge (C)	^{17}O (%)	Target thickness ΔE (keV)	Effective stopping power ϵ_{eff} (10^{-15}eVcm^2/atom)
25 (B1)	186.1	265.5	34.9	33.4	65.7	23.3	41.6
28 (-)	**198.1**	**364.2**	**8.1**	**10.7**	**66.1**	**23.0**	**38.6**
27 (B1)	220.7	339.1	12.4	15.1	64.5	22.3	40.2
24 (B1)	229.9	253.3	17.4	15.9	65.7	23.4	38.9
26 (B1)	250.1	283.3	14.6	14.9	65.7	21.9	37.8
27 (B1)	261.0	363.1	6.5	8.4	64.5	23.1	37.9
31 (B1)	275.1	306.0	14.3	15.8	64.3	22.0	37.2
19 (B2)	281.7	217.0	23.0	18.0	67.3	16.4	35.3
19 (B2)	300.1	209.4	17.4	13.1	67.3	20.3	34.4
26 (B1)	328.9	242.5	5.2	4.6	65.7	20.8	33.9
24 (B1)	388.9	261.6	2.8	2.6	65.7	17.4	31.5
24 (B1)	398.8	273.2	2.0	2.0	65.7	16.9	31.2

Table 6.3: Partial width parameters for the $E_{\mathrm{R}} = 556$ and $E_{\mathrm{R}} = 677$ keV broad resonances, as determined in the recent study of Kontos *et al.* [43].

	$E_R = 556$ keV	$E_R = 677$ keV
Γ_p (keV)	14.1 ± 0.3	11.3 ± 0.2
Γ_γ (eV)	0.632 ± 0.085	1.41 ± 0.17
Γ_α (eV)	8 ± 1	30 ± 4

The total cross section at an energy E_{cm} for a given primary transition, t, was parameterised using the equation:

$$\sigma_t(E_{\mathrm{cm}}) = E_{\mathrm{cm}}\frac{S_{DC}}{e^{-2\pi\eta}} + b_{t,557}\sigma_{557}(E_{\mathrm{cm}}) + b_{t,677}\sigma_{677}(E_{\mathrm{cm}}) \tag{6.7}$$

where S_{DC} represents the DC S-factor and σ_x refers to the cross section contributions from the tails of the two broad resonances at $E_{\mathrm{R}} = 566$ and 677 keV. Broad resonance branching ratios are denoted by $b_{\mathrm{t,x}}$.

To obtain an expression for the total counts expected in channel i of the γ-ray spectrum, Equation 6.6 was summed with a function that describes the background in the region of interest. This consisted of a linear component combined with one or more Gaussian functions where necessary. The resulting function was convoluted with a Gaussian in order to reproduce the broadening effect due to the finite resolution (approximately 1-3 keV FWHM between $E_\gamma =$ 1-5 MeV) of our detector.

A program I have written using RooFit (an analysis package based on ROOT [68]) was used to implement the procedure described above and to arrive at a function capable of describing the γ-ray peak shape for a given primary transition. A χ^2 fit was performed for each observed transition, with the DC parameter, S_{DC}, free to vary. The extracted value of S_{DC}, combined with the calculated broad resonance contribution, allowed the total cross section parameterisation and hence the total S-factor to be determined at each measurement energy.

This γ-ray peak shape approach was applied to fit all primary transitions strong enough to exhibit a clear structure. For weaker transitions containing an insufficient number of counts to make this method reliable, the total yield in the region of interest defined by the target thickness (at the relevant beam energy) was used to determine the S-factor according to the thick-target yield approach

described in Chapter 4. The results were consistent with the γ-ray peak shape method for well-defined peaks.

The final stage in the analysis of the primary transition S-factor consisted in making the necessary corrections due to the effects of true coincidence summing (TCS). An iterative procedure was employed to determine the primary branching ratios required to calculate the extent of TCS for each transition (using Equations 4.18 and 4.19):

- Calculate the primary branching ratios at each measured energy without any correction due to TCS. In this first approximation the branching ratios are simply given by the ratio of the S-factor for a particular primary transition and the sum of the S-factors for *all* observed transitions.
- Calculate the amount of summing-in and summing-out based on these branching ratio values and correct the S-factor for each transition accordingly.
- Re-calculate the primary branching ratios based on these new S-factor results.

The last two steps of this process are then repeated until the branching ratios converge to constant values. Typically this occurs after only one or two iterations.

The results obtained from analysing the primary transitions from the ^{17}O(p,γ)^{18}F reaction are presented in Table 6.4. The total S-factor, $S_{\rm tot}$, at a given effective energy (calculated using Equation 4.10) is calculated by summing the contributions from each transition. The uncertainty in $S_{\rm tot}$ was calculated by summing in quadrature the statistical uncertainty and the uncertainty associated with the target thickness (approximately 5% on average). All of the values listed in Table 6.4 are calculated directly from observed yields. Where information is not listed (for instance due to the presence of natural or beam-induced background masking the signal peak), the S-factor values used to determine S_{tot} were based on interpolations of measurements performed at similar energies.

The two most intense primary transitions, R/DC→937 and R/DC→3839, account for over 50% of the total yield. Fits to the peak shape associated with the R/DC→937 transition are shown in Figures 6.11 and 6.12 for all energies investigated (Table 6.2).

Table 6.4: Primary transition S-factor results in units of keV barn. The R/DC→3791, R/DC→4116 and R/DC→4652 contributions were determined from the secondary transition analysis (Section 6.6). Where information for a given transition is not listed, the S-factor value used to calculate S_{tot} was estimated by interpolating the results obtained at similar measurement energies. The uncertainty (in brackets) in S_{tot} includes both statistical and target thickness uncertainties.

E_{cm} [keV]	$R/DC \rightarrow 937$	$R/DC \rightarrow 1120$	$R/DC \rightarrow 2523$	$R/DC \rightarrow 3061$	$R/DC \rightarrow 3791$
204	2.4(3)	0.6(3)	–	0.51(16)	–
210	2.2(3)	0.5(3)	0.34(19)	0.29(15)	–
228	2.06(17)	0.5(2)	0.20(10)	0.53(11)	0.24(14)
238	2.02(15)	0.85(18)	0.24(9)	0.69(9)	–
250	2.30(12)	0.71(10)	0.21(7)	0.60(5)	–
258	2.34(13)	0.65(15)	0.27(7)	0.62(7)	0.47(13)
274	2.40(12)	0.82(11)	–	0.58(5)	0.35(9)
301	3.0(2)	0.8(3)	0.33(10)	0.60(14)	0.30(12)
359	3.4(3)	1.0(3)	0.44(10)	0.86(9)	0.40(15)
370	3.6(3)	0.9(2)	0.52(9)	0.90(9)	0.54(17)

E_{cm} [keV]	$R/DC \rightarrow 3839$	$R/DC \rightarrow 4116$	$R/DC \rightarrow 4652$	$R/DC \rightarrow 4964$	S_{tot}
204	1.0(2)	–	–	0.5(2)	6.1(7)
210	1.5(3)	0.5(2)	–	0.33(13)	6.1(7)
228	1.18(17)	0.60(12)	–	0.46(10)	5.9(5)
238	0.95(16)	0.45(12)	0.07(5)	0.52(8)	6.1(5)
250	1.06(8)	0.56(7)	–	0.48(5)	6.3(4)
258	1.35(6)	0.72(11)	–	0.25(7)	6.8(4)
274	1.38(8)	0.55(7)	0.08(4)	0.20(5)	6.7(4)
301	1.38(15)	0.77(11)	0.16(9)	0.30(15)	7.6(6)
359	1.9(2)	0.71(8)	–	0.51(6)	9.3(6)
370	1.8(2)	0.69(8)	0.11(6)	0.56(6)	9.6(6)

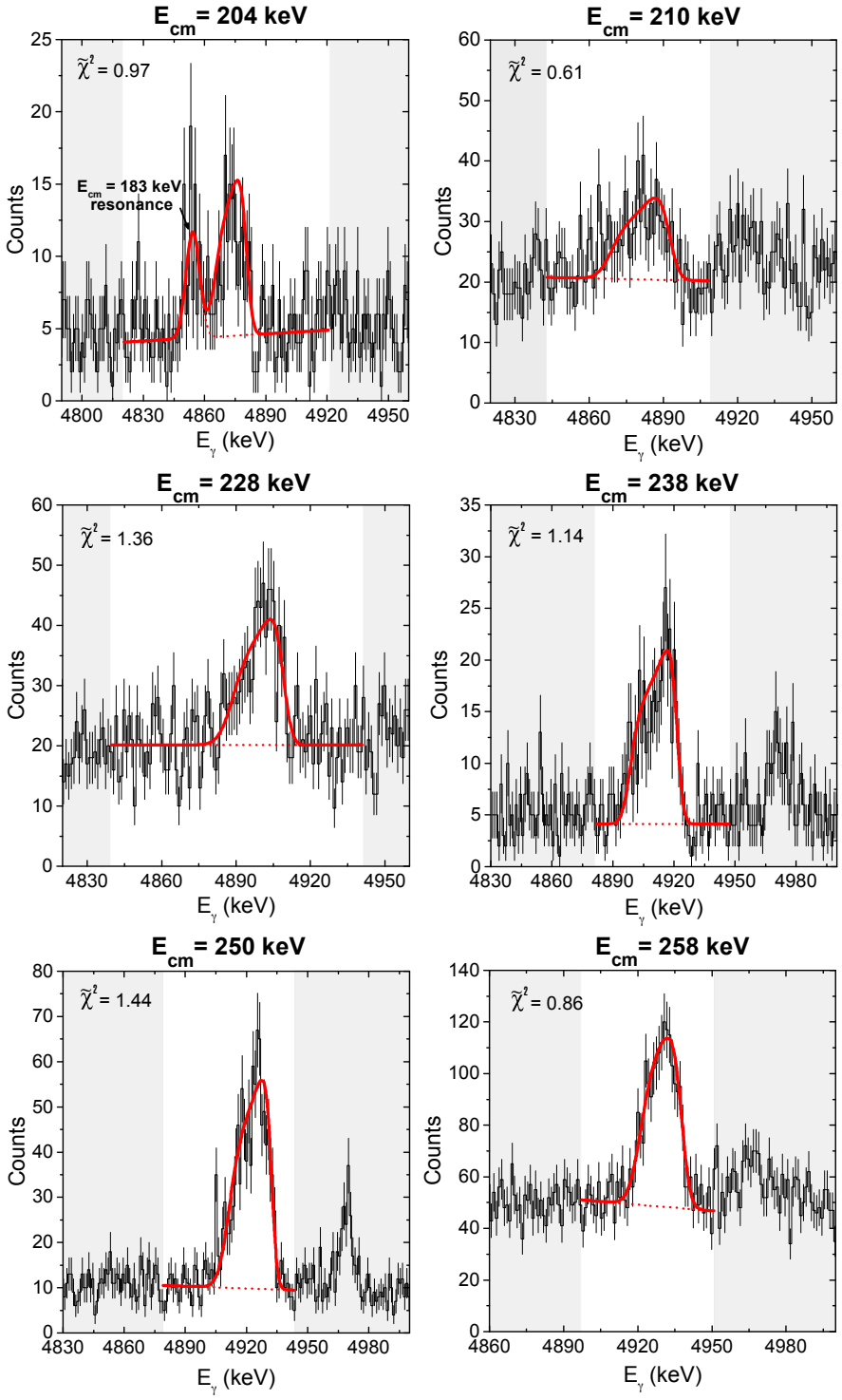

Figure 6.11: Peak-shape fits for the R/DC→937 keV primary transition, measured at energies between E_{cm} = 204-258 keV. The reduced chi-squared value for each fit is shown. A peak associated with the E_{R} = 183 keV resonance is visible at energies around E_{γ} = 4850 keV in the lowest energy measurement (E_{cm} = 204 keV).

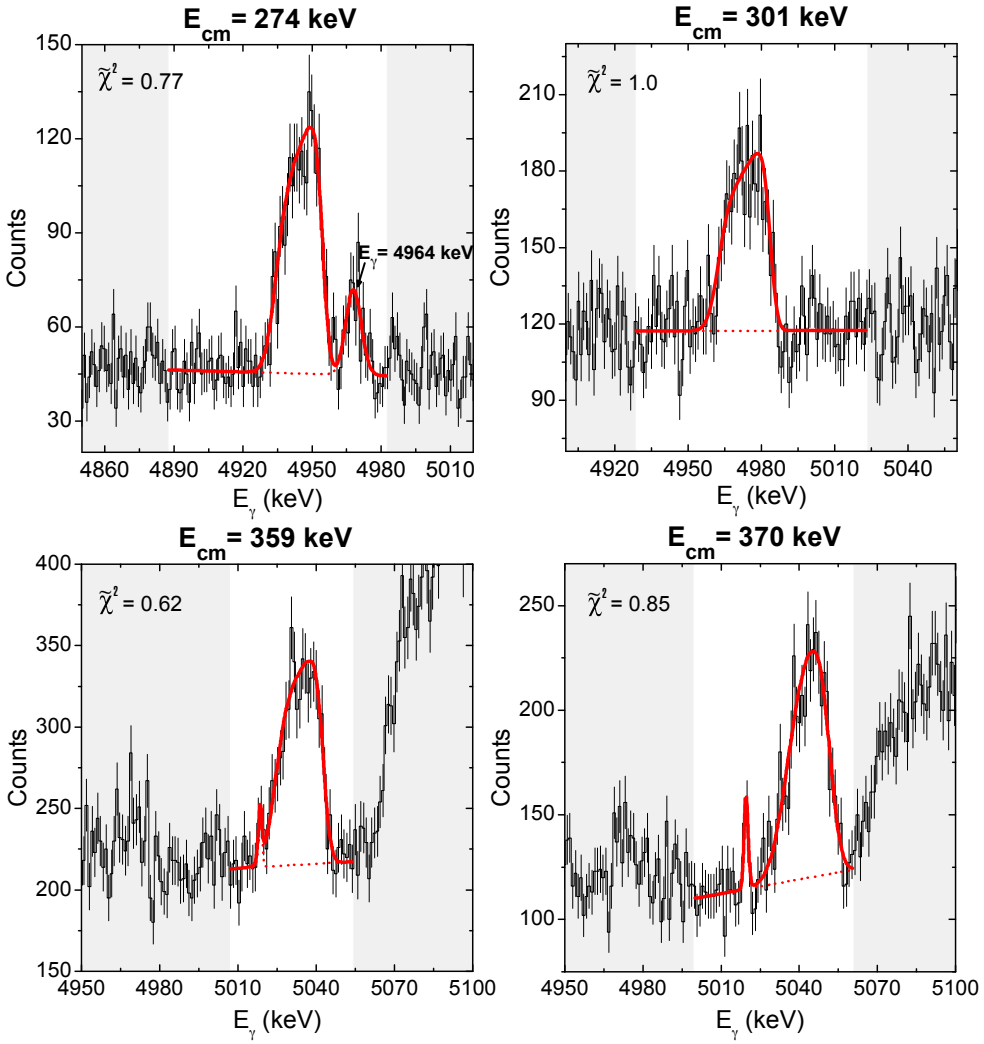

Figure 6.12: Primary peak-shape fits for the R/DC→937 keV transition, measured at energies between E_{cm} = 274-370 keV. The reduced chi-squared value for each fit is shown. The peak labeled as E_γ = 4964 keV corresponds to a secondary ^{18}F transition, while the background peak at approximately E_γ = 5020 keV in the two lower panels is of unknown origin.

The γ rays associated with the transitions R/DC→3791, R/DC→4116 and R/DC→4652 were often hampered by natural and beam-induced background. It was therefore decided to determine the S-factor for these transitions using results obtained from the secondary transition analysis (Section 6.6). The E_x = 3791 keV state (fed by the R/DC→3791 transition) decays to both the E_x = 3061 and 2100 keV levels with the emission of γ rays of energy E_γ = 730 and E_γ = 1691 keV, respectively (Figure 6.9). Taking into account the measured S-factor and branching ratios (reported in [29]) for these two secondary transitions - which are unique to the E_x = 3791 keV state - allows the S-factor for the R/DC→3791 transition to be determined. Similarly, the S-factor for the R/DC→4116 and R/DC→4652 keV transitions can be estimated from analysing the E_γ = 1054 keV and E_γ = 3531 keV γ rays associated with the E_x = 4116→3061 and E_x = 4652→1121 keV transitions in ^{18}F. For transitions where the primary S-factor has been obtained by analysing the secondary transitions as described above, the results for measurement energies where both primary and secondary analyses could be performed agree within uncertainties.

For the $E_{\rm cm}$ = 301 keV measurement, the peak associated with the R/DC→937 keV primary transition overlapped with that of the E_γ = 4964 keV secondary transition. Therefore a correction of approximately 12% (estimated from measurements of the E_γ = 4964 keV secondary transition performed at similar energies) was applied to the total primary S-factor for the $E_{\rm cm}$ = 301 keV measurement.

Special attention was required in order to analyse the spectrum taken at the lowest measured energy of $E_{\rm cm}$ = 204 keV. For this measurement, the $E_{\rm R}$ = 183 keV resonance was partially populated at energies corresponding to the back of the target, *i.e.* on the high energy tail of the target profile. It was possible to resolve the non-resonant and resonant contributions (as seen in Figure 6.11) for each of the affected transitions by directly fitting each component. The resonant contribution was fitted using a completely unconstrained Gaussian peak. Only primary transitions to the E_x = 937, 2523 and 3791 keV states suffered from this issue since the $E_{\rm R}$ = 183 keV resonance is not observed to decay to states associated with the other transitions appearing in Table 6.4. The measurement of the $E_{\rm R}$ = 183 keV resonance strength is discussed in Section 6.8.

At the lowest measured energy, $E_{\rm cm}$ = 167 keV, it was only possible to observe

the R/DC→937 transition. The relatively large uncertainty (approximately 40%) associated with the corresponding S-factor led to the exclusion of this result in all further analysis.

All values appearing in Table 6.4 have been corrected for true coincident summing effects. The magnitude of these corrections are presented in Table 6.5 and varied depending on the complexity of the γ-ray cascades involved.

Table 6.5: Percentage correction applied to the S-factor determined for each primary transition (Table 6.4) due to summing-out.

Transition	Summing-out Correction (%)
R/DC → 937	19.6
R/DC → 1120	47.1
R/DC → 2523	23.4
R/DC → 3061	32.8
R/DC → 3791	51.0
R/DC → 3839	37.6
R/DC → 4116	45.9
R/DC → 4652	50.8
R/DC → 4964	17.0

Angular distribution effects on the observed γ-ray yield have been estimated for the most intense primary transition (R/DC→937 keV). The theoretical angular distribution was calculated for the two possible entrance channel spins ($J^\pi = 2^+,3^+$) of the ^{17}O(p,γ)^{18}F reaction in the work of Fox *et al.* [33]. For a pure E1 transition:

$$W^{J=2}_{R/DC\rightarrow 937}(E1) = 1 + 0.1P_2(cos(\theta))$$
$$W^{J=3}_{R/DC\rightarrow 937}(E1) = 1 - 0.0285P_2(cos(\theta))$$

where P_2 is the second order Legendre polynomial, given by:

$$P_2(cos(\theta)) = \frac{1}{2}(3(cos(\theta))^2 - 1)$$

For a detector at $\theta = 55^\circ$ the term $P_2(\cos(\theta))$ is equal to zero, resulting in an isotropic distribution. However, since the angle subtended by our HPGe detector is non-negligible in close geometry (positioned 1.5 cm from the target surface), it

was necessary to verify that no angular distribution effects are present in our data. This was achieved using a Geant4 [69] simulation (implemented by F. Strieder [70]), which accurately modelled the geometry of our experimental setup. No effects from angular distributions were observed above the statistical accuracy of our measurements.

6.6 Secondary transitions analysis and results

As explained in Chapter 4, identification of the secondary transitions involved in the decay cascade to the ground state of ^{18}F makes it possible to obtain a second determination of the total S-factor, independently from the analysis of the primary transitions. A program I have written using the data analysis environment, ROOT [68], was used to fit the Gaussian peak associated with each observed secondary transition. A time normalised background spectrum was subtracted from certain runs in order to remove natural background lines in the vicinity of the signal peak. Any remaining background was modelled using a function consisting of a linear component and one or more additional Gaussian peaks where necessary.

The counts associated with each secondary transition are given by the difference in the integrals of the total (signal + background) and background functions in the region of interest defined by the signal peak. The corresponding uncertainty was determined using ROOT's *IntegralError* routine [68], which estimates the uncertainty on the integral directly from the fit parameters. For particularly weak transitions the peak area was occasionally determined directly from integrating the total number of counts instead of fitting a Gaussian peak. Following the thick-target yield formalism (Chapter 4), the S-factor, $S(E_{\text{eff}})$, is calculated from the reaction yield, Y, applying Equation 4.9:

$$Y = \frac{S(E_{\text{eff}})}{\epsilon(E_0)} \int_{E_0-\Delta E}^{E_0} \frac{1}{E} e^{-2\pi\eta(E)} dE \tag{6.8}$$

where $\epsilon(E_0)$ is the effective stopping power and $\eta(E)$ is the full-energy peak efficiency. The initial beam energy is given by E_0 and ΔE represents the target thickness (in energy units).

True coincidence summing corrections were calculated using Equations 4.18 and 4.19, taking into account the full γ-decay cascade relevant to a given

transition. The primary branching ratios measured in the present study were used in this calculation while all secondary branching ratios were adopted from [29].

A total of sixteen secondary γ-ray transitions between the various states in ^{18}F have been identified and analysed. The results of this analysis are presented in Table 6.6. Once again, all values are determined directly from measured yields with any missing entries (required to calculate $S_{\rm tot}$) estimated from the results obtained at similar measurement energies. As an example, all secondary transition peaks observed at a measurement energy of $E_{\rm cm} = 370$ keV are shown in Figures 6.13-6.15.

The 937→0 keV transition is by far the strongest one observed, occurring in approximately 71% of all reactions. This indicates that the majority of decays to the ground state of ^{18}F take place via the 937 keV level. The peak from this transition partially overlapped with a background line at $E_\gamma = 934$ keV. A time-normalised background spectrum was subtracted in order to remove this background contribution, which constituted approximately 6% of the total yield for the $E_\gamma = 937$ keV peak.

In contrast to the primary transition analysis, it was impossible to disentangle the $E_{\rm R} = 183$ keV resonance contribution to secondary transitions measured at $E_{\rm cm} = 204$ keV. As explained in Chapter 4, this is because all counts from a secondary transition are distributed in a peak, whose shape is insensitive to how the parent state was populated, *e.g.* via the resonant or non-resonant process.

Only the most intense transition (937→0 keV) was observed at the lowest measured energy of $E_{\rm cm} = 167$ keV. In this case, the total S-factor was estimated from the measured 937→0 branching ratio of 71%.

The total non-resonant S-factor, $S_{\rm tot}$, is calculated from summing only the transitions proceeding to the ground state of ^{18}F. These values are directly comparable to the results obtained in the primary transition analysis (Table 6.4).

6.7 Total S-factor

The total S-factors measured in both the primary and secondary analyses are presented in Figure 6.16. The error bars include both statistical and target thickness uncertainties. Although the results obtained from the secondary

Table 6.6: Secondary transition S-factor results in units of keV barn. The numbers in parentheses in the header row indicate the transition energy in keV. S_{tot} is given by the sum of only the transitions proceeding to the ^{18}F ground state. Where information for a given transition is not listed, the S-factor value used to calculate S_{tot} was estimated by interpolating the results obtained at similar measurement energies. The uncertainty (in brackets) in S_{tot} includes both statistical and target thickness uncertainties.

	$937 \to 0$	$1080 \to 0$	$1121 \to 937$	$2100 \to 0$	$2100 \to 937$	$2100 \to 1080$	$2523 \to 0$	$3061 \to 0$	$3061 \to 937$
E_{cm} [keV]	(937)	(1080)	(184)	(2100)	(1164)	(1020)	(2523)	(3061)	(2125)
167	2.8(4)	–	–	–	–	–	–	–	–
210	3.9(2)	0.23(12)	0.8(3)	0.11(8)	0.35(19)	–	0.16(9)	0.54(15)	1.1(2)
228	3.83(12)	0.15(5)	0.82(18)	0.12(6)	–	0.10(7)	0.22(7)	0.35(8)	1.26(19)
238	3.76(14)	0.05(4)	0.8(2)	0.12(6)	0.17(9)	0.10(7)	0.06(3)	0.20(5)	1.30(13)
250	4.26(7)	0.04(2)	0.90(9)	0.11(4)	–	0.07(4)	0.14(3)	0.37(4)	1.30(8)
258	4.10(9)	0.09(4)	0.80(11)	0.09(5)	0.26(6)	0.08(5)	0.14(3)	0.42(5)	1.31(9)
274	4.18(6)	0.05(3)	0.83(8)	–	0.11(5)	0.10(5)	0.13(3)	0.36(4)	1.39(8)
301	5.31(10)	0.10(4)	0.72(13)	–	0.14(9)	0.24(7)	0.18(4)	0.49(8)	1.71(10)
359	6.44(8)	0.08(3)	0.90(12)	0.16(6)	0.19(8)	0.18(6)	0.24(4)	0.58(8)	–
370	6.37(10)	0.09(3)	0.99(12)	0.07(4)	0.14(5)	0.10(5)	0.16(4)	0.60(9)	1.69(16)

	$3791 \to 2100$	$3791 \to 3061$	$3839 \to 0$	$3839 \to 3061$	$4116 \to 3061$	$4652 \to 1121$	$4964 \to 0$	S_{tot}
E_{cm} [keV]	(1691)	(730)	(3839)	(777)	(1054)	(3531)	(4964)	
167	–	–	–	–	–	–	–	3.9(6)
210	–	–	0.5(3)	0.57(19)	0.49(12)	–	–	5.6(5)
228	0.10(8)	0.14(7)	0.41(18)	0.67(14)	0.57(9)	–	0.22(9)	5.3(4)
238	–	0.17(11)	0.35(8)	0.63(9)	0.43(10)	0.06(4)	0.44(9)	5.0(3)
250	–	–	0.35(5)	0.64(5)	0.53(5)	–	–	5.6(4)
258	0.34(6)	0.13(9)	0.36(6)	0.50(6)	0.67(8)	–	0.31(8)	5.5(3)
274	0.21(4)	0.14(5)	0.31(5)	0.72(6)	0.52(5)	0.07(3)	0.29(7)	5.4(3)
301	0.15(6)	0.18(11)	0.50(13)	0.90(7)	0.73(8)	0.13(7)	–	7.1(5)
359	0.21(6)	0.19(9)	0.46(9)	1.16(7)	0.66(6)	–	0.47(11)	8.4(4)
370	0.34(6)	0.21(6)	0.71(10)	1.09(7)	0.66(6)	0.09(4)	0.47(16)	8.5(5)

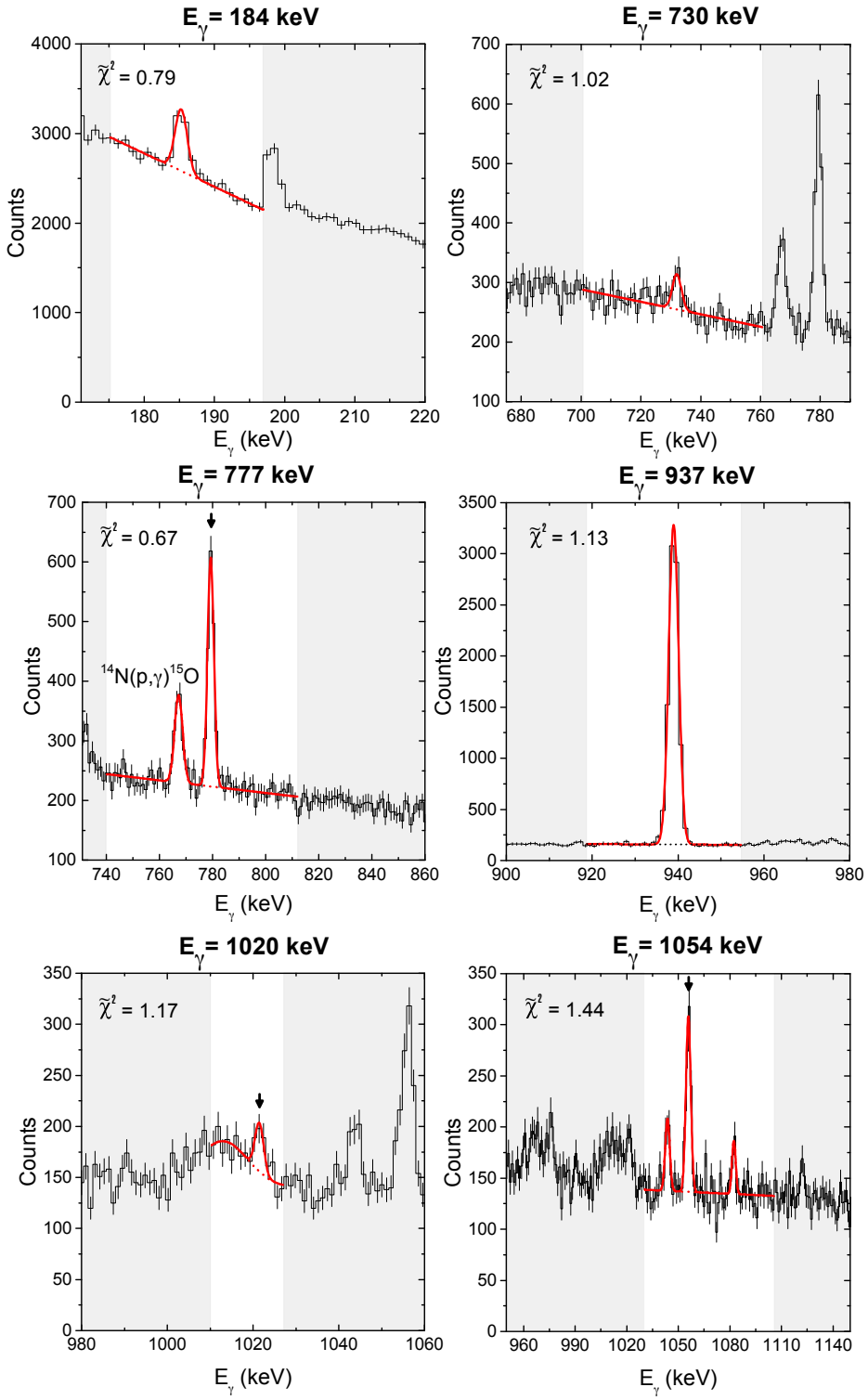

Figure 6.13: Fits to secondary transitions between E_γ = 184-1054 keV, observed at the highest measurement energy of E_{cm} = 370 keV. An arrow identifies the signal peak in spectra where background peaks are also present. The reduced chi-squared value for each fit is shown.

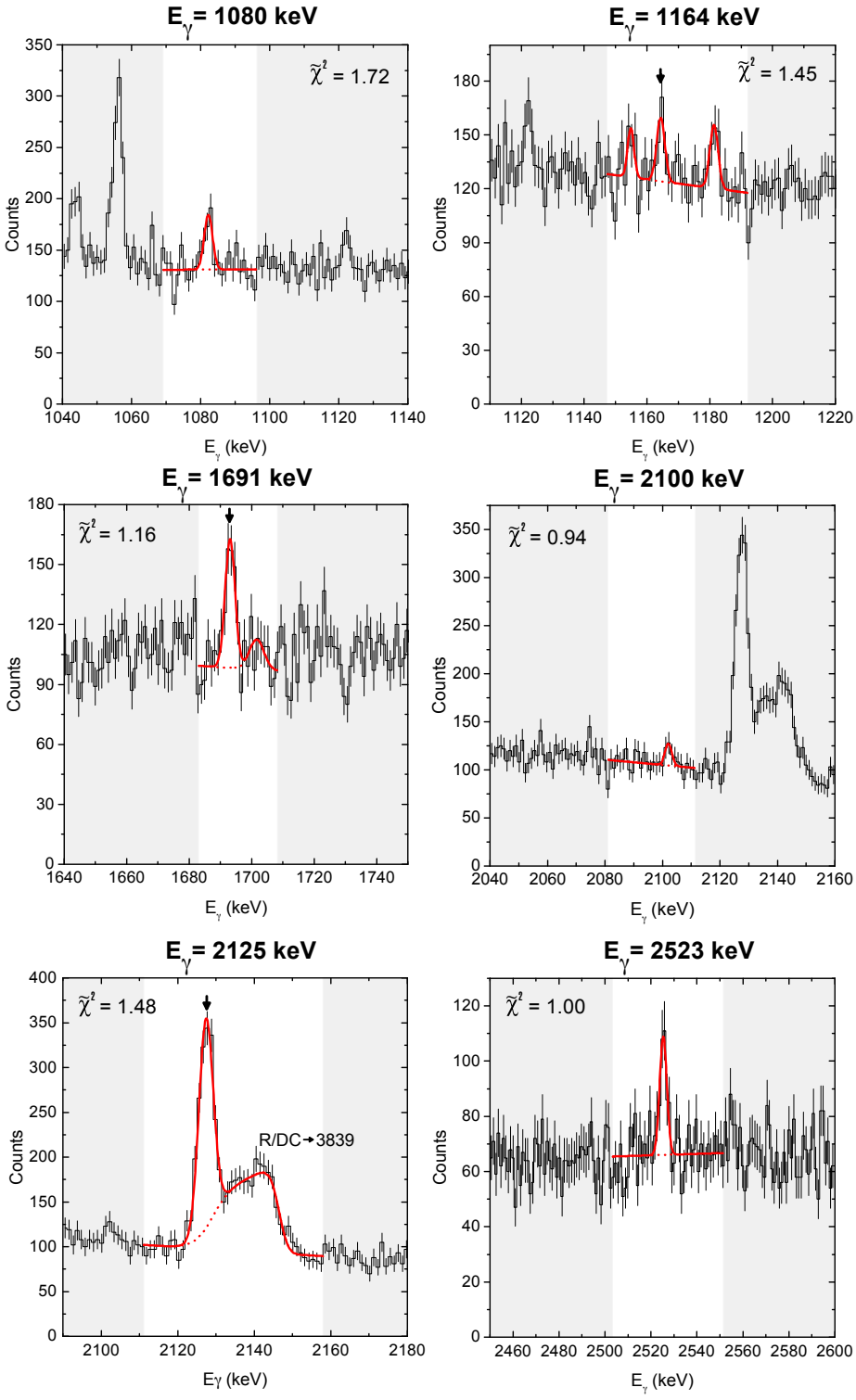

Figure 6.14: Fits to secondary transitions between E_γ = 1080-2523 keV, observed at the highest measurement energy of $E_{\rm cm}$ = 370 keV. An arrow identifies the signal peak in spectra where background peaks are also present. The reduced chi-squared value for each fit is shown.

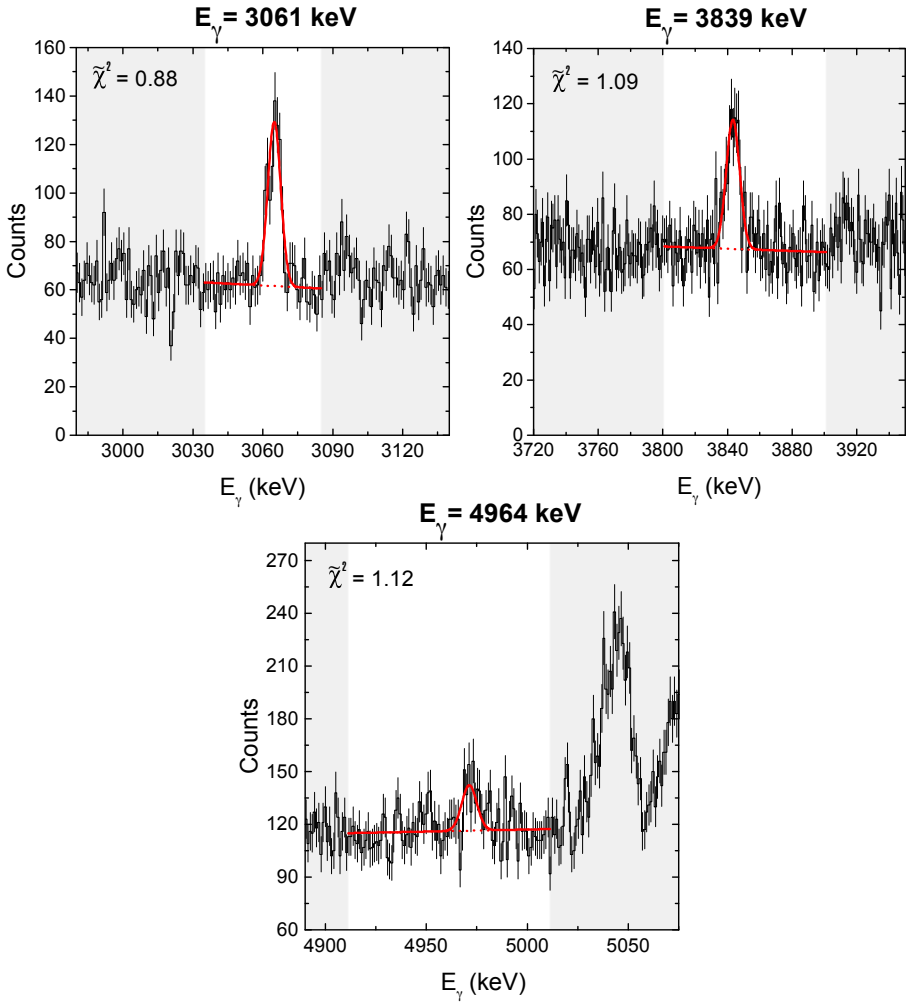

Figure 6.15: Fits to secondary transitions between E_γ = 3061-4964 keV, observed at the highest measurement energy of E_{cm} = 370 keV. The reduced chi-squared value for each fit is shown.

transition analysis appear to be systematically lower than the primary S-factor values, the agreement is generally within 10%. The discrepancy is possibly due to the presence of one or more weak, unobserved (and therefore unaccounted for) secondary transitions. This explanation seems plausible given the complex nature of the γ-ray cascade to the ground state of ^{18}F. As such, the secondary transitions only provide a lower limit to the S-factor and were excluded from further analysis, and from the calculation of the total reaction rate (Section 6.9).

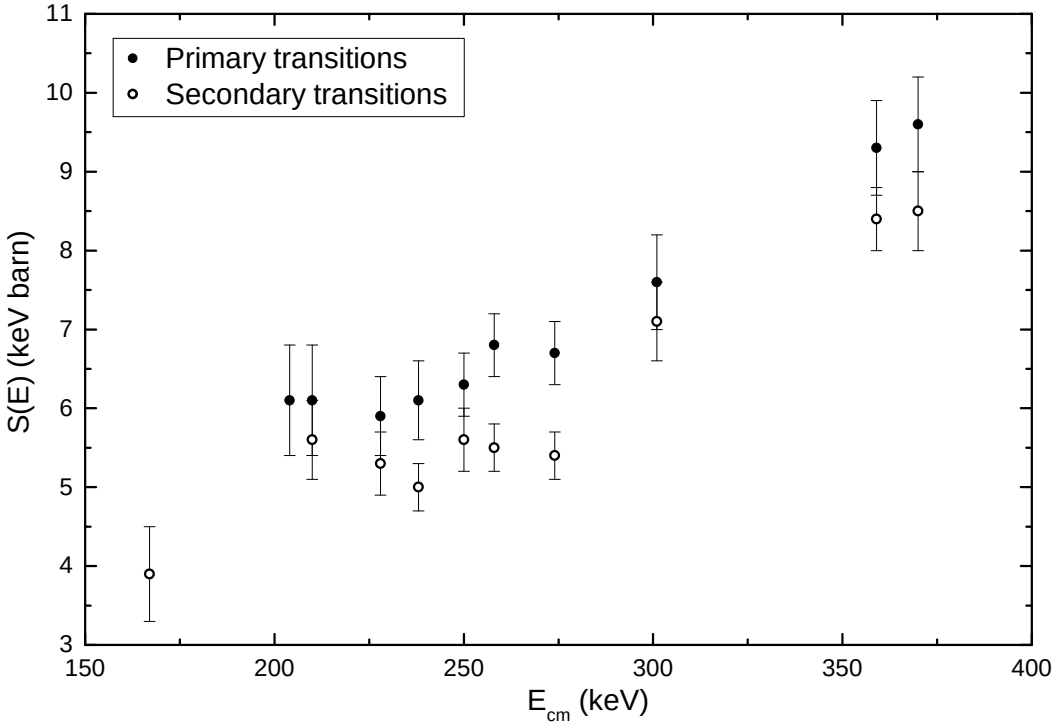

Figure 6.16: S-factor for the ^{17}O(p,γ)^{18}F reaction measured from analysing primary (solid symbols) and secondary (open symbols) γ-ray transitions. The small (approximately 10%) systematic discrepancy between each set of results is possibly due to one or more weak, un-observed (and therefore unaccounted for), secondary transitions.

The primary transition results plotted in Figure 6.16 have been used to determine the energy dependence of the total S-factor in the energy range $E_{\rm cm}$ = 204-370 keV. In order to fit the DC component of the total S-factor, the DC energy dependence found by Fox *et al.* [33] was multiplied by a pre-factor, $C_{\rm DC}$, leading to the expression:

$$S_{DC}(E) = C_{DC}(3.74 + 6.76 \times 10^{-4}E - 2.5 \times 10^{-7}E^2) \quad (6.9)$$

where, E is given in keV and $S_{\rm DC}$ in keV b.

The contributions to the total S-factor from the broad resonances at $E_{\rm R}$ = 556 and 677 keV were determined using Equation 2.26 and the gamma widths obtained in the most recent study of Kontos *et al.* (Table 6.3).

The fit to the total S-factor is shown Figure 6.17, where the broad resonant and DC contributions are plotted using dashed and dot-dashed lines, respectively. The contribution from the tails of the broad resonances amounts to between 20-45% of the total S-factor at energies between $E_{\rm cm}$ = 204-370 keV. The $E_{\rm R}$ = 557 keV resonance accounts for approximately 85% of the total broad resonant S-factor inside the aforementioned energy range (the $E_{\rm R}$ = 677 keV broad resonance accounts for the remaining 15%).

The uncertainty associated with the broad resonance contributions was estimated using a Monte Carlo approach, whereby the relevant partial widths are randomly sampled from a Gaussian distribution with sigma values equal to the quoted uncertainty. Performing this procedure simultaneously for the partial widths presented in Table 6.3 and then plotting the resultant spread of broad resonance S-factor values (for a given energy) leads to a distribution of width approximating the overall broad resonance S-factor uncertainty. On average, this uncertainty was approximately 11% in the energy range $E_{\rm cm}$ = 204-370 keV. This translates into an additional uncertainty on the total S-factor of about 2-5%.

The zero-energy-extrapolation of the total S-factor (Figure 6.17) gives:

$$\mathrm{S}(0) = 5.3 \pm 0.5 \text{ keV b}$$

where the uncertainty was calculated by summing in quadrature the statistical uncertainty (approximately 3%), the systematic uncertainties (Table 6.7) and the uncertainty associated with the broad resonance contribution. The systematic uncertainties quoted in Table 6.7 were calculated as follows. The uncertainty on the full-energy peak efficiency was estimated as described in Section 6.2 while the uncertainty on the stopping power was approximately 4% [47]. The 3% uncertainty on the charge integration is a conservative estimate given the reproducibility of the focusing of the proton beam on the target surface. The true coincidence summing uncertainty was estimated directly from Equations

4.18 and 4.19, propagating the uncertainty associated with the efficiency and branching ratios. The uncertainty on the stoichometry and ^{17}O abundance of our Ta_2O_5 targets was determined from the *Secondary Ion Mass Spectrometry* (SIMS) and *Rutherford Backscattering* (RBS) analysis described in Appendix B.

S-factor fits were also performed individually for each of the primary transitions using the broad resonance branching ratios to the various states in ^{18}F given in Kontos *et al.* [43]. The total S-factor fit for the R/DC→937 transition is shown in Figure 6.18, while the fits for all remaining primary transitions are presented in Figure 6.19. Data points shown in grey represent estimated values based on measurements performed at nearby energies and are not included in the fit.

Table 6.7: Systematic uncertainties (percentage) for the present measurements of the ^{17}O(p,γ)^{18}F reaction.

	Systematic Uncertainty
Full-energy peak Efficiency	5%
Stopping Power	4%
Charge Integration	3%
Stochiometry	3%
^{17}O Abundance	3%
Coincidence Summing	2%

6.8 The E_R = 183 keV resonance strength

Prior to this investigation of the E_R = 183 keV resonance, the corresponding state in ^{18}F (E_x = 5790 keV) had only been observed to decay via the two strongest transitions through the levels at E_x = 937 keV and E_x = 1080 keV [33]. The high level of sensitivity achieved in our study has led to the identification of several additional transitions from this state, presumably too weak to have been observed previously.

The strength of the E_R = 183 keV resonance has been determined by measuring the γ-ray yield associated with the transitions involved in the decay cascade of the corresponding E_x = 5790 keV state in ^{18}F. As was the case for the non-resonant S-factor measurements described in the previous sections, both

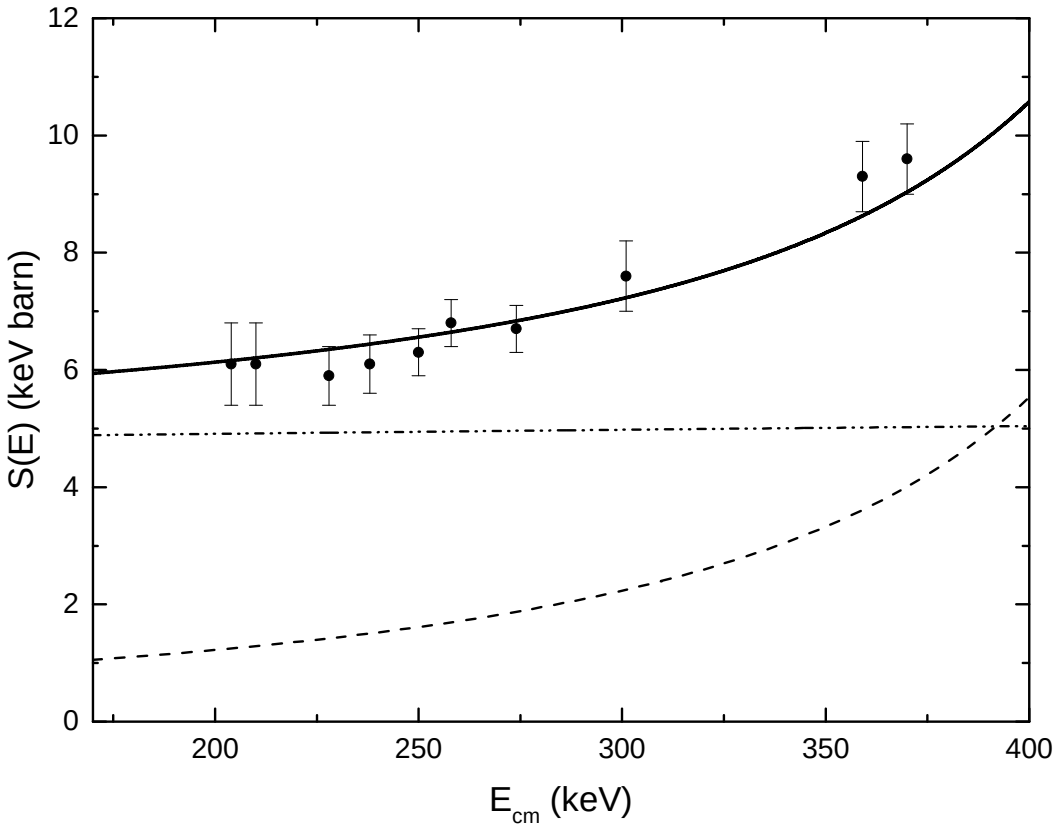

Figure 6.17: Fit (solid line) to the total S-factor results obtained in the present investigation of the $^{17}O(p,\gamma)^{18}F$ reaction. The dot-dashed and dashed lines represent the contributions from the direct capture (DC) process and the tails of the broad resonances at E_R = 556 and 677 keV, respectively.

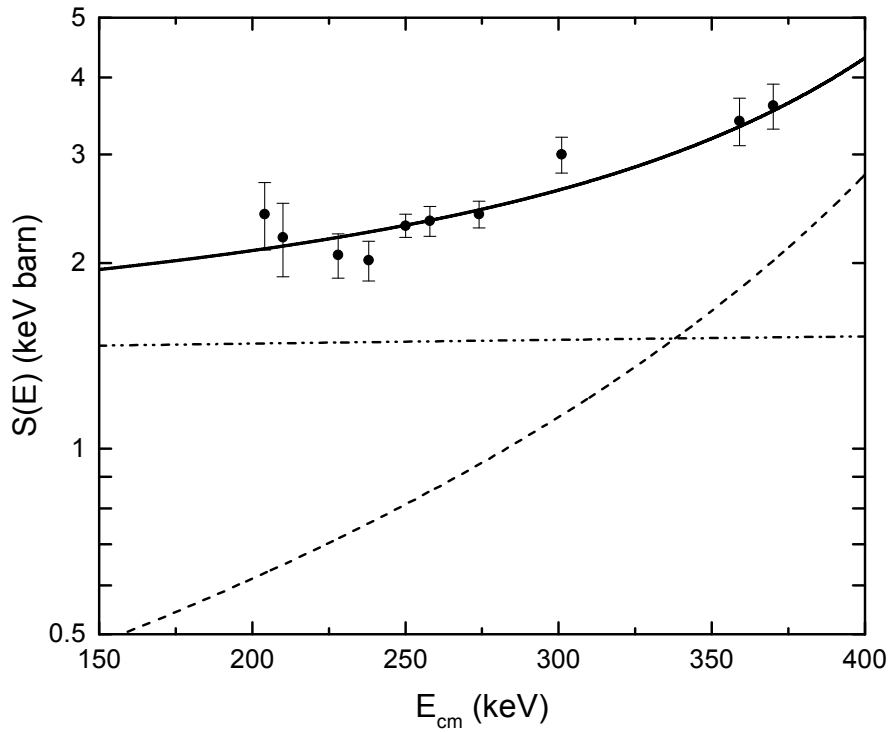

Figure 6.18: S-factor fit (solid line) for the R/DC→937 keV primary transition. The dot-dashed and dashed lines represent the contributions from the direct capture (DC) and the tails of the broad resonances at $E_{\mathrm{R}} = 556$ and 677 keV, respectively.

primary and secondary transitions were analysed. Figure 6.20 shows the γ-ray peaks associated with the formation and decay of the $E_{\mathrm{x}} = 937$ keV and $E_{\mathrm{x}} = 1080$ keV states populated by the $E_{\mathrm{R}} = 183$ keV resonance.

A number of states populated in the decay of the $E_x = 5790$ keV state are also fed by non-resonant processes. In order to extract the purely resonant component of the yield for a given transition, the non-resonant S-factor measured in the present study (Figures 6.18 and 6.19) was extrapolated down to the $E_{\mathrm{R}} = 183$ keV resonance energy. This allowed the expected non-resonant contribution to be subtracted from the total yield on a transition-by-transition basis.

For the strongest on-resonance transition, $E_\gamma = 1080$ keV, the non-resonant contribution was negligible while in the case of the second strongest transition, $E_\gamma = 937$ keV, the non-resonant contribution was at the level of approximately 25%.

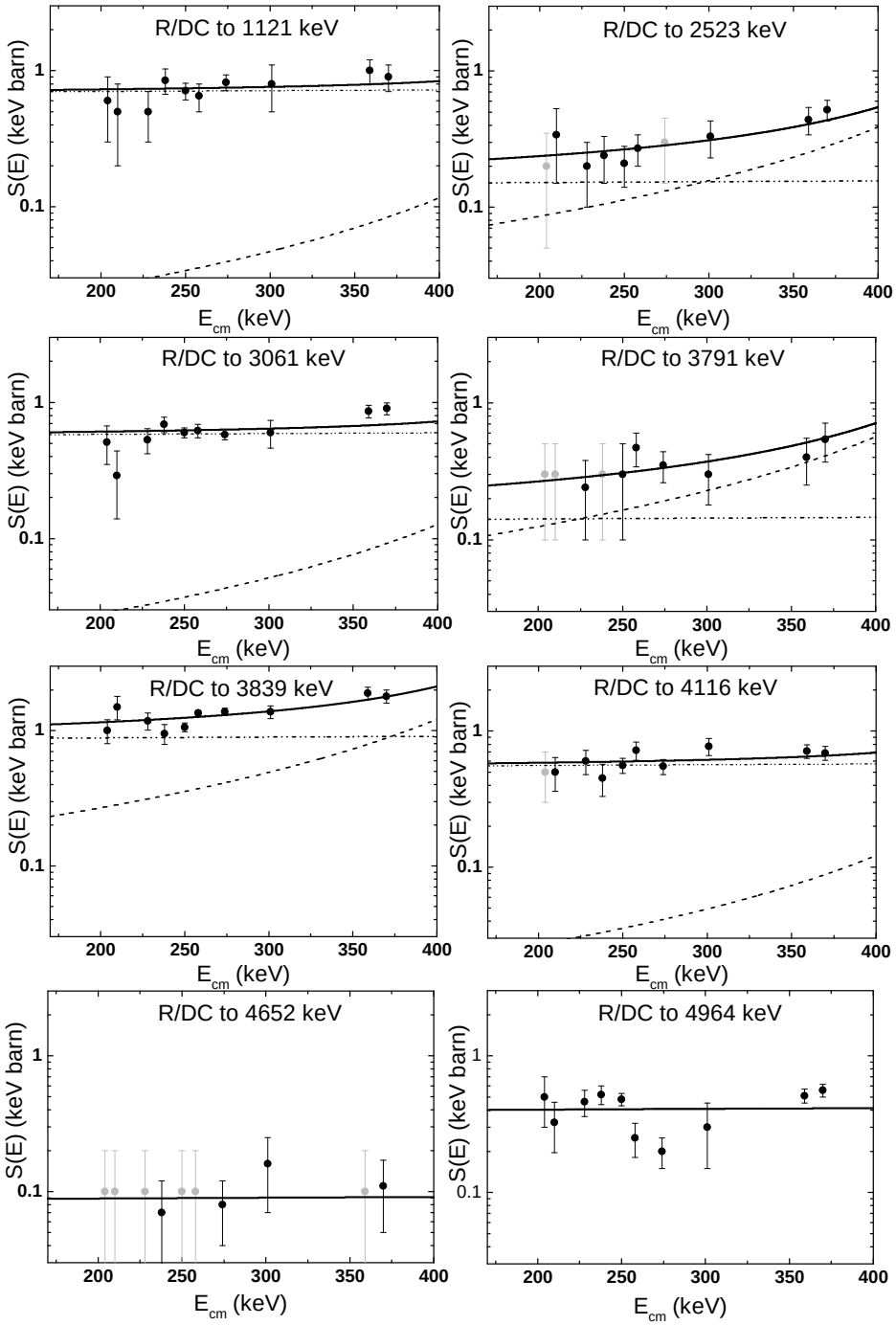

Figure 6.19: S-factor fits (solid lines) for all primary transitions (apart from R/DC→937, which is shown in Figure 6.18) observed in the present study of the ^{17}O(p,γ)^{18}F reaction. The dot-dashed and dashed lines represent the contributions from the direct capture (DC) and the tails of the broad resonances at $E_{\rm R}$ = 556 and 677 keV, respectively. Data points shown in grey represent estimated values based on measurements performed at nearby energies and are not considered in the fits.

The analysis of the R→2101 keV transition (E_γ = 3689 keV) was complicated by its overlapping with the second-escape peak of the stronger R→1080 keV transition (E_γ = 4710 keV). The contribution of the second-escape peak to the total number of peak counts was estimated and subsequently subtracted using the ratio of the relative intensity between full-energy, first- and second-escape peaks for the nearby 3908→0 transition from the ^{18}O(p,γ)^{19}F reaction.

The method used to determine the strength of the E_{R} = 183 keV resonance involves calculating the expected number of counts for each transition using a modified version of Equation 4.13:

$$N_{R,i} = N_p \frac{\lambda_R^2}{2} \omega\gamma \frac{b_{R,i}\eta(E_i)}{\epsilon(E_R)} + N_{\text{sum-in}} - N_{\text{sum-out}} \tag{6.10}$$

where $N_{\mathrm{R,i}}$ is the theoretical number of counts expected from the i-th transition and N_{p} is the number of incident protons. The full-energy peak efficiency is denoted by $\eta(E_i)$, λ_{R} is the de Broglie wavelength at the resonance energy, E_{R}, and $b_{\mathrm{R,i}}$ is the relevant branching ratio. The number of counts expected due to summing-in and summing-out are represented by $N_{\text{sum-in}}$ and $N_{\text{sum-out}}$, respectively. The magnitude of the summing corrections were calculated by applying Equations 4.18 and 4.19.

In order to determine the unknown quantities (resonance strength and branching ratios) in Equation 6.10, a simultaneous χ^2 fit was performed to the experimentally measured yield for each transition. The resonance strength value and branching ratios were simultaneously free to vary so that the resultant values were those which most accurately describe the experimentally acquired data.

This approach was first applied to yields obtained from a spectrum produced by summing several relatively long on-resonance measurements (corresponding to approximately 90C of accumulated charge). Combing several runs maximises the statistical accuracy of the data, which is particularly important in constraining the branching ratios (and hence the true coincidence summing corrections) for relatively weak ^{18}F transitions. Several of the spectra included in this sum were obtained using targets previously exposed to relatively large values (greater than 20C) of accumulated charge. As a consequence, some of the profile scans associated with these targets displayed signs of degradation due to the sputtering processes described in Section 6.1. In the absence of accurate information concerning the remaining ^{17}O abundance of these deteriorated targets, the

absolute value of the E_R = 183 keV resonance strength could not be determined from these data[2]. The branching ratios determined for all of the primary transitions from the E_R = 183 keV resonance measured in this work are listed in Table 6.8.

Transition	Branching Ratio (%)
$R \rightarrow 0$	2.9 ± 0.4
$R \rightarrow 937$	24.5 ± 0.8
$R \rightarrow 1041$	3.4 ± 0.4
$R \rightarrow 1080$	40.8 ± 0.7
$R \rightarrow 2101$	11.8 ± 0.8
$R \rightarrow 2523$	5.5 ± 0.6
$R \rightarrow 3134$	4.3 ± 0.4
$R \rightarrow 3358$	2.3 ± 0.3
$R \rightarrow 3791$	4.5 ± 0.4

Table 6.8: Branching ratios for all observed primary transitions from the E_R = 183 keV resonance. The statistical uncertainties are calculated as described in the text.

For the purpose of calculating the absolute resonance strength, a single on-resonance run was acquired using a fresh target (target 28) of known ^{17}O enrichment. A second χ^2 fit was then performed, where the branching ratios were fixed to their previously determined values. This method benefits from precise branching ratio information obtained from long measurements of low statistical uncertainty, without sacrificing the accuracy of the absolute determination of the resonance strength due to target degradation.

The statistical uncertainties on the resonance strength and on the branching ratios were estimated by varying their original values and re-minimising with all other parameters free until a point where the condition $\chi^2 = \chi^2_{\text{original}} + 1$ was satisfied (equivalent to one standard deviation).

The resonance strength was determined as:

$$\omega\gamma = (1.70 \pm 0.15) \times 10^{-6} \text{ eV}$$

The quoted uncertainty on this value was calculated by summing in quadra-

[2]The ^{17}O abundance has no influence on the relative yield of each γ-ray transition, allowing the branching ratios to be inferred by performing a χ^2 fit to the summed spectrum as described above.

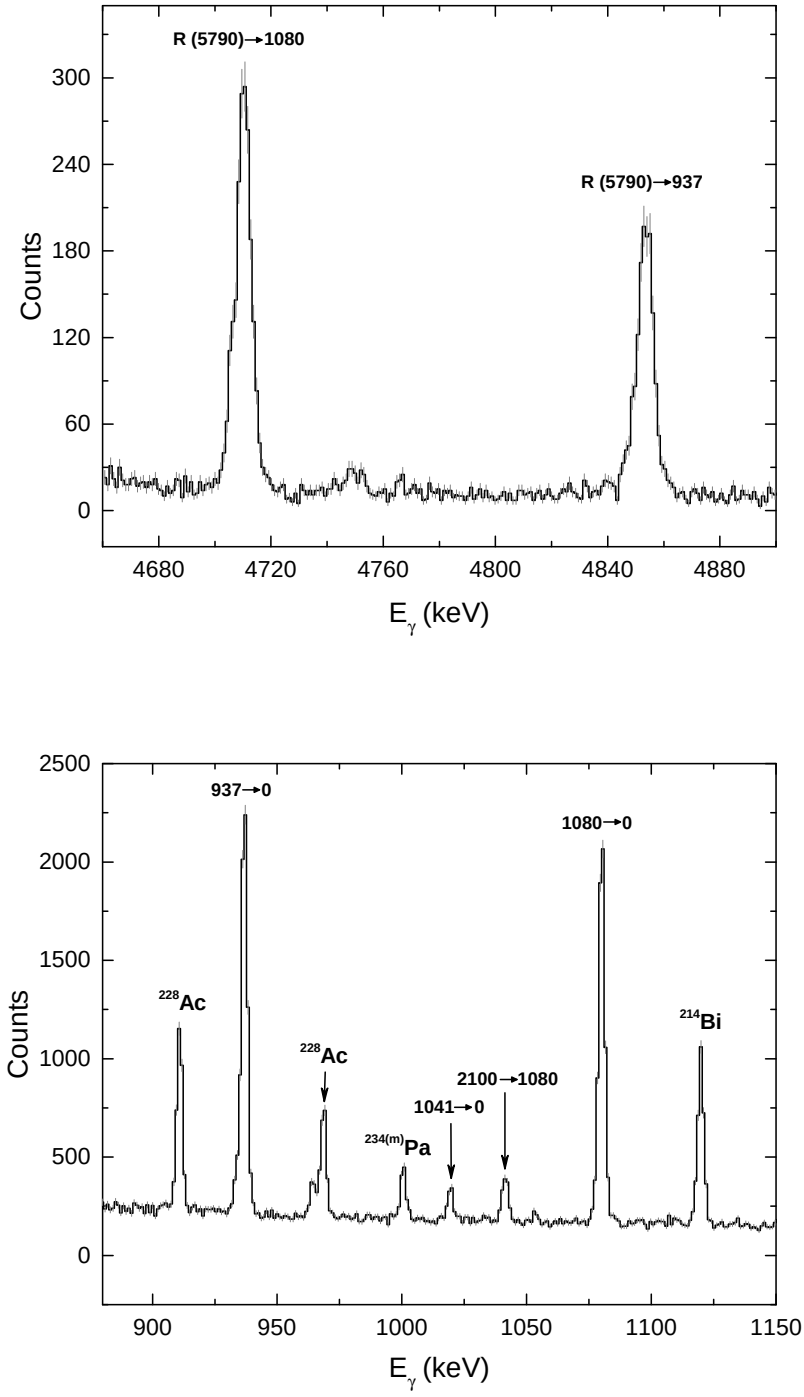

Figure 6.20: On-resonance spectra acquired at the E_R = 183 keV resonance. The upper spectrum shows the γ-ray peaks associated with the two strongest primary transitions, while their corresponding secondary transitions are shown in the lower spectrum. Several natural background lines are also indicated.

ture the systematic uncertainties listed in Table 6.7 with the statistical uncertainty of approximately 3%.

The summing-out corrections for the three strongest primary and secondary transitions are listed in Table 6.9. The only significant correction due to summing-in occurred for the R→0 keV transition, where approximately 52% of the observed yield was attributed to this effect.

In order to verify that the global fit performed to determine the resonance strength is not sensitive to the starting values of the free parameters (branching ratios and resonance strength), their initial values were adjusted within a (arbitrary) 20% limit and the fit re-performed. In all instances the fit converged to the same value for the resonance strength and branching ratios, demonstrating the robustness of the analysis procedure.

Table 6.9: Summing-out corrections for the three most intense primary and secondary transitions from the $E_R = 183$ keV resonance.

Transition	Summing-out Correction (%)
R → 937	25.2
937 → 0	28.5
R → 1080	22.6
1080 → 0	32.0
R → 2100	60.0
2100 → 0	21.7

6.9 The $^{17}O(p,\gamma)^{18}F$ reaction rate

The $^{17}O(p,\gamma)^{18}F$ reaction rate has been determined from the S-factor and $E_R = 183$ keV resonance strength obtained in the present study. This calculation was performed using the *RatesMC* reaction rate code written by Richard Longland [71], based on a Monte Carlo technique. This approach involves associating each nuclear physics quantity, *e.g.* resonance energies and widths, to a suitable probability density function of width sigma reflecting the quoted uncertainty. The total reaction rate is then evaluated using values randomly sampled from these distributions. This allows the median reaction rate to be determined as well as upper and lower rate values corresponding to one standard deviation of

the resultant log-normal distribution. A detailed explanation of the RatesMC code can be found in [71].

Table 6.10: Resonance input parameters used to calculate the $^{17}O(p,\gamma)^{18}F$ reaction rate using the *RatesMC* [71] code.

E_R (keV)	$\omega\gamma$ (eV)	Γ_p (eV)	Γ_γ (eV)	Γ_α (eV)
-1.6	-	$(8.20 \pm 0.05)\times10^{-3}$	$(8.94 \pm 0.74)\times10^{-1}$	$(3.20 \pm 0.21)\times10^{1}$
-3.1	-	$(5.4 \pm 1.8)\times10^{-2}$	$(4.85 \pm 0.51)\times10^{-1}$	$(4.28 \pm 0.16)\times10^{1}$
65.1	-	$(1.90 \pm 0.32)\times10^{-8}$	$(4.4 \pm 0.2)\times10^{-1}$	$(1.30 \pm 0.05)\times10^{2}$
183.4	$(1.70 \pm 0.15)\times10^{-6}$	-	-	-
489.9	$(1.30 \pm 0.15)\times10^{-2}$	-	-	-
529.9	$(1.10 \pm 0.25)\times10^{-1}$	-	-	-
556.7	-	$(1.41 \pm 0.03)\times10^{4}$	$(6.32 \pm 0.85)\times10^{-1}$	8 ± 1
633.9	$(1.60 \pm 0.26)\times10^{-1}$	-	-	-
676.7	-	$(1.13 \pm 0.02)\times10^{4}$	1.41 ± 0.17	$(3.0 \pm 0.4)\times10^{1}$
704.0	$(3.20 \pm 0.7)\times10^{-2}$	-	-	-
779.0	-	$(1.09 \pm 0.11)\times10^{2}$	$(2.61 \pm 0.68)\times10^{-1}$	$(2.86 \pm 0.87)\times10^{2}$
878.4	$(1.80 \pm 0.7)\times10^{-2}$	-	-	-
1037.2	-	$(3.68 \pm 0.61)\times10^{2}$	$(8.4 \pm 2.0)\times10^{-1}$	$(2.31 \pm 0.4)\times10^{2}$
1170.5	$(1.40 \pm 0.28)\times10^{-1}$	-	-	-
1196.6	$(2.70 \pm 0.92)\times10^{-2}$	-	-	-
1270.8	$(5.0 \pm 1.9)\times10^{-2}$	-	-	-

Aside from the non-resonant, direct capture, S-factor contribution and the strength of the $E_{\mathrm{R}} = 183$ keV resonance measured in the present study, a number of additional resonances were included in the reaction rate calculation. The resonance energies, strengths and/or partial widths were taken from [72], which relies heavily on information obtained in [30], [36] and [33]. The values used for all resonances considered in calculating the total reaction rate are listed in Table 6.10. Interference effects between resonances of the same spin and parity are estimated by the RatesMC code using the formalism presented in [73].

The fractional contribution to the total reaction rate as a function of temperature is plotted for each component of the $^{17}O(p,\gamma)^{18}F$ reaction in Figure 6.21. It is perhaps surprising that despite the presence of the $E_{\mathrm{R}} = 183$ keV resonance, the reaction rate is dominated by the non-resonant direct capture (DC) mechanism inside the energy range (indicated on Figure 6.21) relevant for classical novae.

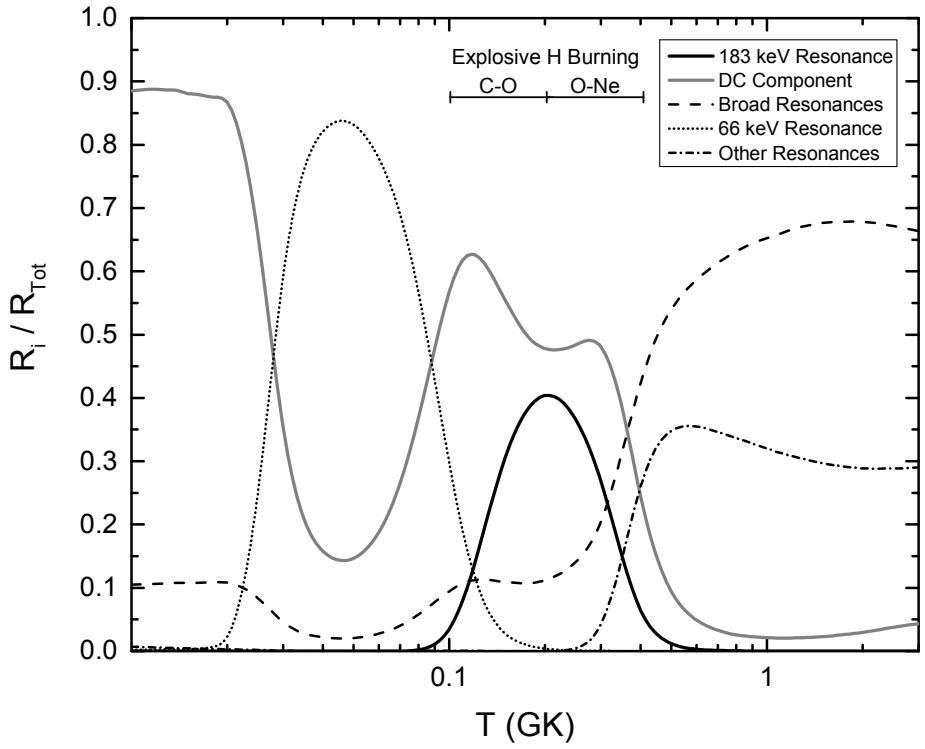

Figure 6.21: Fractional contributions to the total ^{17}O(p,γ)^{18}F reaction rate as a function of temperature. The $E_{\rm R}$ = 183 keV resonance and direct capture (DC) process dominate the reaction rate at the temperatures relevant for classical novae.

Table 6.11 presents the recommended ^{17}O(p,γ)^{18}F reaction rate from the current study. Upper and lower rates (corresponding to the 1σ level) are also provided.

Table 6.11: The $^{17}O(p,\gamma)^{18}F$ reaction rate in units of $cm^3mol^{-1}s^{-1}$ calculated using the RatesMC [71] code. The upper and lower rates (corresponding to 1σ) are also listed.

T(GK)	Lower Limit	Recommended Value	Upper Limit
0.01	3.39×10^{-25}	3.81×10^{-25}	4.29×10^{-25}
0.011	3.59×10^{-24}	4.05×10^{-24}	4.56×10^{-24}
0.012	2.91×10^{-23}	3.28×10^{-23}	3.68×10^{-23}
0.013	1.88×10^{-22}	2.12×10^{-22}	2.39×10^{-22}
0.014	1.02×10^{-21}	1.14×10^{-21}	1.29×10^{-21}
0.015	4.70×10^{-21}	5.30×10^{-21}	5.96×10^{-21}
0.016	1.91×10^{-20}	2.15×10^{-20}	2.42×10^{-20}
0.018	2.28×10^{-19}	2.56×10^{-19}	2.88×10^{-19}
0.02	1.96×10^{-18}	2.19×10^{-18}	2.46×10^{-18}
0.025	1.86×10^{-16}	2.06×10^{-16}	2.28×10^{-16}
0.03	8.72×10^{-15}	9.85×10^{-15}	1.12×10^{-14}
0.04	2.16×10^{-12}	2.49×10^{-12}	2.91×10^{-12}
0.05	6.66×10^{-11}	7.69×10^{-11}	8.92×10^{-11}
0.06	6.74×10^{-10}	7.74×10^{-10}	8.92×10^{-10}
0.07	3.70×10^{-9}	4.20×10^{-9}	4.78×10^{-9}
0.08	1.45×10^{-8}	1.62×10^{-8}	1.81×10^{-8}
0.09	4.64×10^{-8}	5.13×10^{-8}	5.70×10^{-8}
0.1	1.34×10^{-7}	1.47×10^{-7}	1.61×10^{-7}
0.11	3.57×10^{-7}	3.91×10^{-7}	4.28×10^{-7}
0.12	9.01×10^{-7}	9.82×10^{-7}	1.07×10^{-6}
0.13	2.15×10^{-6}	2.34×10^{-6}	2.55×10^{-6}
0.14	4.82×10^{-6}	5.22×10^{-6}	5.67×10^{-6}
0.15	1.01×10^{-5}	1.09×10^{-5}	1.18×10^{-5}
0.16	1.99×10^{-5}	2.15×10^{-5}	2.32×10^{-5}
0.18	6.46×10^{-5}	6.96×10^{-5}	7.51×10^{-5}
0.2	1.73×10^{-4}	1.86×10^{-4}	2.01×10^{-4}
0.25	1.15×10^{-3}	1.23×10^{-3}	1.33×10^{-3}
0.3	4.91×10^{-3}	5.28×10^{-3}	5.67×10^{-3}
0.35	1.94×10^{-2}	2.08×10^{-2}	2.24×10^{-2}
0.4	7.79×10^{-2}	8.41×10^{-2}	9.06×10^{-2}

Table 6.11: (continued)

T(GK)	Lower Limit	Recommended Value	Upper Limit
0.45	2.84×10^{-1}	3.09×10^{-1}	3.35×10^{-1}
0.5	8.77×10^{-1}	9.55×10^{-1}	$1.04\times10^{+0}$
0.6	$5.16\times10^{+0}$	$5.63\times10^{+0}$	$6.16\times10^{+0}$
0.7	$1.87\times10^{+1}$	$2.04\times10^{+1}$	$2.22\times10^{+1}$
0.8	$4.90\times10^{+1}$	$5.33\times10^{+1}$	$5.80\times10^{+1}$
0.9	$1.03\times10^{+2}$	$1.12\times10^{+2}$	$1.21\times10^{+2}$
1	$1.85\times10^{+2}$	$2.01\times10^{+2}$	$2.17\times10^{+2}$
1.25	$5.17\times10^{+2}$	$5.58\times10^{+2}$	$6.02\times10^{+2}$
1.5	$9.93\times10^{+2}$	$1.07\times10^{+3}$	$1.15\times10^{+3}$
1.75	$1.55\times10^{+3}$	$1.66\times10^{+3}$	$1.78\times10^{+3}$
2	$2.11\times10^{+3}$	$2.27\times10^{+3}$	$2.43\times10^{+3}$
2.5	$3.14\times10^{+3}$	$3.37\times10^{+3}$	$3.60\times10^{+3}$
3	$3.94\times10^{+3}$	$4.21\times10^{+3}$	$4.50\times10^{+3}$
3.5	$4.49\times10^{+3}$	$4.80\times10^{+3}$	$5.11\times10^{+3}$
4	$4.83\times10^{+3}$	$5.15\times10^{+3}$	$5.49\times10^{+3}$
5	$5.04\times10^{+3}$	$5.37\times10^{+3}$	$5.73\times10^{+3}$
6	$4.93\times10^{+3}$	$5.25\times10^{+3}$	$5.60\times10^{+3}$
7	$4.67\times10^{+3}$	$4.98\times10^{+3}$	$5.31\times10^{+3}$
8	$4.39\times10^{+3}$	$4.69\times10^{+3}$	$5.01\times10^{+3}$
9	$4.12\times10^{+3}$	$4.40\times10^{+3}$	$4.70\times10^{+3}$
10	$3.86\times10^{+3}$	$4.12\times10^{+3}$	$4.39\times10^{+3}$

A full discussion of how the results presented in this chapter compare with the findings of previous investigations follows in Chapter 7 where the astrophysical implications of this work are also presented.

Chapter 7

Discussion and Astrophysical Implications

7.1 Comparison with previous investigations

In Chapter 6 the results of the present study of the $^{17}O(p,\gamma)^{18}F$ reaction were presented. In summary:

- The total non-resonant S-factor has been accurately measured, with an uncertainty of approximately 9%, over the energy range E_{cm} = 204-370 keV.
- The strength of the $E_R = 183$ keV resonance has been determined as $\omega\gamma = (1.70 \pm 0.15) \times 10^{-6}$ eV, providing the most precise measurement to date.
- The uncertainty associated with the $^{17}O(p,\gamma)^{18}F$ reaction rate has been significantly reduced inside the classical novae Gamow window and now stands at approximately 16%.

7.1.1 Non-resonant S-factor and the $E_R = 183$ keV resonance strength

The total S-factor measured in the present study is presented alongside the results published by Fox *et al.* [33], Newton *et al.* [38] and Hager *et al.* [41] in Figure 7.1. The solid line and solid-symbol data points represent the results obtained in the

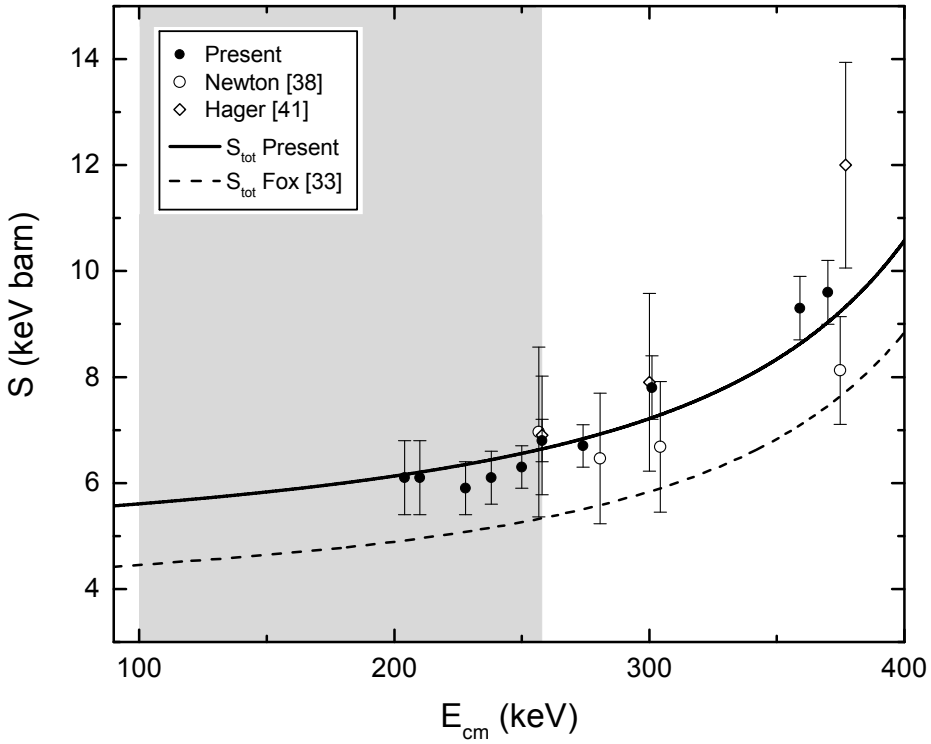

Figure 7.1: Total S-factor for the $^{17}O(p,\gamma)^{18}F$ reaction as determined in the present study (solid data points and line). The S-factor parametrisation from the work of Fox *et al.* [33] is shown by the dashed line, while the S-factor data of Newton *et al.* [38] and Hager *et al.* [41] are also shown (open symbols). The grey region indicates the Gamow energy region for classical novae.

present investigation while measurements from the previous studies cited above are plotted using open symbols. Importantly, several of the S-factor data points obtained in this work lie within the Gamow window for classical novae (indicated by the shaded area in Figure 7.1), thus providing the first accurate information inside this low-energy region. The dashed line in Figure 7.1 illustrates the total S-factor parametrisation published in [33], which is approximately 20% lower than the values obtained in present study, although still compatible given the high degree of uncertainty (50%) associated with the work of [33]. Extrapolating to zero energy, the value of $S(0)$ quoted in Chapter 6 is found to be in good agreement with the results from [38] and [43] (see Table VII in [43]).

The strength of the $E_{\rm cm} = 183$ keV resonance determined in the present study is incompatible with the resonance strength measured by Fox *et al.* [33] (Figure 7.2). However, Fox *et al.* only observed the two strongest primary

transitions (R→937 and R→1080). The present study has demonstrated that only approximately 65% (Table 6.8) of the total yield arises from these transitions, suggesting that the result obtained in [33] should be revised accordingly. Applying this correction brings the resonance strength value of Fox *et al.* [33] into agreement with the result obtained in the present study as well as with the value quoted in [36], as shown in Figure 7.2.

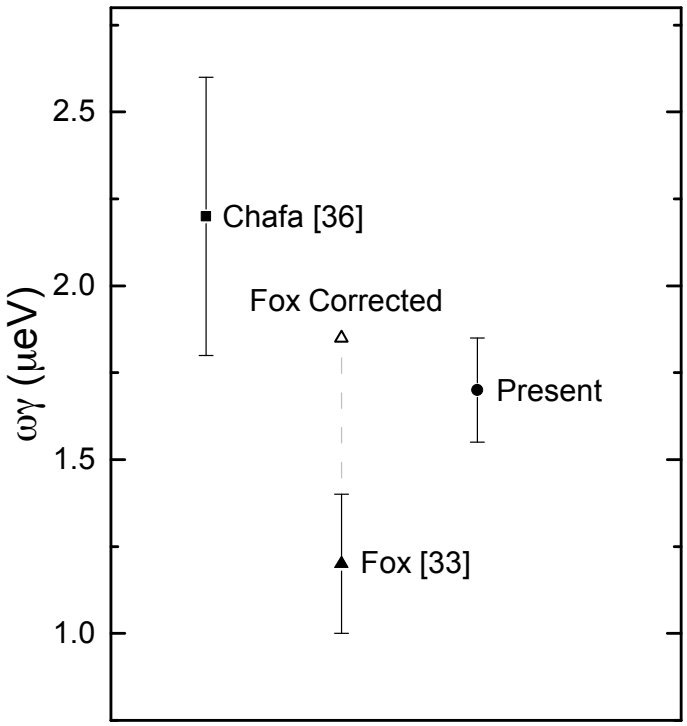

Figure 7.2: Strength of the $E_R = 183$ keV resonance as measured by Fox *et al.* [33] (solid triangle), Chafa *et al.* [36] (solid square) and in the present study (solid circle). Correcting the result of [33] as described in the text leads to the value shown by the open triangle.

7.1.2 Reaction rate comparison

Figure 7.3 compares the present reaction rate with the perviously recommended value of Iliadis *et al.* [40]. The ratio of the rate from [40] and the present rate is shown by the dashed line, while the grey area represents the corresponding uncertainty. The hatched area indicates the uncertainty associated with the present rate. In the temperature region between 0.1 and 0.4 GK, the current

rate is up to 15% higher than that reported in [40]. This difference is mainly due to the higher value of the $E_{\rm R}$=183 keV resonance strength (1.7 μeV compared to 1.2 μeV from [33]) and the larger non-resonant S-factor contribution determined in the present work. At higher energies, the latest measurements of the $E_{\rm R}$ = 556 and 677 keV resonances reported in [43] also lead to an increased rate with respect to that of [40].

The reaction rate uncertainty in the energy region relevant for classical novae has been reduced from over 50% (as published in [40]) to approximately 16%. In Section 7.4 I will discuss the implications of this improved rate with respect to a series of hydrodynamic novae models.

For completeness, the present reaction rate was also compared with the results published in the recent work of Kontos *et al.* [43] and found to be consistently within 10% of their value[1]. It should be noted that the uncertainty associated with the reaction rate determination of [43] is comparable to that of the present investigation, although this is largely due to experimental information adopted from [36] and [38].

7.2 Activation results

The analysis and results presented so far in this thesis relate to a subset of the data acquired by the LUNA collaboration in our investigation of the ^{17}O(p,γ)^{18}F reaction. As previously mentioned, measurements were also performed using the activation technique, the results of which are published in [1] and [2]. The activation study was successful in measuring the total S-factor down to energies as low as approximately $E_{\rm cm}$ = 160 keV. Figure 7.4 presents the total S-factor obtained from the present prompt γ-ray analysis and the corresponding results from the activation measurements. The data obtained using these two independent techniques are in fairly good agreement, particularly at energies below $E_{\rm cm}$ = 300 keV. In order to make a more rigorous comparison between these data sets the non-common systematic uncertainties (approximately 5% [2]) should also be considered.

In addition to the non-resonant S-factor, the strength of the $E_{\rm R}$ = 183 keV resonance has been measured following the activation approach, resulting in a

[1]The rate originally published by Kontos *et al.* [43] contained a numerical error which affected the final result by 10-20% as explained in [74].

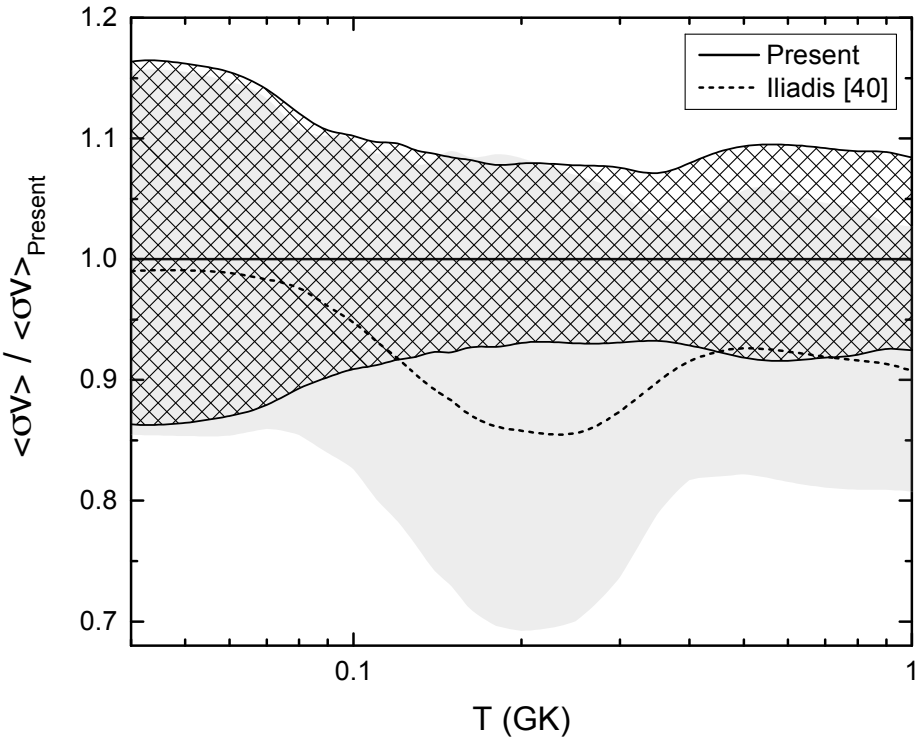

Figure 7.3: The ^{17}O(p,γ)^{18}F reaction rate ratio as a function of temperature. The ratio of the rate from [40] and the present rate is shown by the dashed line while the corresponding uncertainty is represented by the grey area. The uncertainty associated with the present rate is indicated by the hatched area.

value of $\omega\gamma = 1.65 \pm 0.14$ μeV. Once again, this measurement is in excellent agreement with the value obtained from the present prompt γ-ray analysis ($\omega\gamma = 1.7 \pm 0.15$ μeV). The activation measurements described above therefore serve as an independent confirmation of the results presented in this thesis.

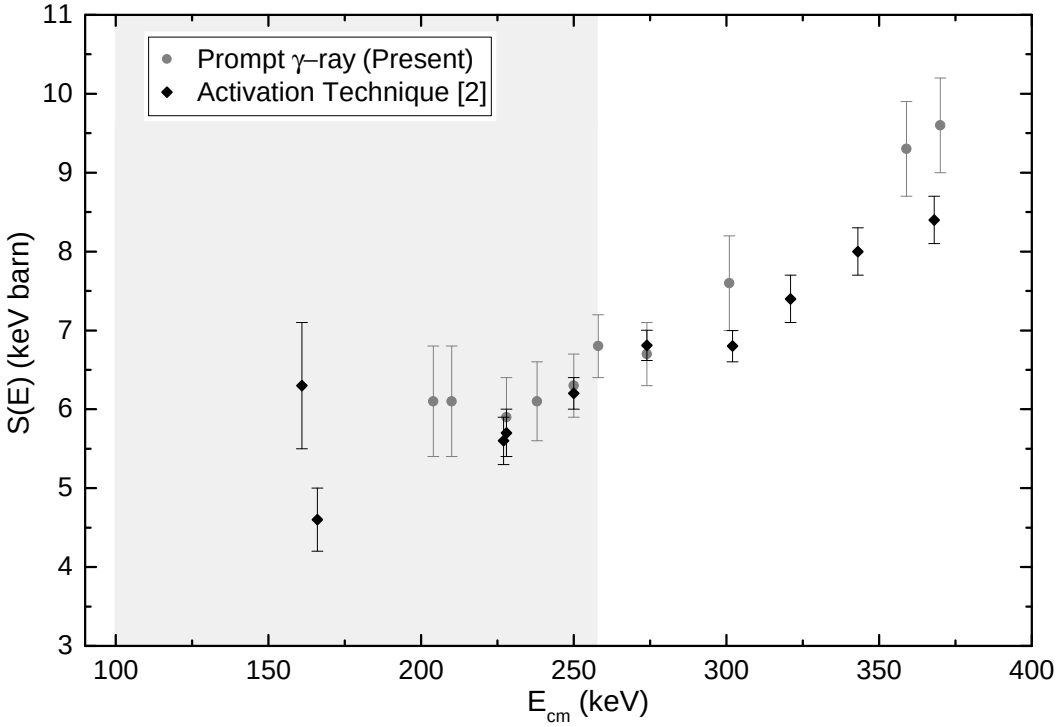

Figure 7.4: The total S-factor for the ^{17}O(p,γ)^{18}F reaction as determined from the prompt γ-ray analysis of the present study (circular grey points) compared to the results from the activation measurements (solid black diamonds), also performed by the LUNA collaboration [2].

7.3 LUNA global analysis

The LUNA collaboration has recently published a global analysis of all currently available data relating to the ^{17}O(p,γ)^{18}F reaction [2]. The total S-factor presented in [2] was determined following a common fit procedure, which included the prompt γ-ray and activation data sets acquired by the LUNA collaboration in addition to the higher energy measurements of [38], [41] and [43]. Performing a common analysis including results obtained in several independent studies

is complicated by the fact that each data set generally suffers from different systematic uncertainties. This leads to a correlation between different data sets and may result in a biased estimation of the total S-factor if not properly accounted for. Scaling factors [75, 76] are introduced to model the systematic uncertainties associated with each set of measurements and a modified χ^2 fit is performed as described in [2]. A similar application of this procedure can also be found in [77].

Applying the method outlined above benefits from the inclusion of additional data leading to a more accurate determination of the total S-factor. Another advantage of the common fit approach is that the partial widths required to calculate the broad resonance contributions to the total cross section (accounting for up to 45% of the total cross section in the energy range E_{cm} = 200-370 keV) are free parameters in the global fit. This is in contrast to the present work, a shortcoming of which is the reliance on partial width information adopted from [43].

The total S-factor determined in [2] is within 5% of the value obtaind from the present prompt γ-ray analysis, although the uncertainty on the former result is approximately 30% lower due to the inclusion of the additional data as previously mentioned. This leads to a reaction rate uncertainty of approximately 9% in [2] (as opposed to the 16% reported in this thesis) in the energy range E_{cm} = 200 - 370 keV. The results published in [2] therefore represent the latest and most accurate information regarding the ^{17}O(p,γ)^{18}F reaction rate and supersede those presented in Table 6.11. In practice, the difference in uncertainty between the results published here and those of [2] is of little consequence in terms of the astrophysical implications discussed in the following section.

7.4 Astrophysical implications for classical novae

In Chapter 1 a brief overview of the scenario leading up to a classical nova event was provided. The ^{17}O(p,γ)^{18}F reaction forms part of the main energy generation process (the hot-CNO cycles) powering classical novae and influences the production of certain rare isotopes such as ^{15}N, $^{17/18}$O and $^{18/19}$F. In order to ascertain what effect the rate of this reaction has on the abundance these

isotopes, a series of nova model calculations have been performed in the framework of the LUNA collaboration by J. José using the spherically symmetric (1-D) hydrodynamic code, SHIVA [13]. The SHIVA code models the hydrodynamic processes that occur on the surface of an accreting white dwarf (*e.g.* mixing between convective layers) and is linked to a comprehensive reaction network which includes 370 possible nuclear reactions. The evolution of nuclei ranging from ^{1}H to ^{40}Ca are tracked at various stages (from the onset of accretion to the ejection phase) of a classical nova event, allowing their final abundances to be calculated. Further details relating the the SHIVA code can be found in [13].

As discussed in Chapter 1, the mass and chemical composition of the underlying white dwarf has a significant effect on the nucleosynthesis that takes place during a classical nova event. Other factors such as the extent of mixing between the white dwarf core and accreted envelope in addition to the mass accretion rate also play a role in determining the characteristics of the thermonuclear runaway and subsequent nova outburst. Many of these parameters are relatively un-constrained and are expected to vary depending on the specific attributes of a given binary system. Because of this, several nova simulations were performed, corresponding to a range of model inputs. The different models are distinguished by the values used for certain key parameters. These include the mass of the white dwarf, the core composition (C-O or O-Ne) and the amount of core material mixed into the surface envelope.

For each model considered, the effect of varying the rate of the ^{17}O(p,γ)^{18}F reaction on final abundances of the isotopes, ^{15}N, $^{18/19}$F and ^{18}O, has been investigated. The results of this study are shown in Table 7.4. White dwarf masses between 1 - 1.35 $M_{\odot}$ were considered. The corresponding core composition reflects the fact that more massive white dwarfs are expected to mainly consist of O and Ne rather than C and O. Mixing levels of 25% and 50% were adopted, consistent with the wide spread of metallicities observed in novae ejecta [78]. A mass accretion rate of 2×10^{-10} $M_{\odot}$ yr^{-1} was assumed in these models. The total accreted mass is determined by the accretion timeframe prior to the onset of the thermonuclear runaway. Since more massive white dwarfs are associated with higher surface temperatures, the thermonuclear runaway is initiated at earlier times. Further information relating to the models implemented can be found in [13].

The abundances presented in Table 7.4 are given in terms of the mass fraction compared to the total ejected mass. Under the heading '^{17}O(p,γ)^{18}F rate' in Table 7.4, *present*, *upper* and *lower* refer to the reaction rates obtained in the present study and the upper and lower rates published in [1], respectively. For comparison, final abundances assuming the reaction rate from [40] (denoted as $IL2010$) were also evaluated.

The abundances predicted using the ^{17}O(p,γ)^{18}F reaction rates from the present study and from [40] generally differ by only a few percent. The maximum variations in abundances are observed for ^{18}O and ^{18}F, which are up to 5% higher with the present rate. The uncertainties associated with the present reaction rate leads to variations in the abundance of ^{18}O and ^{18}F of approximately 10%, while the abundances of ^{19}F and ^{15}N remain almost constant.

Due to our presently limited understanding of certain features of novae such as the precise mixing mechanism operating at the base of the envelope, and the mass accretion rate, these model uncertainties are generally expected to be greater than 10%. As seen, the effect of varying the ^{17}O(p,γ)^{18}F reaction rate (in the manner described above) leads to changes in isotopic abundances within this range, thus the rate of this reaction is now sufficiently well determined to place firmer constraints on observational features of novae nucleosynthesis.

Table 7.1: Results of nova model calculations obtained using the hydrodynamic SHIVA code [13]. The abundances (given in mass fraction) of ^{18}F, ^{18}O, ^{19}F and ^{15}N are determined for a range of model parameters, using different values of the ^{17}O$(p,\gamma)^{18}$F reaction rate. See text for further details.

Model	White Dwarf Mass ($M_\odot$)	Accreted Mass ($10^{-5}M_\odot$)	Core Composition	Mixing (%)	$T_{\rm peak}$ (10^8 K)	^{17}O$(p,\gamma)^{18}$F rate	^{18}F	^{18}O	^{19}F	^{15}N
CO1	1.00	2.709	CO	25	1.73	Present	1.30×10^{-6}	4.87×10^{-7}	9.57×10^{-9}	8.60×10^{-3}
CO1	1.00	2.709	CO	25	1.73	IL2010	1.25×10^{-6}	4.68×10^{-7}	9.48×10^{-9}	8.60×10^{-3}
CO1	1.00	2.709	CO	25	1.73	Upper	1.39×10^{-6}	5.20×10^{-7}	9.76×10^{-9}	8.60×10^{-3}
CO1	1.00	2.709	CO	25	1.73	Lower	1.22×10^{-6}	4.60×10^{-7}	9.48×10^{-9}	8.60×10^{-3}
CO2	1.15	1.437	CO	25	2.00	Present	2.63×10^{-6}	1.10×10^{-6}	1.09×10^{-8}	3.03×10^{-3}
CO2	1.15	1.437	CO	25	2.00	IL2010	2.52×10^{-6}	1.05×10^{-6}	1.07×10^{-8}	3.03×10^{-3}
ONe1	1.15	2.456	ONe	50	2.28	Present	8.46×10^{-6}	3.64×10^{-6}	5.48×10^{-8}	3.57×10^{-2}
ONe1	1.15	2.456	ONe	50	2.28	IL2010	8.15×10^{-6}	3.45×10^{-6}	5.38×10^{-8}	3.57×10^{-2}
ONe2	1.25	1.887	ONe	50	2.48	Present	1.12×10^{-5}	4.90×10^{-6}	1.42×10^{-7}	5.65×10^{-2}
ONe2	1.25	1.887	ONe	50	2.48	IL2010	1.09×10^{-5}	4.75×10^{-6}	1.40×10^{-7}	5.66×10^{-2}
ONe2	1.25	1.887	ONe	50	2.48	Upper	1.13×10^{-5}	5.39×10^{-6}	1.43×10^{-7}	5.67×10^{-2}
ONe2	1.25	1.887	ONe	50	2.48	Lower	1.09×10^{-5}	4.74×10^{-6}	1.41×10^{-7}	5.65×10^{-2}
ONe3	1.35	0.455	ONe	50	3.13	Present	3.49×10^{-5}	1.56×10^{-5}	1.20×10^{-6}	1.07×10^{-1}
ONe3	1.35	0.455	ONe	50	3.13	IL2010	3.50×10^{-5}	1.56×10^{-5}	1.20×10^{-6}	1.07×10^{-1}

Summary and Conclusions

The ^{17}O(p,γ)^{18}F reaction, which forms part of the hot-CNO cycle, affects the synthesis of certain rare isotopes such as ^{15}N, $^{17/18}$O and $^{18/19}$F produced in classical novae. The unstable isotope ^{18}F ($t_{1/2}$ = 110 min) is of particular importance as it could potentially act as a tracer for novae events through the detection of 511 keV annihilation γ rays following its β^+ decay. Determining the rate of the ^{17}O(p,γ)^{18}F reaction is therefore important in constraining nucleosynthesis calculations in novae models.

This thesis has reported on the experimental study of the ^{17}O(p,γ)^{18}F reaction cross section at Gamow energies for classical novae. This work was carried out at the LUNA underground accelerator facility, where the intrinsically low level of γ-ray background (as low as 10^{-3} counts/h in the region of interest) has allowed for the sensitive detection of prompt γ rays associated with the formation and decay of states in ^{18}F. Following the thick-target yield approach, the total non-resonant S-factor for the ^{17}O(p,γ)^{18}F reaction has been determined in the energy range $E_{\rm cm}$ = 204-370 keV with an accuracy of approximately 9%. These measurements represent the first accurate experimental information obtained *directly* inside the energy region relevant for classical novae ($E_{\rm cm}$ = 100-260 keV). In addition to the non-resonant contribution to the ^{17}O(p,γ)^{18}F reaction cross section, the strength of the $E_{\rm R}$ = 183 keV resonance has also been determined with unprecedented precision.

The results from this study were used to calculate the reaction rate using the *RatesMC* code [71] and a series of hydrodynamic novae models [13] were implemented in order to quantify the effect that varying this rate within its uncertainty has on the abundances of the rare isotopes mentioned above. These simulations have confirmed that the ^{17}O(p,γ)^{18}F reaction rate uncertainty has now reached the level of precision required for accurate novae models.

To improve our theoretical understanding of classical novae, refinements in modelling the hydrodynamic processes occurring in novae systems (for instance concerning the mass accretion rate and hydrodynamic mixing mechanism) are required. From a nuclear physics standpoint, it is essential that the rates of reactions such as ^{18}F(p,α)^{15}O (responsible for destroying ^{18}F) and ^{17}O(p,α)^{14}N are better constrained in the novae energy region. A recent investigation of the ^{18}F(p,α)^{15}O reaction has been performed in [79] while the study of the ^{17}O(p,α)^{14}N reaction at novae energies is currently ongoing at LUNA.

If satellite missions such as the European Space Agencies INTEGRAL observatory are successful in detecting γ rays from classical novae events, accurate novae simulations based on improved nuclear physics inputs may prove invaluable in interpreting the observed spectral features.

Appendix A

The Interaction of γ Rays with Matter

Gamma rays interact with matter via three main processes: the *photoelectric effect*, *Compton scattering* and *pair production*, with a relative probability that depends on the energy of the incident γ ray and the atomic number of the absorbing medium.

The photoelectric effect dominates at energies up to several hundred keV and involves a γ ray transferring the entirety of its energy to an atomic electron, ejecting it from the atom as a *photoelectron*. If not absorbed in a single event, γ rays may undergo a series of scattering interactions with electrons inside the detection medium. This process is referred to as Compton scattering and results in the initial energy of the γ ray being transferred to one or more recoil electrons.

At higher energies (typically above 5 MeV) a third process, pair production, becomes important. If the energy of an incident γ ray is greater than twice the rest energy of an electron ($2m_ec^2 = 1.022$ MeV), an electron-positron pair may be formed. Following this interaction the newly created positron soon undergoes annihilation with an electron leading to the production of two 511 keV γ rays, which may then deposit their energy via Compton scattering or the photoelectric effect as described above.

The net effect of these fundamental processes is the creation of free charge (in proportion to the energy deposited) through ionisation of the absorbing medium. In order for a material to operate as a γ-ray detector the charge carriers must be collected and converted into an electrical signal. This can be achieved using a

semiconducting medium such as germanium as the active volume of the detector (Section A.2).

For a detector of sufficient volume, the entirety of the energy of an incident γ ray will be deposited in the detection medium. This results in a peak (referred to as the full-energy peak) in the γ-ray spectrum at an energy equivalent to that of the incident γ rays. However, depending on the dimensions and geometry of a given detector, γ rays may deposit only a fraction of their total energy. This for instance occurs if a γ ray undergoes a Compton scattering event but subsequently leaves the detector before all of its energy has been lost. The γ-ray spectrum resulting from such processes will display a continuum (referred to as the Compton continuum) corresponding to γ rays depositing differing amounts of energy depending on the strength of the scattering interactions in which they are involved. The maximum amount of energy that can be transferred to an electron in a single scattering event occurs at a scattering angle of 180° (perfect backscattering) and corresponds to the spectral feature referred to as the Compton edge. A similar scenario may arise for γ rays participating in pair production. In this case one or both of the 511 keV γ rays resulting from positron annihilation (described above) may escape the detector before depositing their energy. This possibility leads to two peaks (in addition to the full-energy peak) separated by 511 keV. The *1st escape peak* corresponds to pair-production events where only one of the annihilation γ rays escapes detection, while the *2nd escape peak* arises when both γ rays leave the detector. Figure A.1 illustrates a typical spectrum for a mono-energetic source of γ rays where each of the spectral features described above is illustrated. A diagram showing examples of three possible γ-ray interaction histories is also shown.

A.1 Detection efficiency

There are two distinct types of efficiency that are important for studies such as this one. The absolute full-energy peak efficiency, η_{ph}, relates the number of γ rays emitted by the source to the area under the peak (*i.e.* the full-energy peak) that corresponds to γ rays that have undergone complete absorption in a single event inside the detection medium. Since Compton scattering effects can lead to a series of incomplete absorptions, not all γ rays that enter the detector will

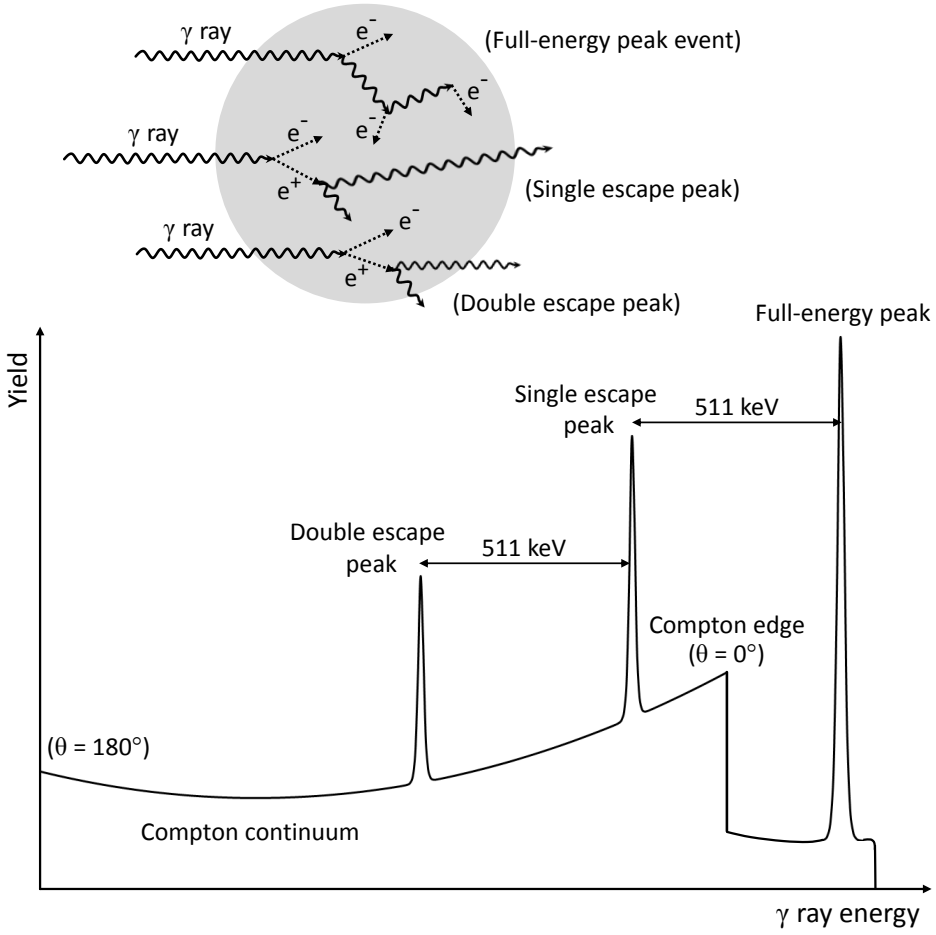

Figure A.1: Upper: Depiction of three possible γ-ray events inside the active detector volume (grey area). Lower: Typical γ-ray spectrum from a HPGe detector indicating certain common spectral features (see text).

appear in the full-energy peak. The total efficiency, ϵ_{tot}, is therefore introduced to relate the number of emitted γ rays to the number of counts detected *anywhere* in the spectrum.

A.2 Semiconductor detectors

A semiconductor is a material possessing an electrical conductivity between that of a pure metal and an insulator. The properties of a semiconductor are determined by the energy gap between the electronic valence and conduction

bands (see for instance [80]). If a sufficient amount of energy is deposited (via the processes described in the previous section) the effect is to promote electrons from the valence band into the conduction band. This leads to the creation of charge carriers in the form of electron-hole pairs.

The conductivity of a semiconductor can be modified by introducing atoms of a different element into the crystal structure, in a process referred to as *doping*. If the dopant atoms have an excess of electrons (referred to as *donor* electrons) compared to the host semiconductor an *n-type* semiconductor is produced. Similarly, if the added dopant has a relative shortage electrons a *p-type* semiconductor is created where the atoms introduced are referred to as *acceptors*.

If two semiconductors of n-type and p-type are brought into contact, the donor electrons will be captured by the acceptor atoms leading to a neutral *depletion layer* at the interface. The width of this region can be increased with the application of a reverse bias voltage. In this configuration, the negatively and positively charged constituents (electrons and holes) resulting from γ-ray interactions inside the depletion layer will travel in opposite directions producing an electrical current. The total collected charge is directly proportional to the energy deposited by the incident radiation.

The configuration of a p-type co-axial germanium detector such as the one used in the present study of the ^{17}O(p,γ)^{18}F reaction is shown in Figure A.2

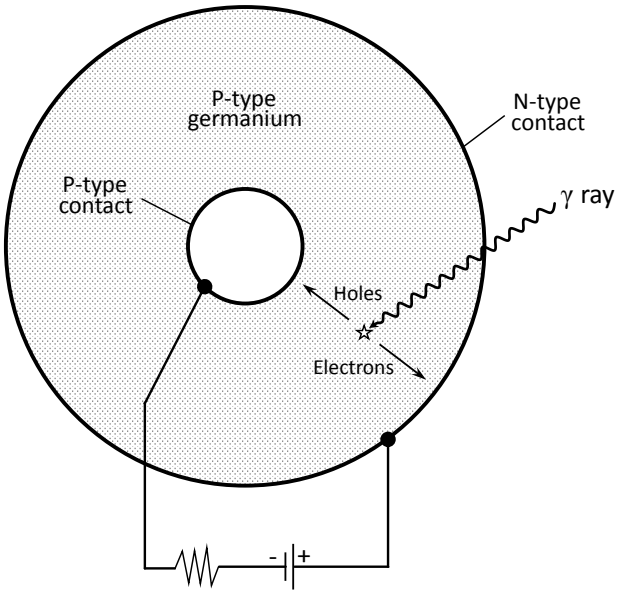

Figure A.2: Diagram of a p-type co-axial germanium detector.

Appendix B

Target Stochiometry and Isotopic Composition

The stochiometry of our Ta_2O_5 targets was determined using the Rutherford backscattering (RBS) technique [81]. This involves bombarding a sample with ions (typically protons or alpha particles with energies in the MeV range) and measuring the projectiles resultant energy after undergoing elastic scattering with the target nuclei. The RBS cross section, σ_{RBS}, is proportional to the charge of the particles involved, allowing the elemental composition of the target to be determined by measuring the yield of the scattered projectiles:

$$\text{Yield} \propto \sigma_{\mathrm{RBS}} \propto \frac{Z_1 Z_2}{E^2} \tag{B.1}$$

Measurements of the target stochiometry were carried out by fellow members of the LUNA collaboration at the Laboratori Nazionali di Legnaro (LNL), Italy. A ^{4}He beam of approximately $E_{\mathrm{cm}} = 2$ MeV was incident on the target surface and a silicon detector, positioned at 160° with respect to the beam axis, was used to record the scattered α particles. Figure B.1 shows the (normalised) α-particle yield measured for three Ta_2O_5 targets of different isotopic oxygen enrichment. In this plot, the step in yield at high energy (proportional to channel number) corresponds to alpha particles scattered from nuclei within the Ta_2O_5 layer. After passing through this layer, the incident beam enters the Ta backing, as indicated by the increase in the yield of scattered α particles (Equation B.1).

The tantalum and oxygen content of the Ta_2O_5 layer was determined using the computer code SIMNRA [82] to fit the RBS spectra (dashed line in Figure

B.1). This led to a value of 2.1×10^{17} Ta/cm^2 and 5.4×10^{17} O/cm^2, and hence a Ta/O ratio of 0.39 $\pm$ 0.02, in excellent agreement with the expected value of 0.4 [61] [83]. The uncertainty of approximately 5% associated with this measurement translates into an additional 3% of uncertainty on the effective stopping power (estimated using SRIM).

The stochiometric ratio was found to remain constant under proton bombardment. This was demonstrated by performing RBS measurements inside the area of the target exposed to the beam as well as on a peripheral region of the target (outside of the beam-spot). As an example, the results of such a measurement conducted using a target subjected to approximately 23C of accumulated charge are shown in Figure B.2. The width of the Ta_2O_5 layer is approximately 20% thinner inside the area exposed to the beam compared to the undamaged regions of the target.

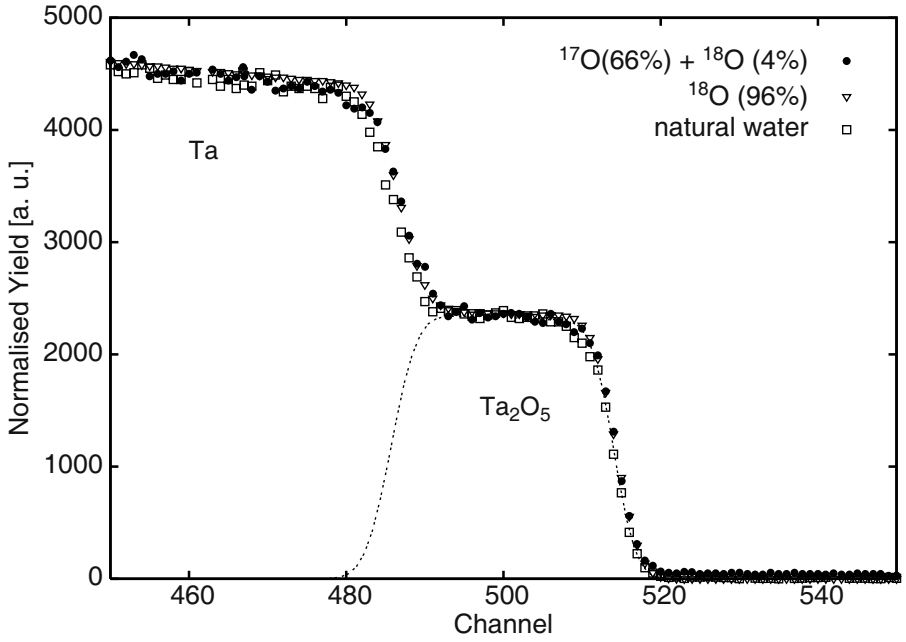

Figure B.1: Rutherford backscattering (RBS) spectra (normalised alpha-particle yield versus channel) measured for three Ta_2O_5 targets of different isotopic oxygen enrichment [60]. The constant width of the Ta_2O_5 layer indicates that the target thickness is independent of the oxygen content of the target. The consistent shape of the yield profile demonstrates the reliability of the target production method. The dashed line represents the simulated yield from calculations made using the software package SIMNRA [82].

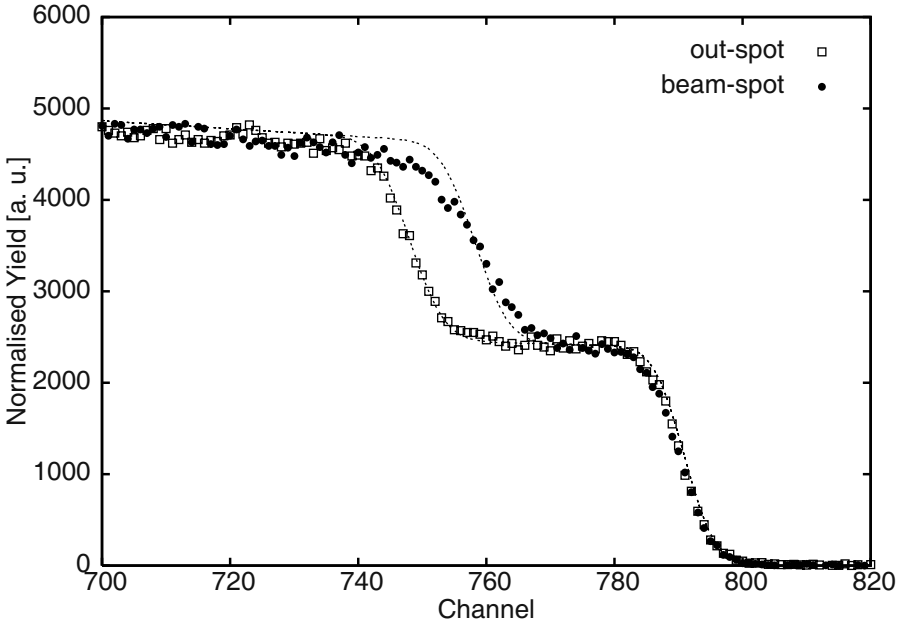

Figure B.2: Rutherford backscattering (RBS) spectra from measurements performed on a Ta_2O_5 target exposed to 23C of accumulated charge [60]. The solid and open symbols represent measurements made inside (beam-spot) and outside (out-spot) the region previously exposed to the proton beam, respectively. The predicted yield calculated using the software package SIMNRA is shown by the dashed line.

As previously mentioned, the abundance of the different isotopes of oxygen present in our targets must be determined in order to calculate the effective stopping power. This information was obtained from Secondary ion mass spectrometry (SIMS) [84] measurements. This technique is based on detecting the charged particles (secondary ions) that are ejected from the surface of a target bombarded by a (primary) beam of heavy particles. The secondary ions (in this case $^{16}O^-$, $^{17}O^-$ and $^{18}O^-$) must then be separated using a *mass spectrometer*, which operates on the principle that ions with different charge to mass ratios are deflected to varying extents in the presence of a constant magnetic field. The measured yield of each oxygen isotope reflects the relative abundance present in the target.

SIMS measurements were performed at the Department of Physics and Astronomy of the University of Padua, Italy. A Cs^+ beam was used to sputter oxygen ions from the target surface and a CAMECA IMS-4f spectrometer was

used to separate each isotope of oxygen.

Figure B.3 shows the relative abundance of each isotope of oxygen from SIMS measurements performed on one of the Ta_2O_5 targets used in the present study. The yield of each oxygen isotope is plotted as a function of the sputtering time, *i.e.* the time for which the target has been exposed to the Cs^+ beam. The solid and dashed lines correspond respectively to data obtained inside and outside the region previously exposed to the proton beam during measurements of the $^{17}O(p,\gamma)^{18}F$ reaction. The smooth plateau evident for each oxygen isotope reflects the uniform distribution of the oxygen layer, while the earlier drop in yield for the measurements performed inside the beam-spot corresponds to a reduced target thickness in that area. It takes approximately 20 seconds for the system to reach stability, as indicated by the initial rise in yield. The relative abundance of each oxygen isotope can be determined directly from the ratio of the yields plotted in Figure B.3. The ^{17}O content of the targets used in this study ranged from 64 - 67%.

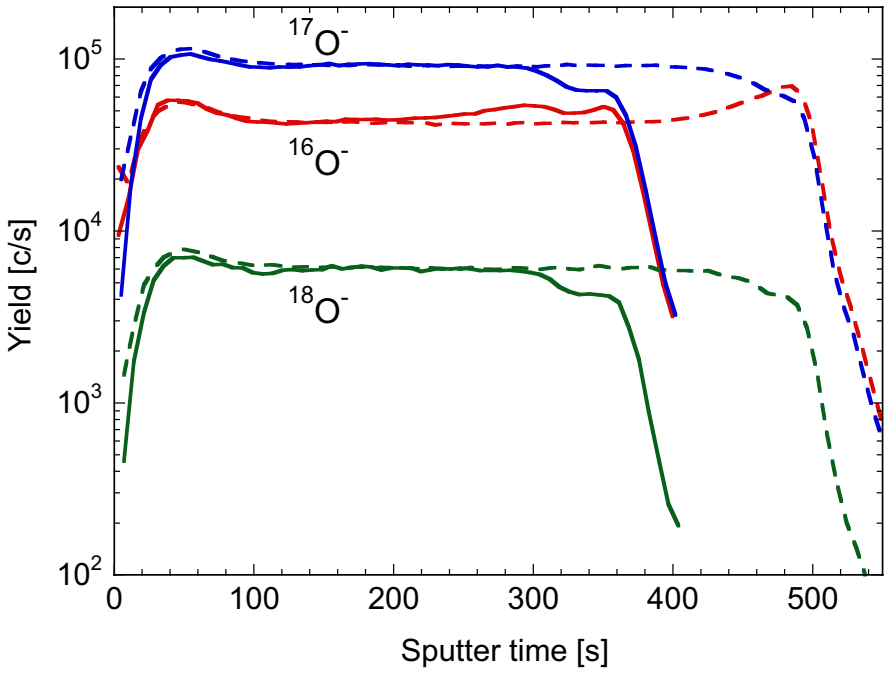

Figure B.3: Results of Secondary Ion Mass Spectrometry (SIMS) measurements performed on one of the Ta_2O_5 targets used in the present study [60]. The yields of different oxygen isotopes sputtering from the target surface are plotted as a function of sputtering time. The solid and dashed lines respectively refer to measurements made inside and outside the regions previously exposed to the proton beam during measurement of the $^{17}O(p,\gamma)^{18}F$ reaction.

Bibliography

[1] D. A. Scott *et al.*, *Physical Review Letters* **109**, 202501 (2012).

[2] A. Di Leva *et al.*, *Physical Review C* **89**, 015803 (2014).

[3] H. A. Bethe and C. L. Critchfield, *Physical Review* **54**, 248 (1938).

[4] R. A. Alpher, H. A. Bethe and G. Gamow, *Physical Review* **73**, 7 (1948).

[5] E. M. Burbidge, G. R. Burbidge, W. A. Fowler, and F. Hoyle, *Reviews of Modern Physics* **29**, 547 (1957).

[6] H. E. Suess and H. C. Urey, *Reviews of Modern Physics* **28**, 53 (1956).

[7] H. Reeves, Stellar Evolution and Nucleosynthesis (Gordon and Breach, Science Publishers Inc., 1968).

[8] D. A. Ostlie and B. W. Carroll, An Introduction to Modern Stellar Astrophysics (Pearson Education, Inc., 2007).

[9] C. E. Rolfs and W. S. Rodney, Cauldrons in the Cosmos (University of Chicago Press, Chicago, 1988).

[10] C. Iliadis, Nuclear Physics of Stars (Wiley-VCH, New York, 2007).

[11] D. Prialnik, Theory of Stellar Structure and Evolution (Cambridge University Press, 2010).

[12] M. F. Bode and A. Evans, Classical Novae (Cambridge University Press, 2008).

[13] J. José and M. Hernanz, *The Astrophysical Journal* **494**, 680 (1998).

[14] J. Casanova, J. José, E. Garcia-Berro, S. N. Shore, and A. C. Calder, *Nature* (London) **478**, 490 (2011).

[15] http://www.galex.caltech.edu/media/glx2007-01r_vid01.html (15th June 2014).

[16] A. W. Shafter, *The Astrophysical Journal* **487**, 226 (1997).

[17] K. Nishiyama and F. Kabashima, *PNV J18202726-2744263,* 2012.

[18] http://www.irida-observatory.org/Observations/PNV-Del/PNV-Del.html (15th June 2014).

[19] J. José and M. Hernanz, *Journal of Physics G: Nuclear and Particle Physics* **34**, R431 (2007).

[20] A. Kovetz and D. Prialnik, *The Astrophysical Journal* **477**, 356 (1997).

[21] J. José, M. Hernanz and C. Iliadis, *Nuclear Physics A* **777**, 550 (2006).

[22] R. D. Gehrz, J. W. Truran, R. E. Williams, and S. Starrfield, *Publications of the Astronomical Society of the Pacific* **110**, 3 (1998).

[23] S. Amari *et al.*, *The Astrophysical Journal* **551**, 1065 (2001).

[24] S. Amari, *New Astronomy Reviews* **46**, 519 (2002).

[25] D. R. Tilley *et al.*, *Nuclear Physics A* **595**, 1 (1995).

[26] http://www.rssd.esa.int/INTEGRAL (15th June 2014).

[27] W. Hauser and H. Feshbach, *Physical Review* **87**, 366 (1952).

[28] I. J. Thompson and F. M. Nunes, Nuclear Reactions for Astrophysics (Cambridge University Press, 2009).

[29] *"Nudat2"* http://www.nndc.bnl.gov (15th June 2014).

[30] C. Rolfs, *Nuclear Physics A* **217**, 29 (1973).

[31] R. F. Christy and I. Duck, *Nuclear Physics* **24**, 89 (1961).

[32] C. Fox *et al.*, *Physical Review Letters* **93**, 081102 (2004).

[33] C. Fox *et al.*, *Physical Review C* **71**, 005003 (2005).

[34] C. Iliadis *et al.*, *The Astrophysical Journal Supplement Series* **134**, 151 (2001).

[35] A. Chafa *et al.*, *Physical Review Letters* **95**, 031101 (2005); 96, 031101(E) (2006).

[36] A. Chafa *et al.*, *Physical Review C* **75**, 035801 (2007).

[37] C. Angulo *et al.*, *Nuclear Physics A* **656**, 3 (1999).

[38] J. R. Newton *et al.*, *Physical Review C* **81**, 045801 (2010).

[39] C. Angulo *et al.*, *Nuclear Physics A* **656**, 3 (1999).

[40] C. Iliadis *et al.*, *Nuclear Physics A* **841**, 31 (2010).

[41] U. Hager *et al.*, *Physical Review C* **85**, 035803 (2012).

[42] D. A. Hutcheon *et al.*, *Nuclear Physics A* **718**, 515 (2003).

[43] A. Kontos *et al.*, *Physical Review C* **86**, 055801 (2012).

[44] A. M. Lane and R. G. Thomas, *Review of Modern Physics* **30(2)**, 257 (1958).

[45] W. E. Kieser, R. E. Azuma, and K. P. Jackson, *Nuclear Physics A* **331**, 155 (1979).

[46] G. F. Knoll, Radiation Detection and Measurement (John Wiley & Sons, Inc., 2000).

[47] J. F. Ziegler, http://www.srim.org (15th June 2014).

[48] A. Lemut, *The European Physical Journal A* **36**, 233 (2008).

[49] G. Audi, A. H. Wapstra, and C. Thibault, *Nuclear Physics A* **729**, 337 (2003).

[50] T. Stanev, High Energy Cosmic Rays (Springer, New York, 2010).

[51] D. J. Griffiths, Introduction to Electrodynamics (Prentice-Hall, Inc., 1999).

[52] A. Formicola *et al.*, *Nuclear Instruments and Methods A* **507**, 609 (2003).

[53] S. Ahlen *et al.*, *Physics Letters B* **249**, 149 (1990).

[54] A. Caciolli *et al.*, *The European Physical Journal A* **39**, 179 (2009).

[55] www.lngs.infn.it (15th June 2014).

[56] H. Costantini *et al.*, *Reports on Progress in Physics* **72**, 086301 (2009).

[57] http://www.highvolteng.com (15th June 2014).

[58] J. D. Cockcroft and E. T. S. Walton, *Nature* **129**, 242 (1932).

[59] http://www.ortec-online.com (15th June 2014).

[60] A. Caciolli *et al.*, *The European Physical Journal A* **48**, 144 (2012).

[61] D. Phillips, *Nuclear Instruments and Methods* **116**, 195 (1974).

[62] *Cambridge Isotope Laboratories Inc.,* http://www.isotope.com.

[63] M. Laubenstein *et al.,* Applied Radiation and Isotopes **61**, 167 (2004).

[64] G. Gilmore and J. Hemingway, Practical Gamma-Ray Spectrometry, (John Wiley & Son Ltd., 1996).

[65] G. Imbriani *et al.*, *European Physical Journal A* **25**, 455 (2005).

[66] B. Limata *et al.*, *Physical Review C* **82**, 015801 (2010).

[67] http://www.gnu.org/software/gsl (15th June 2014).

[68] R. Burn and F. Rademakers, http://root.cern.ch/drupal (20th April 2014).

[69] S. Agostinelli *et al.*, *Nuclear Instruments and Methods in Physics Research A* **506**, 250 (2003).

[70] F. Strieder, *Private communication,* April 2014.

[71] R. Longland *et al.*, *Nuclear Physics A* **841**, 1 (2010).

[72] C. Iliadis, R. Longland, A. E. Champagne, and A. Coc, *Nuclear Physics A* **841**, 251 (2010).

[73] A. M. Lane and R. G. Thomas, *Reviews of Modern Physics* **30**, 257 (1958).

[74] A. Kontos *et al.*, *Physical Review C* **88**, 029905(E) (2013).

[75] G. D'Agostini, *Nuclear Instruments and Methods in Physics Research A* **346**, 306 (1994).

[76] C. M. Ko, J. Borysowicz, A. Becke, and D. Sprung, *Nuclear Physics A* **319**, 175 (1979).

[77] D. Schürmann, L. Gialanella, R. Kunz, and F. Strieder, *Physics Letters B* **711**, 35 (2012).

[78] M. Livio and J. W. Truran, The Astrophysical Journal **425**, 797 (1994).

[79] A. M. Laird *et al.*, *Physical Review Letters* **110**, 032502 (2013).

[80] D. A. Neamen, Semiconductor Physics And Devices: Basic Principles (McGraw-Hill, 2011).

[81] K. Oura, V. G. Lifshits, A. Saranin, A. V. Zotov, and M. Katayama, Surface Science: An Introduction (Springer-Verlag, New York, 2003).

[82] M. Mayer, AIP Conference Proceedings **475**, 541 (1999).

[83] D. Phillips and J. P. S. Pringle, *Nuclear Physics A* **135**, 189 (1976).

[84] F. G. R. A. Benninghoven and H. W. Werner, Secondary Ion Mass Spectrometry: Basic Concepts, Instrumental Aspects, Applications, and Trends (Wiley, New York, 1987).

Publications

D. A. Scott *et al.*, *First Direct Measurement of the $^{17}O(p,\gamma)^{18}F$ Reaction Cross Section at Gamow Energies for Classical Novae.* In Physical Review Letters **109**, 202501 (2012).

A. Caciolli, D. A. Scott *et al.*, *Preparation and characterisation of isotopically enriched Ta_2O_5 targets for nuclear astrophysics studies.* In The European Physical Journal A **48**, 144 (2012).

A. Di Leva, D. A. Scott *et al.*, *Underground study of the $^{17}O(p,\gamma)^{18}F$ reaction relevant for explosive hydrogen burning.* In Physical Review C **89**, 015803 (2014).